Millimeter Wave Channels for Vehicular Communications: Variability and Sparse Models

Dissertation

for obtaining the academic degree

Dr. techn.

as part of the study

Electrical Engineering and Information Technology

carried out by

Herbert Groll

student number: 00725518

Institute of Telecommunications
at TU Wien

Advisor:
Univ.Prof. Dr.-Ing Christoph Mecklenbräuker

Examiners:
Prof. Sana Salous, Ph.D.
Adjunct Prof. Peter Gerstoft, Ph.D.

Vienna, May 18, 2023

Statement on Academic Integrity

I hereby declare and confirm with my signature that the doctoral dissertation is exclusively the result of my own autonomous work, based on my research and literature published, which is seen in the notes and bibliography used. I also declare that no part submitted has been made in an inappropriate way, whether by plagiarizing or infringing on any third person's copyright. Finally, I declare that no part submitted has been plagiarized for any other paper in another higher education institution, research institution or educational institution.

Vienna, May 2023

Author's signature

Supervisor's signature

The best time to plan an experiment is after you've done it.
Ronald A. Fisher

Acknowledgments

I gratefully acknowledge the financial support of the *Doctoral School 5G Internet of Things* and TU Wien.
I want to thank my scientific advisor Christoph F. Mecklenbräuker for his continuous support and his motivation for this research and also for his guidance during the doctoral studies, which contributed to my personal evolution. I want to thank Peter Gerstoft and the Marine Physical Laboratory of the Scripps Institution of Oceanography at University of California, San Diego, for the opportunity of my research visit. I'm grateful for the scientific support through the *Inclusive radio communications for 5G and beyond* (IRACON) of the European Cooperation in Science and Technology (COST) Action CA15104 and for the vehicular millimeter wave cooperation between the Institute of Telecommunications at TU Wien, the Department of Radio Electronics at Brno University of Technology, Security & Communication Technologies Team at Austrian Institute of Technology, and the Wireless Devices and Systems Group at University of Southern California. I also want to thank my colleagues at the Institute of Telecommunications for the great atmosphere and a very special thanks to Stefan Pratschner, Erich Zöchmann, Robert Langwieser, Thomas Blazek, Sebastian Caban, Martin Lerch for their help and fruitful discussions at MIMO-Lab.
I want to thank my parents, my family, and my friends for their understanding and support in all aspects of life. Most importantly, I want to express my deepest gratitude to my love Kerstin for the encouragement, love, and endless support through this journey.

Abstract

Future wireless communications systems face increased demand for higher data rates and massive connectivity. These requirements are challenging to meet with the already scarce radio resource in the frequency spectrum below 6 GHz alone. Therefore, millimeter wave (mm-wave) bands are of interest for vehicular wireless communications, 5G systems, and beyond. Mm-wave communications systems are nothing new, but technological advancements allow their cost-effective use for new potential applications. Vehicular mm-wave radiocommunication allows large bandwidths with directed beams for short-range high-rate links.

This thesis investigates the mm-wave channel at 60 GHz supported by conducted experiments for vehicle to infrastructure (V2I) scenarios on three focus points.

First, the limited bandwidth leads to unresolvable propagation paths within the same delay tap of an equivalent tapped delay line channel model, giving rise to fluctuations known as small-scale fading. The magnitude of the delay tap that is attributed to the line of sight (LOS) component shows severe variability along the track of the investigated experiment. Small-scale fading due to the LOS component and specular component due to a ground reflection is a key issue for medium channel bandwidths with limited frequency diversity. The results on the variability show that the variability is lower for a beam with an uptilt compared to a horizontally directed beam due to the attenuation of a ground reflection. Wide beamwidths or unwanted strong sidelobes of the employed antennas are further reasons for the presence of dominant specular components which lead to severe fluctuations even for high channel bandwidths. I propose a novel small-scale fading model, which enables to model the fluctuations of the LOS delay tap magnitude in the presence of three dominant specular components with specific phase relations. The model explains why statistical tests on the magnitude distribution accept fading models for dominant specular components with fewer components than there are present. I perform an analysis of the magnitude distributions within small spatial regions along the trajectory of the V2I scenario. The two-wave with diffuse power fading model provides a good fit of the V2I mm-wave channel within small spatial regions, although evidence from the data suggests the presence of a third wave.

Second, it is convenient to model nonstationary time-varying random wireless channels as stationary within a limited region of time and frequency. This stationary channel model describes elementary time shifts (delay) and frequency shifts (Doppler) of the signal due to multipath components (MPCs). I perform an analysis of the V2I mm-wave channel's power distribution in the delay-Doppler domain with respect to different beam tilt angles of the vehicle's directive antennas. The wireless channel at 60 GHz in an

urban street canyon environment shows a low number of MPCs with significant power in the delay-Doppler domain. Moving or static vehicles with large reflective surfaces are identifiable in the measurements. The beam directed horizontally slightly increases the diversity in the delay-Doppler domain of a wireless system.
Third, the low number of MPCs in the delay-Doppler domain suggests that a parametric sparse model of only a few coefficients adequately models the V2I mm-wave channel. I apply the framework of atomic norm minimization (ANM) to identify scatterers in the delay-Doppler domain of a measured V2I mm-wave wireless channel. The ANM method is not restricted to a finite grid, but its application on the measured channel has an impracticable computation complexity for today's wireless systems. I show how the decoupled version of the ANM, which has lower complexity, successfully extracts the delay-Doppler parameters in high resolution for the channel's MPCs. The derived sparse representations are in good agreement with the measured channels which shows that the sparse model is adequate. The sparse representation models the wireless channel in a deterministic way. I therefore propose to employ hybrid deterministic and random time-varying channel models for V2I mm-wave communications.

Zusammenfassung

Zukünftige Funksysteme stehen vor der Herausforderung der stetigen Zunahme an erforderlicher Datenrate und Anzahl an verbundenen Kommunikationsteilnehmer. Diese Anforderungen sind nur schwer mit den knappen Frequenzressourcen zu erreichen, welche das intensiv genutzte Frequenzspektrum unterhalb von 6 GHz zur Verfügung stellt. Die Millimeterwelle (mm-Welle) und die damit in Verbindung stehenden Frequenzbänder großer Bandbreite sind daher von großem Interesse für die drahtlose Fahrzeugkommunikation, 5G Mobilfunksysteme oder ähnliche Systeme. Der Einsatz von mm-Wellen ist für gewisse Funksysteme schon länger Stand der Technik, jedoch führt die voranschreitende Miniaturisierung und Integration der dafür notwendigen Technologie zu stets kosteneffizienteren Anwendung der mm-Welle für neue Einsatzfelder. Für die Fahrzeugkommunikation ermöglicht die mm-Welle durch die großen Bandbreiten und bei der Verwendung von gerichteten Antennen eine Funkübertragung über kurze Distanzen bei einer hohen Datenrate.

Diese Arbeit untersucht den Funkkanal der mm-Welle bei 60 GHz in drei Fokuspunkten auf Basis von durchgeführten Experimenten zur Kommunikation zwischen Fahrzeug und Verkehrsinfrastruktur (V2I) im urbanen Straßenverkehr.

Im ersten Punkt gehe ich auf das Problem des kleinräumigen Signalschwunds ein, welches trotz des Bestehens einer Sichtverbindung bei der Verwendung von bandlimitierenden Systemen bestehen kann. Ich beschränke mich dabei auf die Verzögerungsauflösung bei der Verwendung mittlerer Kanalbandbreiten. Dabei kann sowohl eine Bodenreflexion als auch weitere Komponenten der Mehrwegeausbreitung maßgeblich zum kleinräumigen Schwund beitragen. Ich untersuche die Veränderlichkeit des Funkkanals entlang der Trajektorie des Fahrzeugs hängt dabei von der Ausrichtung der gerichteten Antennen ab. Eine leicht nach oben geneigte Ausrichtung weißt eine kleinere Veränderlichkeit auf als eine horizontale Ausrichtung. Ich stelle ein Model für den kleinräumigen Schwund vor, welches die Modellierung von drei dominierenden Komponenten der Mehrwegeausbreitung mit einer Phasenabhängigkeit erlaubt. Durch das Model können Ergebnisse statistischer Tests auf eine bestimmte Verteilungsfunktion der Empfangsamplitude erklärt werden, welche ein Schwundmodel nicht ablehnen obwohl jenes Model weniger dominierende Komponenten vorsieht als vorhanden sind. Ich führe eine Analyse der Verteilung der Empfangsamplitude für den Funkkanal entlang der Trajektorie des Fahrzeugs im V2I-Szenario durch. Das *Two-Wave with diffuse power*-Schwundmodel liefert dabei gute Anpassungsergebnisse bei der Beschränkung auf kleine Streckenabschnitte, wobei die vorhandenen Messdaten auf eine dritte dominierende Komponente hindeuten.

Im zweiten Punkt betrachte ich den zeitvarianten Funkkanal in der kombinierten Zeitverzögerungs- und Dopplerverschiebungsdomäne, kurz Verzögerungs-Doppler-Domäne, um die Leistungsverschiebung von Signalen durch Komponenten der Mehrwegeausbreitung in jener Domäne zu beschreiben. Ich analysiere den gemessenen V2I-Funkkanal für die mm-Welle in der Verzögerungs-Doppler-Domäne und untersuche den Einfluss der Neigung der gerichteten Antennen am Fahrzeug. Die Untersuchung zeigt für eine städtische Straßenschlucht eine geringe Anzahl an signifikanten Komponenten der Mehrwegeausbreitung in der Verzögerungs-Doppler-Domäne. Sich bewegende oder abgestellte Fahrzeuge, welche eine große Fläche für Reflexionen darstellen, sind in den Messergebnissen identifizierbar. Eine horizontal gerichtete Antenne erhöht dabei die Diversität in der Verzögerungsdomäne.
Im dritten Punkt verwende ich wegen der geringen Anzahl an Komponenten in der Verzögerungs-Doppler-Domäne ein parametrisches spärliches Model zur Beschreibung des V2I-Funkkanals für die mm-Welle. Ich wende das Konzept der *atomaren Normen* und dessen Minimierung (ANM) am gemessenen Funkkanal an zur Identifikation von Streuern in der Verzögerungs-Doppler-Domäne. Die ANM-Methode ist dabei nicht auf ein endliches Raster zur Bestimmung der Verzögerungs-Doppler-Parameter beschränkt. Da die Anwendung von ANM auf die Funkmessdaten einen hohen Rechenaufwand benötigt ist diese Methode für heutige Funksysteme noch nicht praktikabel. Ich zeige anhand einer entkoppelten ANM-Variante mit niedrigeren Rechenaufwand die erfolgreiche hochauflösende Bestimmung der Verzögerungs-Doppler-Parameter von Komponenten der Mehrwegeausbreitung. Ein davon abgeleitetes parametrisiertes spärliches Model beschreibt den gemessenen Funkkanal in guter Näherung. Da dieses Model den Kanal in einer deterministisch beschreibt, schlage ich für die Modellierung von zeitvarianten V2I-Funkkanälen für die mm-Wellenkommunikation die Verwendung von hybriden Modellen vor, welche aus einem deterministischen und einem stochastischen Anteil bestehen.

List of Abbreviations

3GPP 3rd Generation Partnership Project

ANM atomic norm minimization

BEM basis expansion model

CBF conventional beamformer

CDF cumulative distribution function

CFO center frequency offset

CIR channel impulse response

CV coefficient of variation

D-ANM decoupled ANM

DFT discrete Fourier transform

DOA direction of arrival

FDM frequency division multiplex

HPBW half power beam width

i.i.d. independent and identically distributed

ICT Information and Communication Technology

IEEE Institute of Electrical and Electronics Engineers

IO interacting object

LASSO least absolute shrinkage and selection operator

LOS line of sight

LSF local scattering function

LTV linear time-varying system

MAPP matrix pencil and auto-pairing

ML maximum likelihood

mm-wave millimeter wave

MPC multipath component

MUSIC multiple signal classification

NAE normalized approximation error

NR New Radio

OFDM orthogonal frequency division multiplex

PAPR peak to average power ratio

PDF probability density function

PSD positive semi-definite

RMS root mean squared

RMSE root mean squared error

RSU road-side unit

RX receiver

SBL sparse Bayesian learning

SDP semi-definite program

SNR signal-to-noise ratio

STFT short-time Fourier transform

TDL tapped delay line

TVTF time-varying transfer function

TWDP two-wave with diffuse power

TX transmitter

V2I vehicle to infrastructure

V2V vehicle to vehicle

V2X vehicle to everything

WSSUS wide-sense stationary uncorrelated scattering

Contents

1 Introduction

Future wireless communications systems will face increasing demand such as higher data rates and massive connectivity. Standardization bodies and technology working groups are thus keen on advancing established technology standards like the 3rd Generation Partnership Project (3GPP) 5G technology standard to meet the increasing demand. In 2021, the European Telecommunications Standards Institute, which is a 3GPP member, selected the "evolution of 5G radio (B5G, 6G)" as one out of ten major technology trends in the technology radar for Information and Communication Technology (ICT) [1]. A key technology within this evolution is millimeter wave (mm-wave) and higher frequencies for communications, which have the potential for a surge of new radio technologies, network models, and massive machine type communications [1]. All ten major trends stated in [1], artificial intelligence and internet of things being widely known examples, are not independent of each other and could mutually amplify their evolution. ICT systems need sufficient bandwidth and reactivity to ensure successful operation and to allow further evolution of those technologies.
Furthermore, mm-wave wireless channels are an exciting evolution for vehicle to infrastructure (V2I) and vehicle to vehicle (V2V) communications, including but not limited to future applications in autonomous vehicles, cooperative driving, or other more advanced intelligent transportation systems. High data rates become necessary when vehicles and infrastructure exchange their sensor data to enable sensor fusion required for potential applications. Currently, established vehicular wireless communications standards allow wireless communications with high reliability at sub-6 GHz frequency bands. The mm-wave bands are an important addition to reach the desired Gbit/s data rates without consuming the limited radio resources at sub-6 GHz [2]. The technology standards *Institute of Electrical and Electronics Engineers (IEEE) 802.11ay* and *3GPP 5G New Radio (NR)* already leverage mm-wave already for non-vehicular scenarios.
V2I and V2V wireless communications radio technologies are subsumed under the umbrella term vehicle to everything (V2X) and there are many opportunities and challenges for the successful operation of wireless communications systems at mm-wave bands. These include signal losses, sparsity of the wireless channel, interaction with the environment, and the nonstationary aspect of the vehicular wireless channel.

Signal losses. The free-space path loss of the wireless channel, as defined by the Friis equations [3] with ideal isotropic antennas, increases with higher transmission frequency. However, the effective area of an ideal isotropic antenna decreases with increasing transmission frequency such that the free-space path loss only describes how the power density

of a spherical wave decreases with distance. Conversely, the antenna directivity increases if the transmission frequency increases and the effective antenna area remains the same. Therefore, it is feasible to manufacture directive antennas for mm-wave with a small footprint. Even though free-space path loss is not a loss in the ohmic sense, radio waves at higher frequencies still experience higher attenuation due to interaction with molecules in the atmosphere. Absorption lines of gases in the lower atmosphere and rain constitute additional attenuation for mm-wave bands, but this influence is negligible for small-cell applications [4], e.g. for short range communications considered in V2X mm-wave communications applications.

Sparsity. Sparsity of the wireless channel can be an attractive property for channel sounding, modeling, and estimation [5]. The suitability of sparse methods depends on data being in agreement with parsimonious models. Those parsimonious models can be adequate to describe some propagation scenarios sufficiently well. The wide conception is that mm-wave channels are sparse, although this is only true in terms of the delay and the angular domain and only if sufficiently high bandwidth and antennas with sufficiently narrow beams are employed [6]. It does not necessarily mean that the number of significant multipath components (MPCs) is small [6]. Mm-wave communications systems employ directional antennas to combat high free-space path loss and allow to operate with wider bandwidths due to a less-crowded frequency spectrum, and thus experience sparser scattering in observed scenarios [7]. Furthermore, the significant MPCs exhibit a sparse structure in Doppler domain for vehicular mm-wave channels [8], [9] given a sufficiently high channel snapshot rate for resolving components in the Doppler domain. For a description of the wireless channel in the delay, angular, or Doppler domain, sparse estimation methods could offer an advantage in parameter estimation, especially when the parameter space is large.

Interaction. When moving from 6 GHz to 60 GHz, the wavelength decreases by a factor of ten, while the environment remains the same. This means that the influence of diffraction is reduced for mm-wave due to the size of common objects in the environment [2]. For rough surfaces, diffuse scattering becomes more important than specular scattering [4]. Shadowing, caused by environmental objects, is of great importance for mm-waves [6]. Those effects are independent of employed antennas and need to be considered for highly detailed channel modeling, e.g. in ray tracing.

Nonstationarity. The vehicular wireless channel is generally time-varying due to the mobility of vehicles or moving objects in the propagation environment. Many vehicular wireless channels have only short stationarity times and limited stationarity bandwidths when modeling the channel as random [10], [11]. Therefore, nonstationarities must be taken into account for V2X communications and antenna beam management becomes especially important for mm-wave due to the employment of directive antennas [2].

Based on measurements, the temporal variations make it difficult to identify, statistically characterize, or model vehicular channels [12].

1.1 Literature Review

I review relevant research for V2I mm-wave communications on experimental channel analysis, antenna positions on the vehicle, and the different aspects of sparsity.

Experimental Channel Analysis. The use of mm-wave for V2X has been a research topic for several decades already with examples ranging from path loss measurements for train-to-infrastructure scenarios in [13] to performance investigation for V2V communications [14].

In general, the last two decades were marked by great interest in sub-6 GHz vehicular communications, where experimental research, e.g. [12], [15]–[18], provided the necessary understanding to design today's systems for V2X communications. Those experiments took nonstationarity into account and were mostly conducted with omnidirectional antennas.

Apart from its specific frequency range, the use of directional antennas is a key aspect for mm-wave compared to sub-6 GHz vehicular communications. V2V measurements in [19] investigate the channel at 38 GHz and 60 GHz, using a channel sounder with 1 GHz bandwidth. The two involved vehicles drive along a road with guard rails. The derived two delay tap model sufficiently describes the measurement, which is possible due to employed highly directive antennas placed in the bumpers of cars. One delay tap includes a direct path and a reflected component. The second delay tap corresponds to the presence of a road guard rail. Likewise, overtaking vehicles may cause significant components as investigated at 60 GHz in [20], [21]. A more detailed statistical analysis of delay and Doppler spread in [22], [23] shows the effect of the size of the overtaking vehicle, where large vehicles could offer large surfaces for specular reflection. Further mm-wave V2V measurements with approaching cars are shown in [24], where the high bandwidth of 8 GHz allows fine delay resolution. The availability of large consecutive bandwidth is currently given at mm-wave bands. Employing the same channel sounder in a V2I measurement campaign shows power-delay profiles and a statistical analysis of the root mean squared (RMS) delay spreads with notable variations due to passing vehicles [21].

For intra-vehicular communications, while the vehicle is in operation, the works in [25], [26] point out the severe influence of the road quality on the fading characteristic due to vibrations. Therefore, it is very likely that the effect of vibration is also present for V2X communications.

The mm-wave wireless channel has been observed to have a sparse multipath structure in multiple domains [27]–[29]. The authors in [9] suggest that a V2I channel features

more discrete MPCs in the Doppler domain at mm-wave bands compared to a sub-6 GHz band. Simultaneous multiband ultra-wideband double-directional measurements at 6.75 GHz, 30 GHz, and 60 GHz are reported in [30]. The analysis of a corner scenario of a "T"-intersection in an urban environment indicates similar scattering opportunities at the sub-6 GHz and the mm-wave bands.

An experimental 60 GHz wireless system in [31] provides insights about the variability of the received signal-to-noise ratio (SNR) in a V2I scenario. The variability of the SNR is higher at higher vehicle speed due to beam alignment fluctuations of the employed antennas. Furthermore, antennas with a wider beamwidth also caused higher variability. However, the variability of the results is probably only due to beam alignment and not due effects which are specific to the mm-wave band.

The authors in [32], [33] analyze a high-mobility V2I expressway scenario at 28 GHz. The RMS delay spreads are small due to the availability of a line of sight (LOS) component and MPCs, possibly due to large objects, with significantly less power [32]. The investigation of the same expressway scenario in terms of wide-sense stationarity revealed that the range of stationary distance is 6–23 wavelengths for a channel bandwidth of 500 MHz [33]. This short stationary distance may be a consequence of the LOS component and a purely random channel is possibly an inadequate model.

The variability of the V2V mm-wave wireless channel at 73 GHz and a channel bandwidth of 409.6 MHz was under investigation in [34]. A two-slope fit provides a good model for the large-scale fading effects and a Kolmogorov-Smirnov test decides on the goodness-of-fit of several parametric cumulative distribution functions (CDFs) to the small-scale fading effects. However, parts of the large-scale fading curve show a two-ray fading behavior, which indicates that the averaging window was too small too remove small-scale fading effects from two dominant specular components, e.g. a LOS component and a ground reflection.

Antenna positions. The antenna position on the vehicle becomes more crucial for smaller wavelengths as less power from diffraction or penetration is available. This is corroborated by [35] in which possible antenna positions on a car at 0.6 –1.48 m height are investigated via V2V path loss measurements at 28 GHz [35].

Antennas for vehicular mm-wave are investigated in a traffic simulation study in [36] at 28 GHz with a focus on beamforming capabilities of the employed antenna arrays. The study takes the effects of the vehicle on the radiation pattern into account and proposes the placement of 4×3 antenna arrays at each north, south, west, east edge of the vehicle's roof [36].

The antennas can be integrated in the bumpers of cars as in the measurement campaign in [19]. The authors in [37] compare beamforming loss for rooftop and bumper positions and road roughness profiles, with a slight advantage of rooftop-mounted position. Mounting antennas for V2I near the car roof at the windshield is considered in [38], where a suitable antenna for 5G NR at 28 GHz is designed. High gain with wide angular

coverage is achieved with a multi-array design of several simultaneous directed beams. However, low sidelobe suppression could lead to unwanted strong specular components interfering with a LOS component.

Sparsity. Several authors [39], [40] have proposed numerous low-complexity linear time-varying system (LTV) channel models to describe propagation effects on a transmitted waveform in an approximate way.

It is often desirable to have a low number of significant coefficients in such a model to exploit this sparse structure and to improve channel estimation performance [41], [42]. Sparse methods also provide valuable tools in denoising applications for signal approximations [41], denoising [43] and even for long-tailed data statistics [44].

Most popular sparse signal processing techniques for parameter estimation are restricted to a predefined grid, e.g. orthogonal matching pursuit, basis pursuit, and least absolute shrinkage and selection operator (LASSO). For those techniques, an overcomplete basis or dictionary is essential for sparse recovery [45, Ch. 13]. Sparse signal reconstruction using the sparse Bayesian learning (SBL) framework with low-complexity is used in [46], [47]. A fixed-point implementation of SBL [47] is shown in [48].

Sparse channel estimation for time-varying channels is considered in [41], [49]. Sparse approximations of V2V measurements with c-LASSO and oversampled discrete Fourier transform (DFT) basis is presented in [50]. The sparsity of wireless channels is often based solely on intuitive analysis and the lack of proper measures is discussed in [5], [51] where a combination of indicators is employed to estimate channel sparsity. The authors in [52] apply basis pursuit to estimate delay-Doppler from passive orthogonal frequency division multiplex (OFDM) radar signals.

State-of-the-art wireless systems employ a probing signal to aid in channel estimation. The probing signal has finite bandwidth and snapshot period which leads to a fundamental uncertainty in the delay-Doppler domain [53]. Prior knowledge about the delay-Doppler characteristics of the propagation channel enables optimal design of such a probing signal. Imposing a suitable sparsity constraint as prior information on the propagation channel enhances its recovery with super-resolution capability in the delay-Doppler domain [54], [55]. High-resolution delay-Doppler estimates improve OFDM channel estimates when only a few significant MPCs are present [56]. Furthermore, inferred propagation scenario geometry from delay-Doppler estimates aid in target tracking [57] and antenna beam alignment [58].

One sparsity-aware method with the aim to infer simple models from limited measurements is the framework of atomic norm minimization (ANM), a non-greedy method. Advantages of the ANM method are its gridless approach to the estimation of sparse models, its capability of automatic model selection, and its suitability for compressed sensing [55]. It can be understood as a generalization of the grid-based LASSO estimator to a gridless approach [43], [55]. ANM is also known as total-variation minimization [55] or the Beurling LASSO [59] in literature. Further, the formulation of ANM as an op-

timization problem allows to easily incorporate additional constraints into the original ANM [60]. Disadvantages of ANM are its unfavorable scaling of numerical complexity with problem size and the necessary signal separation conditions [59] to reach theoretical performance guarantees.
As the resolution of individual MPCs in delay becomes feasible due to increased bandwidth, delay estimation utilizes techniques similar to direction of arrival (DOA) estimation in array processing [61]. ANM enables gridless estimation of the DOA of sources from sensor array measurements [62]. An extension to non-uniform linear arrays via irregular Vandermonde decomposition is shown in [63]. The application of ANM for real array measurements is shown in [64]. DOA estimation with deep learning methods from single delay-Doppler snapshots in automotive radar is investigated in [65].
The authors of [60] and [66] employ the ANM for simulated data where model mismatch from varying delays is ignored.

1.2 Contribution

My research work is on one hand focused on DOA estimation for array processing [48], [64], [67]–[69] and on the other hand on vehicular wireless communications in the mm-wave frequency band [8], [70]–[72].
Regarding DOA estimation, I investigate the implementation aspect for a sparsity aware DOA estimation method in [48], the problem of characterizing the robustness of DOA estimators in [67], and apply sparse methods [69] to real antenna array measurements conducted at TU Wien [73] or in the collaborative work with University of California, San Diego [64].
The vehicular mm-wave research was conducted in collaboration with Brno University of Technology, University of Southern California, Austrian Institute of Technology, and the research group at TU Wien, where preparations for measurement campaigns [8], [9], [23], [24], [74], [75] required particularly careful design and thorough review.
Most relevant for this thesis are my works in [8], [71], [72], where the sparsity-aware methods bridge the gap between the DOA topic and the vehicular mm-wave topic. The aims of my research in this thesis is the investigation on the variability, on sparsity, and on the application of sparse methods for V2I mm-wave channels
The most important contributions are the following.

Chapter 4. The descriptive statistics of a V2I mm-wave channel show severe variability along the vehicle's trajectory in an urban street scenario [71]. The variability of the channel depends on the spatial filtering of the antenna pattern, where variability is lower for an antenna beam with an uptilt than a horizontal antenna beam. I show that averaging is not suitable in the investigated nonstationary V2I scenario to separate small-scale fading from large-scale fading. I describe a simplified three-wave with diffuse power fading model, which can statistically describe the small-scale fading of the wireless

channel within small spatial regions. Restricted to positions within those regions, the two-wave with diffuse power (TWDP) fading model provides a good fit.

Chapter 5. The sparsity assumption of the V2I mm-wave channel holds true in the delay-Doppler domain for measured 60 GHz V2I communications channels in the same street crossing scenario in an urban environment [8]. Large vehicles are identifiable in the delay-Doppler domain at channel bandwidths of 100 MHz and they may provide an additional propagation path to the LOS. I show that a horizontally directed beam in the investigated V2I mm-wave scenario creates a wireless channel with more resolvable MPCs with significant power than a beam with a 15° uptilt. Therefore, the additional propagation paths provide increased delay-Doppler diversity and specifically increased reliability in some cases, e.g. when the LOS component is blocked.

Chapter 6. Sparsity in the delay-Doppler domain enables application of sparse estimation methods. I propose and develop ANM and decoupled ANM (D-ANM) for application to joint delay-Doppler estimation of MPCs for nonstationary V2I mm-wave channels in [72]. I empirically analyze its performance through numerical channel simulations in the presence of a small number of spatial clusters of point-scatterers and in application to real-world mm-wave measurement data, acquired in a V2I environment. I show that ANM applied to the samples of wireless channel measurements suffers from leakage effects similar to spectral analysis, possibly due to model mismatch. I show that D-ANM is suitable for scatterer identification in the delay-Doppler domain for cluster spreads smaller than the resolution of the system. Based on the vehicular mm-wave measurement data, I show that scatterers identified with D-ANM accurately model the time-variant channel parameters mean delay, RMS delay spread, mean Doppler, and RMS Doppler spread.

1.3 Notation

a^*	complex conjugate
$\mathbf{a}$	bold-faced lower-case letters denote column vectors
$\mathbf{A}$	bold-faced upper-case letters denote matrices
$\mathrm{vec}(\mathbf{A})$	stacks all columns of $\mathbf{A}$ with a column vector as result.
$\mathcal{A}$, $\mathcal{H}_0$	calligraphic letters denote sets or a hypothesis
$\mathbf{a}^{\mathrm{T}}, \mathbf{A}^{\mathrm{T}}$	transpose operator on a vector or matrix
$\mathbf{a}^{\mathrm{H}}, \mathbf{A}^{\mathrm{H}}$	complex-conjugate transpose operator on a vector or matrix
$\odot$	Hadamard product, i.e. elementwise product
$\otimes$	Kronecker product of two matrices
$\mathbf{e}_n$	canonical basis vector with a single one at position n
$\mathbf{1}_L$	column vector with ones at all L entries
$\mathbb{E}_x\{\cdot\}$	expectation with respect to random variable x (omitted when clear from context)

1.4 Structure

In chapter 2, I describe the aspects of multipath propagation, signal fading, and the time-variant channel model I apply throughout the thesis. Section 2.1 gives an overview of the terminology within this thesis for multipath propagation. Section 2.2 describes the signal fading effects I identified in the investigated scenarios. Section 2.3 introduces the time-variant channel model for underspread channels.
In chapter 3, I describe the channel sounding process through a multicarrier system to obtain the measured wireless channel Section 3.1 gives an quick overview of channel sounding. Section 3.2 describes the details for channel sounding with a multicarrier signal and section 3.3 extends to multiple channel. Section 3.3.2 discusses the resolution limits and the arising ambiguity.
In chapter 4, the variability of the wireless channel is analyzed under the presence of dominant specular components. Section 4.1 introduces possible nonparemetric and parametric statistical models for the analysis of fading with a simplified three-wave with diffuse power model in section 4.1.4. Section 4.2 describes the inference of a small-scale fading model from samples of simulation or measurement data. Section 4.3 introduces the V2I scenario under investigation for simulation and measurement. Section 4.4 describes the simulation setup and shows their results concerning the variability and distribution fits. Section 4.5 describes the setup of the conducted measurement and shows their results concerning the variability and distribution fits. I give a discussion of chapter 4 in section 4.6.
In chapter 5, I provide an analysis of the wireless channel in the delay-Doppler domain and identify scatterers specific to the investigated urban street environment. Section 5.1 describes the local scattering function (LSF) as a useful tool for analyzing nonstationary time-varying channels. Section 5.2 reintroduces the V2I measurement campaign. Section 5.3 shows the measurement results regarding identified scatterers in the delay-Doppler domain. I give a discussion of chapter 5 in section 5.4.
In chapter 6, I employ sparse methods to identify scatterers in the delay-Doppler domain with a focus on gridless estimation employing decoupled atomic norm minimization. Section 6.1 discusses sparse methods with estimation on the grid to gridless estimation methods with ANM in section 6.1.4 and D-ANM in section 6.1.5. Section 6.2 describes a simple simulation model, which is compatible to the investigated V2I mm-wave scenarios, to assess the chosen gridless estimation methods. Section 6.3 briefly introduces a second measurement campaign. Section 6.4 shows the simulation and measurement results of the scatterer identification and the applicability of the sparse model on the measurement data. I give a discussion of chapter 6 in section 6.5.
I provide conclusions to my work in chapter 7.

2 Vehicular Millimeter Wave Communications Channels

This chapter discusses the theoretical framework for the analysis of vehicular mm-wave communications channels with emphasis on the estimation of the dominant components of sparse V2I mm-wave channels as relevant for the research question.

2.1 Multipath Radio Propagation

"Wireless channels differ from wired channels by multipath propagation, i.e. the existence of a multitude of propagation paths from transmitter (TX) and receiver (RX), where the signal can be reflected, diffracted, or scattered along its way [76]." A direct unobstructed propagation path from TX to RX is known as the line of sight (LOS) path. Other propagation paths can exist in the environment due to the presence of interacting objects (IOs), which are dielectric or conducting obstacles for radio waves [76]. A widespread approximation for the complicated propagation phenomena of radio waves is the ray model. Each ray is a model for the direction of a plane wave for which the laws of geometrical optics for reflection and transmission apply. The superposition of plane waves causes interference which leads to fading of the sum amplitude when small variations of the relative phase between waves take place. This fading effect is further described in section 2.2.
Furthermore, the superposition of multiple rays constitutes a resulting propagation path and permits an approximate model of various phenomena, e.g. diffraction and scattering [76]. The ray model is unsuitably detailed to interpret results of wireless communications channel measurements due to limited resolution of the measurement system. Therefore, a common term for superposition of unresolvable rays is a multipath component (MPC), which transfers energy in a channel. The terms ray and MPC are often used interchangeably in literature.
Here, I provide an overview of the multipath radio propagation terminology used in this thesis.

Scattering. For radio propagation, scattering is the process when a wave interacts with a boundary such that the wave is scattered in multiple directions. E.g. scattering at rough surfaces, which leads to diffuse scattering of the waves.

Reflection. The wave interacts with a boundary, e.g. a surface, that is larger in size than the wavelength and the wave is reflected dominantly in specular direction.

Scatterer. An IO is known as scatterer at high-level characterization, even when interaction with radio waves is not a scattering process [76]. An infinitely small scatterer is a common element of simulation models and known as point-scatterer.

Multipath component. An MPC carries energy through one out of many propagation paths which a signal travels from TX to RX.

Specular component. A plane wave incident on a specular surface causes a reflected plane wave in specular direction, i.e. the specular component.

Coherent component. A plane wave incident on a slightly rough surface causes a scattering pattern with a reflected wave as coherent component in specular direction and non-coherent component in all other directions. It is called coherent because the reflected wave has a uniform phase front [77] and it exists only within a small angle around the specular direction.

Specular surface. A specular surface has a low electrical roughness, e.g. $ks < 0.2$ as defined in [77] where $k = \frac{2\pi}{\lambda}$ is the wavenumber and s is the RMS height of the surface, e.g. $s < 1.6\,\text{mm}$ for 60 GHz.

Slightly rough surface. Similar to a specular surface but with $0.2 \leq ks < 2$ as defined in [77], e.g. $s < 0.16\,\text{mm}$ for 60 GHz.

Cluster A cluster can have several definitions, primarily associated with a group of elements with a shared parameter. In this thesis, I define a cluster as a group of point-scatterers whose parameters come from the same distribution.

2.2 Fading

The variability of a received signal's magnitude is known as fading. A popular classification of fading is according to the scale at which a mechanism causes variations. The path loss is dominant for large-scale fading. Shadowing and obstruction through objects is characteristic for medium-scale fading. Interference of MPCs is the dominant effect for small-scale fading.
V2I scenarios are similar to urban microcell mobile communications scenarios [6], with restrictions on the placement of the infrastructure node at the roadside or at a central

position of an intersection. For V2I mm-wave communications over short ranges, small-scale fading models need to consider the employed directional beams, which act as a spatial filter to MPCs. For example, if spatial filtering reduces the number of significant MPCs in an otherwise rich scattering environment to a small number, then an invocation of the central limit theorem is unjustified.

2.2.1 Small-Scale Fading

MPCs interfere with each other constructively or destructively depending on their phase relation. A change in phase can have multiple sources, e.g. additional path length or complex reflection coefficient. If the phase of each MPC is deterministic, then interference is particularly pronounced.
A popular statistical model for small-scale fading in LOS scenarios is the Rician fading model [3], [76]. The LOS scenario often implies that there is only one dominant and many diffuse components present. In that case, the envelope of the received signal follows a Rice distribution, described by the Rice factor K_{R} and the second moment of the envelope Ω. However, the envelope distribution can change severely in the presence of additional dominant components [78], [79]. Small-scale fading of measurements is often analyzed only at a single frequency, where the channel is excited by a continuous wave signal [80]. Nevertheless, a stochastic description at a single frequency is insufficient for designing wideband wireless communications systems. There, a suitable stochastic description is achieved by a delay dependent fading analysis of the channel impulse response (CIR) from wideband measurements [3]. A tapped delay line (TDL) model is able to provide an adequate description for CIR [76], [81]. The taps of the TDL model have a deterministic or stochastic behavior, depending on the choice of the model. For stochastic TDL model variants, evaluating the small-scale fading statistics from measurements allows to parametrize probability density functions (PDFs) for all delay taps [82]. However, the results are influenced by the measurement system.
For many types of channel sounders, the measured wireless channel is available in the frequency domain, after post-processing, as time-varying transfer function (TVTF) with discrete time-frequency samples. An inverse DFT recovers a sampled CIR with equidistant delay taps. The influence of a spectral window when transforming the TVTF into the CIR is often neglected, e.g. a Hann window in [83], [84]. Especially neighboring delay taps are correlated when no rectangular window is employed [85].

2.2.2 Further Fading Classification

Large-scale fading, medium-scale fading, and shadow fading are stochastic models for signal fluctuations which describe fading effects relevant for larger distances than the LOS scenarios investigated in this thesis. Those fading categories are characteristic in terms of the spatial scale at which fading occurs. In the time-varying channel case, typical categories for fading are *fast* fading and *slow* fading, where the distinction is based on

the temporal scale. This classification depends on assumptions about the specifications of a wireless communications system, e.g. the symbol duration, and the change rate of the wireless channel due to movement, and is thus rather limited. However, the term fast fading is often synonymously used in literature for small-scale fading effects [76].

2.3 Time-Varying Channel

The transmission effects of a signal through a wireless channel are often sufficiently described by a linear model. In static and quasi-static environments, the theory of linear time-invariant systems provides an adequate description of the time delays and the change in magnitudes of the signal. If the rate of change of the wireless channel is significant, as often the case for V2I wireless communications, the theory of linear time-varying systems provides a better description than a time-invariant model.

2.3.1 Linear Time-Variant Channel Model

For the input signal $s(t)$ and the output signal $r(t)$, the narrowband LTV channel input-output relation is [76, eq. (6.9)–(6.11)]

$$r(t) = \int_{-\infty}^{\infty} h(t,\tau)s(t-\tau)\mathrm{d}\tau + z(t), \tag{2.1}$$

where $h(t,\tau)$ is the time-varying CIR and $z(t)$ is additive white Gaussian noise. The LTV channel is described equivalently in the frequency domain by the TVTF of the channel $H(t,f)$ and the corresponding Fourier transform of $s(t)$ as the spectrum $S(f)$ of the input signal. The output signal is equivalently

$$r(t) = \int_{-\infty}^{\infty} H(t,f)S(f)e^{j2\pi tf}\mathrm{d}f + z(t). \tag{2.2}$$

The interpretation of $H(t,f)$ as a time-frequency transfer function [1] is a special case and relies on an *underspread* assumption as described in section 2.3.5. Most wireless channels are underspread [87] and I assume the underspread assumption is valid for the considered scenarios in this thesis.

For a narrowband LTV system, it is adequate to approximate the Doppler effect as a frequency shift ν. The spreading function $S_{\tau,\nu}(\tau,\nu)$ is a different representation with

[1] Different definitions exist, c.f. [86]

emphasis on the time dispersion and the frequency dispersion of the channel. A two-dimensional Fourier transform connects $S_{\tau,\nu}(\tau,\nu)$ with $H(t,f)$ [53, eq. (1.11)]

$$H(t,f) = \int_{-\infty}^{\infty}\int_{-\infty}^{\infty} S_{\tau,\nu}(\tau,\nu)e^{j2\pi(t\nu-f\tau)}\mathrm{d}\tau\mathrm{d}\nu, \tag{2.3}$$

where (τ, f) and (ν, t) are both Fourier pairs.

2.3.2 Deterministic and Random Channel Description

The number of scatterers plays an important role if a deterministic or a random wireless channel description is appropriate. If only a low number of scatterers are present and path delays change approximately linearly, then the channel is almost periodically time-varying and can be approximated by a sum of complex exponentials [88]

$$h(t,\tau) = \sum_{\nu\in\mathcal{N}} h_\nu(t-\tau)e^{j2\pi\nu\tau}, \tag{2.4}$$

where $h(t,\tau)$ is the CIR, ν a frequency shift, $\mathcal{N}$ is a countable set, and $h_\nu(\cdot)$ are Fourier series functions. The CIR in eq. (2.4) as a LTV can thus be implemented as a sum of frequency shifted linear time-invariant system systems [89]. Implemented as a filter, this is known as *frequency shifted* (FRESH) filtering [89]. If the different $h_\nu(\cdot)$, $\forall\nu$, itself are adequately described by a weighted sum of Dirac impulses $\delta(\cdot)$ as

$$h_\nu(t) = \sum_{\tau\in\mathcal{T}_\nu} c_{\nu\tau}\delta(t-\tau), \tag{2.5}$$

where $\mathcal{T}_\nu$ is a set of delays for a specific ν and $c_{\nu\tau}$ is a complex valued weight, then the received signal $r(t)$ in eq. (2.1) is

$$r(t) = \sum_{(\nu,\tau)\in\mathcal{X}} c_{\nu\tau}s(t-\tau)e^{j2\pi\nu t} + z(t), \tag{2.6}$$

with countable set $\mathcal{X} = \{(\nu_1,\tau_1),\ldots,(\nu_S,\tau_S)\}$ of S frequency shifts and delays. The deterministic channel descriptions eq. (2.4) and eq. (2.6) are parsimonious for a small number S of MPCs.

A strong LOS component together with strong specular reflections are often modeled as deterministic rather than as a nonstationary process [90]. For vehicular channels, the $c_{\nu\tau}$ and $\mathcal{X}$ are still time-varying, but more "slowly", i.e. they change at a larger scale and are approximately constant at a smaller scale.

A stochastic description of the wireless channel seems appropriate when many scatterers are present [88]. For a stochastic description of the wireless channel the TDL model is a popular description of the CIR due to its low complexity [81]. It is based on a wide-sense

stationary uncorrelated scattering (WSSUS) assumption of the channel to describe the random channel through power spectral densities of random processes. For vehicular channels, the WSSUS assumption is often considered violated [18], [84], [91] and an adaptive approach between regions of quasi-stationarity is chosen for modeling [92], [93].
A random time-variant channel has generally a mixed deterministic and random part [81]. For mm-wave channel, where a LOS component is present, the deterministic part of the channel grows in importance. Therefore, one must decompose the mixed channel and restrict the WSSUS analysis only for the purely random channel [81]. A hybrid deterministic and random channel modeling approach is considered in quasi-deterministic channel models of *IEEE 802.11ad/ay* [90].

2.3.3 Geometry-Based Channel Model

Employing basis functions for modeling of time variations is a favorable approach when there is prior knowledge of the fast variations. With reasonable assumptions like strong reflections of only a few components, complex exponentials can capture the variations of channel coefficients [88, Sec. 6.4].
A model for the CIR of a noise-free sparse LTV channel is the sum of S discrete MPCs in a delay-Doppler formulation as [53, eq. (1.17)]

$$\tilde{h}(t,\tau) = \sum_{s=1}^{S} c_s(t)\delta(\tau - \tau_s(t))e^{j2\pi\nu_s(t)t}, \tag{2.7}$$

with complex-valued channel amplitude $c_s(t)$, propagation delay $\tau_s(t)$, and Doppler frequency $\nu_s(t)$ of the s-th MPC. The geometry of the propagation environment, materials of IOs, and employed antennas define the parameters of the MPCs and if the amplitude is significant for an inclusion in eq. (2.7). The change of a MPC's propagation delay introduces a modulation of the channel amplitude, i.e. the Doppler modulation $e^{j2\pi\nu_s(t)t}$ with Doppler frequency

$$\nu_s(t) = -f_c\frac{\partial\tau_s(t)}{\partial t}, \tag{2.8}$$

where f_c is the center frequency and $\nu_s(t)$ depends on the change rate of $\tau_s(t)$.
If the parameters can be treated as approximately constant within a short time interval T_{stat}, then $c_s(t) \approx c_s$, $\tau_s(t) \approx \tau_s$, and $\nu_s(t) \approx \nu_s$. A simple spreading function $\tilde{S}_{\tau,\nu}(\tau,\nu) = \sum_{s=1}^{S} = c_s\delta(\tau-\tau_s)\delta(\nu-\nu_s)$ describes the time dispersion and the frequency dispersion of sum of S MPCs. Analogously to eq. (2.3), the noise-free sparse TVTF simplifies to

$$\tilde{H}(t,f) = \sum_{s=1}^{S} c_s e^{j2\pi(t\nu_s - f\tau_s)} \quad \text{for} \quad 0 \le t < T_{\text{stat}}. \tag{2.9}$$

It is common to specialize the general model in eq. (2.9) to a model with distinct groups of paths, e.g. $1 \le s < S$ are MPCs with at least a single bounce each and $s = S$ is

the LOS path (if present). This is a simple interpretation of plane waves arriving via different physical paths, where each path has a distinct complex-valued path amplitude c_s, propagation delay τ_s and Doppler shift ν_s. One goal is to estimate the parameters $S \in \mathbb{N}$, $[c_1 \ \dots \ c_S]^{\mathrm{T}} \in \mathbb{C}^S$, $[\tau_1 \ \dots \ \tau_S]^{\mathrm{T}} \in \mathbb{R}_+^S$, and $[\nu_1 \ \dots \ \nu_S]^{\mathrm{T}} \in \mathbb{R}^S$, to completely describe the LTV channel within T_{stat}.
With regard to the discrete MPC model in eq. (2.7), the delay parameter $\tau_s(t)$ associated with MPCs varies only slowly with time. It follows from $\nu_{\max}\frac{1}{\Delta f} \ll 1$, that phase drifts due to Doppler shifts in eq. (2.9) allow a piecewise approximation $e^{j2\pi t\nu} \approx e^{j2\pi kT\nu}$ for $t \in [(k-1)T, kT]$.
For $\nu_{\max}\frac{1}{\Delta f} \ll 1$, self-interference is negligible during the duration of one symbol [52], [94, Assumption A3)]. Therefore, multiple measurements taken sequentially in time need to be acquired to resolve multiple Doppler frequencies sufficiently well [3].

2.3.4 Directional and Polarimetric Channel

Wireless channels can include further degrees of freedom into their models, e.g. with direction of departure, direction of arrival, or polarization information. Those additional degrees of freedom are necessary for a more holistic characterization of the wireless channel. The spatial filtering due to directional antennas employed at mm-wave effectively changes the perceived channel of a wireless communications system. Therefore, it is important to define the scope of the wireless channel in a concise way.
Directional channel models are useful for an antenna independent analysis of measurements [95]. However, deriving empirical directional channel models from measurements is difficult in practice, especially for mm-wave and higher frequencies, due to limited stability of the measurement system [96], [97].
I consider the antennas as a part of the propagation channel for the analysis in this thesis. The employed antennas are directional at one end and their beams have fixed steering angles. The remaining antenna on the other side is omnidirectional. All employed antennas have linear polarization and are mounted for vertical polarization on both ends.

2.3.5 Underspread Assumption

It is important to obtain knowledge of the wireless channel by means of channel sounding either during operation to enable reliable communication, or as part of a broader characterization to provide a representative description for channel modeling. This identification is more difficult for time-varying channels than for time-invariant channels.
Stationary signals have a useful frequency representation known as the spectrum of the signal. The vast number of available tools for a treatment in the frequency domain facilitates signal processing for stationary signals. Treating nonstationary signals can be more difficult. For nonstationary signals with short-time stationarity, the short-time Fourier transform (STFT) is a useful method to describe the signal with a time-varying

frequency representation. The short-time Fourier transform (STFT) applies a sliding time window $w(t)$ to the whole signal to select only a segment, for which the Fourier spectrum is calculated. The result is a time dependent spectrum of the signal.
The STFT of $s(t)$ is

$$F_s(t, f; w) = \int_{-\infty}^{\infty} s(t')w^*(t' - t)e^{-j2\pi ft'}\mathrm{d}t'. \tag{2.10}$$

If the product of effective length in the delay domain and effective spectral bandwidth, as the dual of the time domain, is sufficiently small, then tools from stationary analysis can be applied within sufficiently short time intervals including frequency domain concepts [88, Ch. 2].
The vague requirement of short-time stationarity of a signal or system, e.g. quasi-stationary channels [81], gives rise to a more precise concept of underspread systems and their respective calculus [86].
A LTV system is underspread if its spreading function is nonzero only in a small region in delay-Doppler [86]. However, for a real wireless channel, long propagation delays are possible and paths with multiple bounces may cause Doppler shifts of multiple times the involved velocities. The spreading function for a real wireless channel is nonzero almost everywhere in such a scenario. In an alternative definition, $H(t, f)$ as in eq. (2.2) is an approximate time-frequency transfer function for underspread LTV systems and the approximation error is bounded by moments of the spreading function [86]. This approximation has the advantage that the moment based underspread definition is compatible with a real wireless channel.
The received signal for an underspread system is [86]

$$r(t) \approx \int_{t_0}\int_{f_0} F_s(t_0, f_0; w)H(t_0, f_0)w(t - t_0)e^{j2\pi f_0 t}\mathrm{d}t_0\mathrm{d}f_0 \tag{2.11}$$

and the STFT of the received signal is [86]

$$F_r(t, f; w) \approx F_s(t, f; w)H(t, f). \tag{2.12}$$

Here, $H(t, f)$ represents a time-varying filter operation on $s(t)$ in the frequency domain. It follows from $\nu_{\max}\frac{1}{\Delta f} \ll 1$ that phase drifts due to Doppler shifts in eq. (2.9) allow a piecewise approximation $e^{j2\pi t\nu} \approx e^{j2\pi kT\nu}$ for $t \in [(k-1)T, kT]$.
For $\nu_{\max}\frac{1}{\Delta f} \ll 1$, self-interference is negligible during the duration of one symbol [52], [94, Assumption A3)]. Therefore, multiple measurements taken sequentially in time need to be acquired to resolve multiple Doppler frequencies sufficiently well [3].
Compared to eq. (2.3), the sampled doubly selective channel $H[k, l]$ is the two-

dimensional DFT of a smoothed spreading function $S_{\tau,\nu}[l',k']$

$$H[k,l] = \sum_{l'=0}^{N_\tau-1}\sum_{k'=0}^{N_\nu-1} \frac{S_{\tau,\nu}[l',k']}{\sqrt{N_\nu N_\tau}} e^{j2\pi(\Delta\nu T_R k k' - \Delta\tau\Delta f l l')},$$
$$S_{\tau,\nu}[l',k'] = \sum_{l=0}^{N_\tau-1}\sum_{k=0}^{N_\nu-1} \frac{H[k,l]}{\sqrt{N_\nu N_\tau}} e^{j2\pi(\Delta\nu T_R k k' - \Delta\tau\Delta f l l')}, \tag{2.13}$$

with delay index l', delay resolution $\Delta\tau = \frac{1}{B}$, signal bandwidth B, Doppler index k', number of time snapshots N_ν, number of frequency samples N_τ, and Doppler resolution $\Delta\nu = \frac{1}{N_\nu T_R}$. The DFT relation in eq. (2.13) implies, that the channel is two-dimensional periodic, which is most likely not the case. Similar to $S_{\tau,\nu}(\tau,\nu)$, the smoothed spreading function $S_{\tau,\nu}[l',k']$ describes the dispersion of the signal in the delay-Doppler domain and was found to have an approximate sparse support in vehicular mm-wave scenarios due to employed directive antennas [8] and sufficient bandwidth for resolving arrivals in time [41].

Finite symbol lengths, limited bandwidth, employed pulse-shaping, and point-scatterer model mismatch lead to practical limits of a sparse representation of the spreading function [49]. Already for point-scatterers, grid-mismatch of the sampled wireless channel manifests itself as DFT leakage since their discrete delay and Doppler naturally are not exactly located on DFT bins.

A sparse representation of the approximate sparse spreading function is nonetheless desirable for simpler description of the propagation channel. A structured sparse channel model is advantageous in developing simpler channel tracking algorithms [41].

While the channel needs to fulfill the underspread condition, the choice of sampling parameters for pilot-based channel sounding method in eq. (3.9) defines the limits for identifying delay and Doppler. For a lower rate of pilots in time, a channel snapshot period $T_\mathrm{R} \geq T$ is sufficient as long as $\nu_\mathrm{max} \leq \frac{1}{2T_\mathrm{R}}$ is fulfilled [76, eq. (8.5)].

3 Vehicular Millimeter-Wave Channel Sounding

The measurement process of obtaining channel realizations is known as channel sounding. I carry out a measurement campaign to investigate the mm-wave channel in a V2I scenario. In this chapter, I describe channel sounding using a multicarrier principle and the preprocessing steps to retrieve the data under investigation. The extension to multiple channels in the frequency domain allows simultaneous channel sounding of multiple transmit chains. I describe the resolution limits of the channel sounder and the limited cross-channel isolation in section 3.3.2.
The measurement data obtained from the channel sounder is then further analyzed in terms of the small-scale fading analysis of received signal in chapter 4, the identification of scatterer in the delay-Doppler domain in chapter 5, and the use of sparse methods for identification of scatterers in chapter 6.

3.1 Channel Sounding

The focus at channel sounding is on the properties of the radio propagation channel to identify adequate models and estimate the model's parameters and statistics. The availability of adequate models enables research and development on future wireless communications systems. Channel estimation can be understood as a subset of this channel sounding process, e.g. for parameter estimation, or an integral part of an already deployed communications system to obtain channel state information to adapt adjustable parameters[1]. This thesis focuses on the former aspect.
The measurement device for channel sounding is known as the channel sounder. The task of the channel sounder is to excite the wireless channel with a known signal, which covers the frequency spectrum of interest, and to measure the channel's "response".
Popular channel sounder architectures for mm-wave employ vector network analyzers, sequence correlation, or chirp generation [98]. For suitability as a sounder for vehicular channels in realistic environments, the rate of obtaining channel snapshots must be sufficiently high for the chosen scenario, which is difficult to achieve for some architectures, e.g. for vector network analyzers. Therefore, for the analysis in this thesis I have chosen a

[1] Obtaining channel state information for a communications system through channel estimation is often also ambiguously named channel sounding.

multicarrier channel sounding technique which employs sequence correlation. The multicarrier technique is especially well-suited for software defined radio based measurement systems due to their discrete sampling hardware architecture.

3.2 Multicarrier System Channel Sounding

The multicarrier approach for channel sounding relies on transmitting a known signal and correlate the received signal at a RX. The transmit signal $s(t)$ is composed of a known reference sequence $p[k,l]$ and transmit pulse $g_{k,l}(t)$ as

$$s(t) = \sum_{k} \sum_{l=0}^{N_\tau - 1} p[k,l] g_{k,l}(t), \tag{3.1}$$

where k is the discrete time index, l is the frequency index. The transmit pulse is the building block of the signal and defined as

$$g_{k,l}(t) = g(t - kT) e^{j2\pi l \Delta f t}, \tag{3.2}$$

where T is the time spacing and Δf is the subcarrier spacing. The RX calculates the demodulated sequence

$$r[k,l] = \int_t r(t) \gamma^*_{k,l}(t) \mathrm{d}t, \tag{3.3}$$

from the received signal $r(t)$ with matched filtering with receive pulse

$$\gamma_{k,l}(t) = \gamma(t - kT) e^{j2\pi l \Delta f t}. \tag{3.4}$$

For a multicarrier system with rectangular pulses and a sufficiently dispersion-underspread channel, estimates $\hat{H}[k,l]$ for the LTV propagation channel transfer function $H[k,l]$ at discrete time-frequency points (kT, lF) are calculated as [53, eq. (1.82)]

$$\hat{H}[k,l] = \frac{r[k,l]}{p[k,l]} = H[k,l] + z'[k,l], \tag{3.5}$$

where the error term $z'[k,l]$ includes noise and self-interference. The reference sequence $p[k,l]$ is derived from a back-to-back calibration step [99] to compensate for the measurement hardware to a certain degree, e.g. the transfer functions of the TX's and RX's analog frontends excluding their antennas. For multichannel sounders, each TX-RX pair i needs separate back-to-back calibrations, leading to separate reference sequences $p_i[k,l]$. The channel sounder measurements are limited by noise and the RX SNR in this thesis is defined in dB as

$$\mathrm{SNR}[k] = 10 \log_{10} \left(\frac{\sum_l |r[k,l]|^2}{\sigma^2} \right), \tag{3.6}$$

where σ^2 is the RX noise variance. For the employed bandwidths in this thesis, σ^2 is assumed homogenous across frequency.
The duration T is the time support of the pulse, and it restricts the maximum unambiguous propagation delay, i.e. the maximum excess delay $\tau_{\max}$ defined by the difference between maximum and minimum propagation delay [76, Sec. 6.2.2]. On one hand, T must be large enough for a channel with $\tau_{\max}$, on the other hand, shorter T reduces self-interference due to time-variance, i.e. presence of Doppler shifts.
The product of $\tau_{\max}$ and maximum Doppler shift $\nu_{\max}$ is critical in identifying the channel. Employing eq. (3.5) requires a sufficiently underspread channel, i.e.

$$\tau_{\max}\nu_{\max} \ll 1. \tag{3.7}$$

Most practical vehicular wireless channels fulfill the underspread condition [53, Sec. 1.5.1].
The inverse DFT transform of eq. (3.5) provides an discrete sample estimate of the LTV channel impulse response (CIR)

$$\hat{h}[k, l'] = \frac{1}{N} \sum_{l=0}^{N_\tau - 1} \hat{H}[k, l] e^{j2\pi l l'/N_\tau}, \tag{3.8}$$

with the delay tap indices $l' = 0, \ldots, N_\tau - 1$. Note that $\hat{h}[k, l']$ has regular spaced delay taps and suffers from DFT leakage, unlike eq. (2.4) or eq. (2.7). Furthermore, the delay taps spacing $\Delta\tau = \frac{1}{N_\tau \Delta f}$ is the dual of the measurement bandwidth, which influences delay resolution.

3.2.1 Data Segmentation

I define a time-frequency limited and discrete TVTF $\hat{H}[k, l; t_b]$ from the the discrete TVTF estimates $\hat{H}[k, l]$ in eq. (3.5) as

$$\hat{H}[k, l; t_b] = \hat{H}[k + \tfrac{t_b}{T_{\mathrm{R}}} - \tfrac{N_\nu}{2}, l], \quad k = 0, \ldots, N_\nu - 1, \tag{3.9}$$

with N_ν channel snapshots in time at channel snapshot period T_{R}, N_τ samples in frequency, limited to observation time $T_{\mathrm{obs}} = N_\nu T_{\mathrm{R}}$, and centered at time t_b and frequency f_c. I construct a corresponding sample matrix $\mathbf{Y}[t_b] \in \mathbb{C}^{N_\nu \times N_\tau}$ from eq. (3.9) for each time-frequency region t_b as

$$\mathbf{Y} = \begin{bmatrix} \hat{H}[0, 0; t_b] & \ldots & \hat{H}[0, N_\tau - 1; t_b] \\ \vdots & \vdots & \vdots \\ \hat{H}[N_\nu - 1, 0; t_b] & \ldots & \hat{H}[N_\nu - 1, N_\tau - 1; t_b] \end{bmatrix}. \tag{3.10}$$

In situations where the snapshot period is sufficiently short such that $T_{\mathrm{R}} \ll \frac{1}{2\nu_{\max}}$, the sample matrix $\mathbf{Y}[t_b]$ can be downsampled by de-interleaving $N \in \mathbb{N}$ channel snapshots in

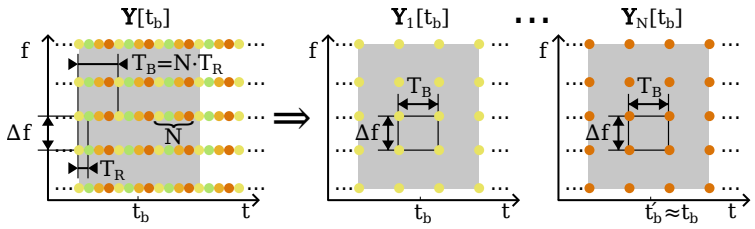

Figure 3.1: Downsampling of the time-frequency sample matrix $\mathbf{Y}[t_b]$ to create multiple channel snapshots $\mathbf{Y}_n[t_b]$ approximately centered at time t_b.

time into multiple sample matrices $\mathbf{Y}_n[t_b] \in \mathbb{C}^{(N_\nu/N)\times N_\tau}$ as shown in fig. 3.1. Each $\mathbf{Y}_n[t_b]$ with $n = 1 \ldots N$ covers roughly the same time-frequency region t_b and the reduced channel snapshot period is $T_{\mathrm{RR}} = NT_{\mathrm{R}}$. If the channel is approximately ergodic within T_{RR}, then those multiple channel snapshots $\mathbf{Y}_n[t_b]$ form an ensemble for a specific t_b, although with some degree of time-smoothing. The ensemble average of snapshots is used for coherent averaging in section 3.3.3.

In the following, I treat each time-frequency region t_b as independent and write only $\mathbf{Y}_n$ for ease of notation. If only one channel snapshot is available per t_b, $\mathbf{Y}_n$ with $n \in \{1\}$ is simply written as $\mathbf{Y}$.

3.3 Multichannel Sounding

Channel sounding relies on an excitation of the channel and its response is measured at the RX. It is straight forward to extend the measurement to multiple RXs if appropriate hardware is available. For channel sounding with more than one TX, it is necessary to distinguish between the excitations due to the individual TXs.

Time division multiplex schemes at the TXs are quite common [95], [100] for multiple-input multiple-output channel sounding and they divide the measurement task into multiple single-input single-output or single-input multiple-output measurements within the coherency time of the wireless channel.

Frequency division multiplex (FDM) schemes allocate different parts of the frequency spectrum to different TXs to allow simultaneous measurement with all TXs. For large bandwidths, an interleaved allocation in frequency keeps the difference between the respective center frequencies small [101]. The frequency spacing between different TXs needs to take phase noise into consideration, which is especially pronounced for mm-wave equipment [102] and which could degrade the SNR of a measurement if the frequency spacing is too low [103].

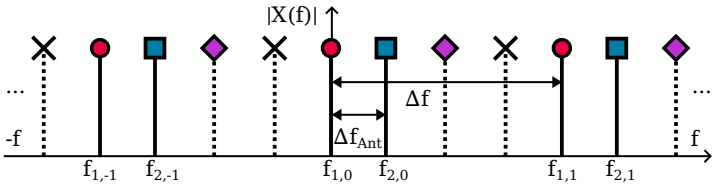

Figure 3.2: Baseband spectrum of sum of interleaved multitone signals for four TXs. Antenna frequency spacing Δf_{Ant} and tone spacing $\Delta f = 4\Delta f_{\text{Ant}}$.

3.3.1 Multitone Signal

A common excitation signal is a multitone signal which is the sum of several sinusoids with distinct frequencies distributed over the whole bandwidth of interest [3]. The complex baseband model of the multitone signal is

$$x(t) = \frac{1}{N} \sum_{l=0}^{N-1} e^{j2\pi \Delta f l t + j\phi_l}, \tag{3.11}$$

with time t, number of tones N, tone spacing Δf, and initial phases ϕ_l. The choice of ϕ_l has an influence on the peak to average power ratio (PAPR) of the signal and is often chosen quadratic for low PAPR [99]. A low peak to average power ratio of the transmit signal is beneficial in minimizing the deviation from the quiescent point of the transmit power amplifier and thus lower the influence of non-linearities.
I set ϕ_l according to a Zadoff-Chu sequence of length N, which are polyphase codes with good autocorrelation properties, to keep PAPR low [104]. The multitone signal with $\Delta f = \frac{1}{NT}$ can be interpreted as an endless loop of the same OFDM symbol consisting only of pilots. Due to the looping, a cyclic-prefix of the OFDM is inherent to the signal such that the time spacing of the transmit pulse is $T = \frac{1}{\Delta f}$. Therefore, multitone channel sounding has strong similarities to OFDM channel estimation and is often named OFDM-based channel sounding [9].
By assigning a frequency offset Δf_{Ant} between antennas, simultaneous channel sounding with multiple TXs is possible [8], [101], [105]. The TX dependent version of the signal of eq. (3.11) is then defined as

$$x_i(t) = \frac{1}{N} \sum_{l=0}^{N-1} e^{j2\pi(\Delta f l + i\Delta f_{\text{Ant}})t + j\phi_{il}}, \tag{3.12}$$

where the initial phases ϕ_{il} are independent for each TX i.
The RXs split up the received signal into TX-RX pairs in the frequency domain based on the previously defined frequency allocation. Figure 3.2 shows the interleaved tones in the spectrum of the sum signal of multiple TXs when $\Delta f = 4\Delta f_{\text{Ant}}$. If the block length N_R for DFT-based processing is a multiple of $N_{\text{Ant}} = \frac{1}{\Delta f_{\text{Ant}} T}$ samples, then the separation is possible by selecting the corresponding DFT bins. Furthermore, increasing N_R decreases spectral leakage between DFT bins.

Multichannel Data Segmentation. For multicarrier multichannel sounding, the calculation of estimates $\hat{H}_{ij}[k,l]$ is analogous to eq. (3.5) but with separate received signals $r_i[k,l]$ and separate calibration data $p_{ij}[k,l]$ of TX i and RX j. The estimated TVTF of the wireless channel is only available for those time-frequency samples k and l with corresponding excitations by a TX. If intermediate samples are required, then an interpolation with a lowpass filter provides good estimates for those interpolated samples of dispersion-underspread channels [53, Sec. 1.7.2].

3.3.2 Resolution Limits

Ambiguity Function

A fundamental resolution limit for channel sounding is given by the complex (cross-)ambiguity function $A_{x_1,x_2}(\tau,\nu)$ [3] defined as

$$A_{x_1,x_2}(\tau,\nu) = \int_t x_1(t)x_2^*(t+\tau)e^{j2\pi\nu t}dt \tag{3.13}$$

which describes the cross-correlation between signal $x_1(t)$ and $x_2(t)$ for a given frequency shift ν. For $x_1 = x_2$, $A_{x_1}(\tau,\nu) = A_{x_1,x_1}(\tau,\nu)$ is the autoambiguity function. A fast decay of the sounding signal's autocorrelation $|A_{x_1}(\tau,0)|$ is desirable to achieve a virtual sounding signal, which approximates a Dirac impulse [106]. Moreover, $|A_{x_1}(\tau,\nu)|$ should be small for $(\tau,\nu) \neq (0,0)$ for high resolution in delay-Doppler [87], [94]. The autoambiguity function of a short-timed sounding signal, e.g. a single OFDM symbol, may provide resolution capability in delay and show marginal decay for frequency shift. In that case, a RX matched to the signal is robust to frequency shifts and at the same time poor in resolving those shifts. Multiple repetitions N of the sounding signal are needed for a resulting ambiguity function with sufficient decay in frequency shift. If the employed signal is periodic, the ambiguity function evaluated over one period T easily extends to multiple periods defined as [107]

$$A_{Nx_1}(\tau,\nu) = A_{x_1}(\tau,\nu)\frac{\sin(\pi\nu NT)}{N\sin(\pi\nu T)}e^{j\pi\nu(N-1)T}$$

Consequently, taking multiple periods of the signal influences the ambiguity function in the frequency shift domain, but it also increases the total observation time $T_{\text{obs}} = NT$. The autoambiguity function $|A_{x_1}(\tau,\nu)|^2$ of a sounding signal employed during the measurement campaign in [8] is shown in fig. 3.3 with $T = 84\,\mu\text{s}$ for different number of repetitions $N = 1$, $N = 10$, and $N = 100$. The signal is a multitone signal with 21 tones of constant magnitude. The cut $|A_{x_1}(\tau,0)|$ shows 20 nulls between $\tau = 0\,\text{ns}$ and the autocorrelation period at $\tau = \tau_{\max} = 210\,\text{ns}$. The nulls are independent of N, which are also sampling points in the delay domain. For $N = 1$, there is no recognizable decay in frequency shift. Nulls in frequency shifts appear with increasing N, which are then

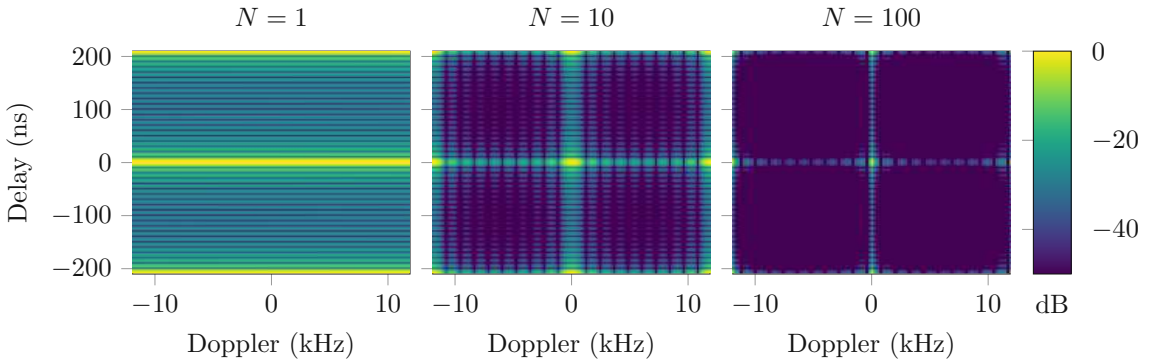

Figure 3.3: Autoambiguity function $20 \log_{10} |A_{x_1}(\tau, \nu)|$ of sounding signal in [8].

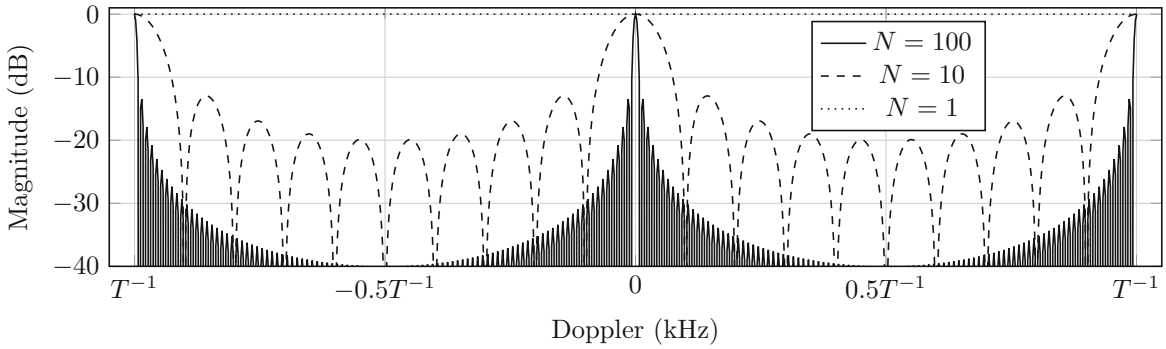

Figure 3.4: Zero-delay cut of the autoambiguity function $20 \log_{10} |A_{x_1}(\tau, \nu)|$ fig. 3.3 for $N = 1$, $N = 10$, and $N = 100$.

sampling points in the Doppler domain. For $N = 100$, the sidelobes fall off already considerably.
The zero-delay cut $|A_{x_1}(0,\nu)|^2$ is shown in fig. 3.4, where the ambiguity stays at 0 dB for $N = 1$, sidelobes fall off to -20 dB for $N = 10$, and -40 dB for $N = 100$. The width of the lobe around $|A_{x_1}(0,0)|^2$ is important in the ability to localize the shift in time and frequency of the received signal. For channel sounding with a matched filter, the resolution of the channel estimate is on the order of B^{-1} for delay and T_{obs}^{-1} [94]. A reason to deviate from the matched filter is to suppress sidelobes at the cost of reduced resolution [108] [109, Ch. 10].

Ambiguity Function for Multicarrier System

As described in section 3.3.2, the cross-correlation of the transmit and receive signal should have a Dirac-like shape. An estimate of the channel is then obtained by sampling the channel with this virtual Dirac train [106].
If the channel is sufficiently underspread, then the relevant ambiguity function for a multicarrier system depends on the employed transmit pulse $g(t)$ and receive pulse $\gamma(t)$ [87]

$$A_{g,\gamma}(\tau,\nu) = \int g(t)\gamma^*(t-\tau)e^{-j2\pi\nu t}dt,$$

where the problem remains to design appropriate $g(t)$ and $\gamma(t)$.

Back-to-back Calibration

The ideal sounding signal undergoes distortions in the signal chain of the channel sounder from source to received samples which are not exclusively due to antennas or the wireless channel. Therefore, the ambiguity function of the received signal after back-to-back connection serves as a reasonable performance test for the whole channel sounder [3]. The transmit powers during the measurement campaign must be the same as the ones during calibration to operate the TX at approximately the same quiescent point. Adequate attenuators between RX and TX ensure the operation of the RX at the same dynamic range as during the measurement campaign.
Let $a_i[k]$ and $a_j[k]$ be the recorded samples at channel i and channel j, respectively, when each TX-RX pair is connected separately back-to-back via cables and attenuators. The employed transmit and receive signal define a channel's autoambiguity $A_{a_i}(\tau,\nu)$. In the process of designing a transmission system, the channel sounder's 20 dB-width of $A_{a_i}(\tau,0)$ should be smaller than the reciprocal of the design bandwidth as rule of thumb [110].
If multiple channels transmit at the same time, interchannel interference must be considered. The cross-ambiguity functions $A_{a_1,a_2}(\tau,\nu)$ and $A_{a_2,a_1}(\tau,\nu)$ describe the interchannel interference between channel 1 and channel 2. This interference influences the identifiability of the channel additional to ambiguity $A_{a_i}(\tau,\nu)$ and is ideally small for all τ and

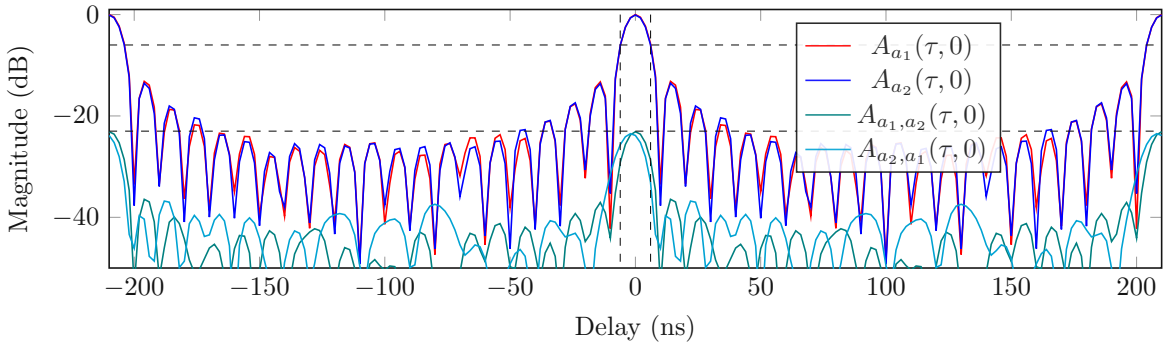

Figure 3.5: Zero-Doppler cut of the autoambiguity functions $20\log_{10}|A_{a_1}(\tau,\nu)|$ and $20\log_{10}|A_{a_2}(\tau,\nu)|$ and their cross-ambiguity functions $20\log_{10}|A_{a_1,a_2}(\tau,\nu)|$ and $20\log_{10}|A_{a_2,a_1}(\tau,\nu)|$ of the recorded signals $a_1[k]$ and $a_2[k]$ at back-to-back calibration. Record length is 10 periods of a single OFDM symbol. Matched filtering with rectangular pulses leads to a 6 dB width of $\frac{1.21}{B} = 12.1\,\text{ns}$.

ν. For two simultaneously transmitted signals at different channels, their cross-channel isolation $I_{ij}(\nu)$, defined similar in [111] as

$$I_{ij}(\nu) = \min_{\tau} \frac{|A_{a_i}(0,0)|^2}{|A_{a_i,a_j}(\tau,\nu)|^2}, \tag{3.14}$$

is an important measure for the ability to suppress contributions from the cross-channel j to the actual channel of interest i.
Figure 3.5 shows the autoambiguity functions of two channels from the back-to-back calibrations of the employed FDM channel sounder and their cross-ambiguity functions. For both channels, cross-channel isolation $I_{12}(\nu)$ and $I_{21}(\nu)$, defined in eq. (3.14), is at least 23 dB.

3.3.3 Processing Gain

Estimates of the TVTF obtained from a channel sounder can be enhanced by coherently combining samples of a received waveform. Processing gain through averaging, i.e. averaging gain, is achieved by calculating the average received waveform of N_{avg} repetitions within a specified coherent averaging time. In doing so, the magnitude of non-coherent components of the received waveform, e.g. white noise, is reduced compared to coherent components. The theoretical averaging gain G_{avg} depends directly on the number of averaged repetitions N_{avg}. The achievable averaging gain depends heavily on the phase noise performance of the channel sounder, which deteriorates coherent components.
The resulting average TVTF is smoothed over the coherent averaging time[2], and sampled

[2]Coherent integration time is a similar concept in radar applications, cf. [112].

at a snapshot period T_R, which limits the maximum detectable Doppler shift ν_max to

$$T_\mathrm{R} \leq \frac{1}{2\nu_\mathrm{max}}. \tag{3.15}$$

Coherent averaging can be interpreted as the zero-Doppler bin of a DFT over N_avg samples with a rectangular window. Therefore, this zero-Doppler bin subsumes contributions from the Doppler spectrum according to Dirichlet's kernel[3].

[3]For odd N_avg, Dirichlet's kernel is $\mathcal{D}_{N_\mathrm{avg}}(\nu T_\mathrm{R}) = \frac{1}{N_\mathrm{avg}} \sum_{k=-(N_\mathrm{avg}-1)/2}^{(N_\mathrm{avg}-1)/2} e^{j2\pi k \nu T_\mathrm{R}}$ [85, Eq. (17c)].

4 Channel Variability

Models for V2I channels can assume the presence of a LOS component, when proper placement of road-side units (RSUs) is ensured. Sparse models with only two paths are then able to describe most of the relevant fading characteristics of V2I mm-wave channels [113]. The availability of high bandwidths at mm-wave frequencies improves the ability of a communications system to resolve MPC in delay. Consequently, less components interfere at the RX within a single delay tap. The required minimum bandwidth to resolve ground reflections and the LOS component is attainable for mm-wave [113]. Published standards on mm-wave radio access technologies, e.g. 802.11ad/ay or 3GPP 5G NR FR2, provide high channel bandwidth in most configurations. However, the choice of some configurations with medium channel bandwidths leads to insufficient delay resolution to resolve ground reflections and the LOS component. Furthermore, insufficient sidelobe suppression of employed directional beams could cause dominant specular components, e.g. caused by the vehicle itself, which require excessive bandwidth for resolvability.

In this chapter, I provide an analysis of the fading statistics of the LOS delay tap in the case of medium channel bandwidth. I propose a model for three dominant specular components and diffuse components with a specific phase relationship encountered in V2I mm-wave channels. The specific phase relationship enables an approximate description of the envelope statistic within a limited region with only two instead of three dominant specular components, i.e. the two-wave with diffuse power (TWDP) fading model. This simplified three-wave with diffuse power model is applicable for a local statistical description of the envelope when the magnitudes of the three waves are approximately stationary locally. I describe the coefficient of variation (CV) in section 4.1.1 as metric for variability of the received signal envelope. I introduce the multiple specular components model [78] in section 4.1.2, which models the envelope distribution as a conditional Rician distribution [79]. Section 4.1.3 describes the special case of TWDP fading. Restriction of the phase relationship as in the two wave case [114] allows a special case of a simplified three-wave with diffuse power model in section 4.1.4, relevant for V2I mm-wave. Rician and TWDP fading can be expressed in closed-form [114] in terms of the coefficient of variation (CV) in section 4.1.6. I introduce a relevant V2I mm-wave communications scenario in section 4.3. I provide simulations in section 4.4 and a measurement campaign in section 4.5, assessing the impact of beam elevation on the CV and fits of CDFs fits dependent on the vehicle's position. I provide a discussion at the end of the chapter in section 4.6

4.1 Model

Statistical moments, e.g. the mean and the variance, allow a nonparametric description of the statistics of the received signal envelope. An estimation of those moments from measurements is possible without the assumption of a specific underlying statistical model. However, the knowledge of an appropriate underlying statistical model for the received signal envelope, i.e. knowledge of a distribution's CDF, enables the synthesis of data from the model for simulation purposes.
Parametric CDFs provide a parsimonious description of the statistics of the received signal envelope. Although parametric models and a transition of their parameter values often give useful insights, the applicability of a model needs to be tested on measurements.

4.1.1 Coefficient of Variation

The CV is a moment-based metric for the variability of a real valued random variable X defined as the ratio of standard deviation to mean[1]

$$\mathrm{CV} = \frac{\sqrt{\mathbb{E}\{X^2\} - \mathbb{E}\{X\}^2}}{\mathbb{E}\{X\}}. \tag{4.1}$$

The CV is related to a similar metric called amount of fading (AF), where $\mathrm{AF} = (\mathrm{CV})^2$ and the random variable is the instantaneous SNR [114], [115]. AF is an important measure for the severity of fading for arbitrary combining schemes for communications receivers [115].

4.1.2 Fading Channel Model with Dominant Specular Components

The Rician fading model is popular for the statistical description of small-scale fading involving a single dominant specular component and diffuse components [3], [76]. For multiple specular components, a complex baseband received signal can be written as [78]

$$R = \sum_{i=1}^{N} V_i e^{j\phi_i} + Z, \quad Z = X + jY, \tag{4.2}$$

where the N complex phasors of amplitudes V_i and random phases ϕ_i are specular components and X and Y are independent and identically distributed (i.i.d.) zero-mean Gaussian random variables with variance $\sigma_x^2 = \sigma_y^2$.

[1] CV is also known as normalized standard deviation.

The envelope $r = |R|$ of the received signal R conditioned on the specular components, e.g. by the modulus squared superposition of the specular components

$$P_N = \left| \sum_{i=1}^{N} V_i e^{j\phi_i} \right|^2 , \tag{4.3}$$

follows a Rician distribution [79]

$$f_{r|P_N}(r) = \frac{r}{\sigma_x^2} e^{-\frac{r^2+P_N}{2\sigma_x^2}} I_0\left(\frac{\sqrt{P_N} r}{\sigma_x^2}\right), \tag{4.4}$$

where $I_0(\cdot)$ is a zeroth-order modified Bessel function. The unconditional PDF $f_r(r)$ of r depends on the distribution of P_N and is derived by the expectation operator [79]. The CDF of r is obtained similarly and given by [79]

$$F_r(r) = 1 - \mathbb{E}_{P_N}\left\{ Q_1\left(\frac{\sqrt{P_N}}{\sigma_x}, \frac{r}{\sigma_x}\right)\right\}, \tag{4.5}$$

where $Q_1(\cdot,\cdot)$ is the Marcum Q–function. For a known distribution of P_N, eq. (4.5) provides a clear method to derive the fading statistics.
In the absence of a dominant specular component, the model degenerates to the Rayleigh fading model. For $N = 1$, eq. (4.2) leads to the well-known Rician distribution of the received signal envelope $|r|$. For $N = 2$, $\sigma_x^2 > 0$, and i.i.d. ϕ_i with uniform distribution over the interval $[0, 2\pi)$, eq. (4.2) leads to a distribution according to TWDP fading, which has no exact closed-form equation [78], cf. section 4.1.3. For $N = 3$, the shape of the distribution can change dramatically compared to $N = 2$, especially for the case of balanced amplitudes [79]. The model provides little benefits in describing the fading behavior in the general case for $N \geq 3$, as it either tends towards Rayleigh fading or Rician fading [78].

4.1.3 Two Wave with Diffuse Power

The TWDP fading model describes the statistics of the signal envelope of the sum of $N = 2$ specular components, V_1 and V_2, and diffuse components Z, cf. eq. (4.2). The shape of the PDF of TWDP fading model is completely specified by the parameters [78]

$$K_{\mathrm{TWDP}} = \frac{V_1^2 + V_2^2}{2\sigma_x^2} \tag{4.6}$$

as the specular to diffuse power ratio, and

$$\Delta_{\mathrm{TWDP}} = \frac{2V_1^2 V_2^2}{V_1^2 + V_2^2}, \tag{4.7}$$

where $1 + \Delta_{\mathrm{TWDP}}$ is the specular peak to specular average power ratio. The model assumes an uniform distribution of the phase difference $\Delta\phi = \phi_2 - \phi_1$. The CDF of r is

$$F_r(r) = 1 - \frac{1}{2\pi} \int_0^{2\pi} Q_1\left(\frac{\sqrt{P_2}}{\sigma_x}, \frac{r}{\sigma_x}\right) \mathrm{d}\Delta\phi, \tag{4.8}$$

where $P_2 = V_1^2 + V_2^2 + 2V_1V_2\cos(\Delta\phi)$. Results for arbitrary distributions of $\Delta\phi$ have been investigated in [114].

4.1.4 Simplified Three-Wave with Diffuse Power

The distribution of instantaneous power of the specular components P_N is required to obtain the fading statistics via the expectation based CDF in eq. (4.5). For $N = 3$ specular components, P_N includes the individual powers V_i^2 and cross-terms as

$$P_3 = V_1^2 + V_2^2 + V_3^2 + 2V_1V_2\cos(\Delta\phi_2) + 2V_1V_3\cos(\Delta\phi_3) + 2V_2V_3\cos(\Delta\phi_3 - \Delta\phi_2). \tag{4.9}$$

A distinct fading pattern is often observed in vehicular wireless channels due to interfering dominant propagation paths with deterministic changes. Path loss changes due to a ground reflection interfering with the LOS are discussed in [116]–[119], where a moving TX or RX within a static environment leads to dependencies between the phases ϕ_i of the specular components. For an empirical analysis of the received signal's CDF, samples need to cover at least the spatial fading period of the deterministic two-ray fading, such that $\Delta\phi_2 = \phi_1 - \phi_2$ of two specular components covers the interval $[0, 2\pi]$.
For $N = 3$, sufficient samples are needed for $(\Delta\phi_3 - \Delta\phi_2, \Delta\phi_2, \Delta\phi_3)$ to cover the interval $[0, 2\pi] \times [0, 2\pi] \times [0, 2\pi]$, which is difficult to obtain in situations where the amplitudes V_1, V_2, and V_3 are also time-varying. However, if the phase relations between the specular components follow a deterministic model, a simplified approach is applicable for eq. (4.4) and eq. (4.5) as follows.

Assumptions. Let $i = 1$ be the LOS component between a moving TX and RX, let $i = 2$ be a specular component due to ground reflection, and let $i = 3$ be a specular component due to a single bounce near the TX or the RX. The magnitudes V_1, V_2, and V_3 of their respective components are constant. The phase differences between the components depend only on the position of the TX on the axis of movement, i.e. the y-axis in the investigated V2I scenario fig. 4.1 later in this chapter.
I assume an affine relation $\Delta\phi_2(y) = c_3\Delta\phi_3(y) + c_2$ with constant c_3, initial phase offset c_2 and, without loss of generality, $\Delta\phi_3(y) - \Delta\phi_2(y) = 0$ to define the $\Delta\phi_3$-dependent P_3 as

$$P_3(\Delta\phi_3) = V_1^2 + V_2^2 + V_3^2 + 2V_1V_2\cos(\Delta\phi_2) + 2V_1V_3\cos(\Delta\phi_3) + 2V_2V_3\cos(\Delta\phi_3(c_3 - 1) + c_2). \tag{4.10}$$

For $c_3 \gg 1$, $\cos(\Delta\phi_3(c_3-1)+c_2) \approx \cos(c_3\Delta\phi_3+c_2) = \cos(\Delta\phi_2)$ and locally for $\Delta\phi_3 \in [\Delta\phi_3 - \frac{\varepsilon}{2}, \Delta\phi_3 + \frac{\varepsilon}{2}]$, the specular power is

$$\tilde{P}_3(\Delta\phi_2; \Delta\phi_3) = \tilde{V}_1^2 + V_2^2 + 2V_2\tilde{V}_1\cos(\Delta\phi_2), \tag{4.11}$$

with $\tilde{V}_1 = |V_1 + V_3 e^{j\Delta\phi_3}|$. If $\Delta\phi_2$ is uniformly distributed in $[0, 2\pi]$, then r has a CDF according to the TWDP fading model with magnitudes $\tilde{V}_1$ and V_2, conditioned on $\Delta\phi_3$. The parameters describing the simplified three-wave with diffuse power are conditioned on $\Delta\phi_3$. Analogously to the TWDP fading model parameters,

$$K_{\text{S3WDP}} = \frac{\tilde{V}_1^2 + V_2^2}{2\sigma_x^2} \tag{4.12}$$

and

$$\Delta_{\text{S3WDP}} = \frac{2\tilde{V}_1^2 V_2^2}{\tilde{V}_1^2 + V_2^2}, \tag{4.13}$$

where $\tilde{V}_1$ replaces V_1 in eq. (4.6) and eq. (4.7).
The reason for covering $\Delta\phi_3$ only within small interval is the short required spatial distance of the obtained samples to treat the magnitudes V_i as constant. This is in agreement with the widespread method of empirical small-scale fading analysis, where only short spatial distances of a few wavelengths are considered [3] due to limited stationary distances, e.g. only 6–23 wavelengths in [33].
The peak instantaneous power of the specular components for $P_3(\Delta\phi_3)$ is $\max\{P_3\} = (V_1+V_2+V_3)^2$ at $\Delta\phi_2 = \Delta\phi_3 = \Delta\phi_3 - \Delta\phi_2 = 0$. Therefore, near the spatial position y where $r(y)^2$ is $\max\{r(y)^2\}$, it is reasonable to assume $\Delta\phi_3 = 0$, $\tilde{V}_1 = |V_1 + V_3 e^{j0}| = V_1 + V_3$, and treat $\Delta\phi_3$ constant within a small interval, whereas an arbitrary r^2 is difficult to relate to specific phases.

4.1.5 Diffuse Power and Noisy Samples

The samples obtained from measurements include not only diffuse components but also noise from various sources, e.g. receiver noise. It is common to employ a complex Gaussian model for diffuse components and receiver noise [120]. Estimation algorithms for small-scale fading parameters can take the knowledge of the receiver noise into account [121].
In a static scenario, the availability of multiple snapshots enables a distinction between receiver noise from diffuse components, where each snapshot likely contains independent receiver noise whereas diffuse components may remain static. However, in a vehicular environment often only a single snapshot is available. Therefore, separating receiver noise from diffuse components is more difficult.

4.1.6 Coefficient of Variation Special Cases

Closed form expressions exist for the CV of several probability distributions. The AF for the TWDP fading model is given in [114] and, transformed here into CV for convenience, defined as

$$\mathrm{CV}_{\mathrm{TWDP}} = \sqrt{\frac{2 + 4K_{\mathrm{TWDP}} + K_{\mathrm{TWDP}}^2 \Delta_{\mathrm{TWDP}}^2}{2(1 + K_{\mathrm{TWDP}})^2}}, \tag{4.14}$$

where K_{TWDP} and Δ_{TWDP} are the parameter which specify the distribution of the TWDP fading model, cf. section 4.1.3. The distribution of the TWDP fading model specializes to a Rician distribution for $\Delta_{\mathrm{TWDP}} = 0$, such that its CV is

$$\mathrm{CV}_{\mathrm{R}} = \sqrt{\frac{1 + 2K_{\mathrm{R}}}{(1 + K_{\mathrm{R}})^2}}, \tag{4.15}$$

with values from $\mathrm{CV}_{\mathrm{R}} = 0$, for Rician K-factor $K_{\mathrm{R}} \to \inf$, to $\mathrm{CV}_{\mathrm{R}} = 1$, for $K_{\mathrm{R}} = 0$, i.e. Rayleigh fading.

4.2 Estimation of Small-scale Fading

The wideband transmission at mm-wave enables certain delay resolution of the wireless channel. The discrete sample CIR $\hat{h}[k, l']$ in eq. (3.8) for multicarrier systems is time-varying with time index k and consists of $l' \in N_\tau$ delay taps. Each delay tap can be modeled as a fading process. Let $\hat{h}_{\mathrm{LOS}}[k]$ be the delay tap associated with the delay τ_{LOS} of the LOS component and $|\hat{h}_{\mathrm{LOS}}|$ its envelope. The empirical CDF of $|\hat{h}_{\mathrm{LOS}}|$ is commonly employed in literature to infer statistical models. First, some candidate parametric CDFs are fitted to the empirical CDF. Then, a goodness-of-fit test is required between the fitted CDFs and another empirical CDF from independent samples.

4.2.1 Kolmogorov-Smirnov Goodness-of-fit Test

The following two hypotheses test a sample x against two distributions,

$$\mathcal{H}_0 : F_x(x) \equiv F_0(x) \quad \text{and} \quad \mathcal{H}_r : F_x(x) \neq F_0(x), \tag{4.16}$$

where $\mathcal{H}_0$ is the hypothesis that the sample drawn from distribution $F_x(x)$ comes from the predefined CDF $F_0(x)$, and the hypothesis $\mathcal{H}_r$, that the sample comes from a different CDF. The Kolmogorov-Smirnov test uses the following test statistic [122]

$$D_n = \sup_x \left| \hat{F}_x(x) - F_0(x) \right|, \tag{4.17}$$

where $\hat{F}_x(x)$ is the empirical CDF of n samples. The test statistic D_n is a random variable independent of $F_0(x)$, cf. [122], with significance level $\alpha = \Pr\{D_n > c \mid \mathcal{H}_0\}$ and

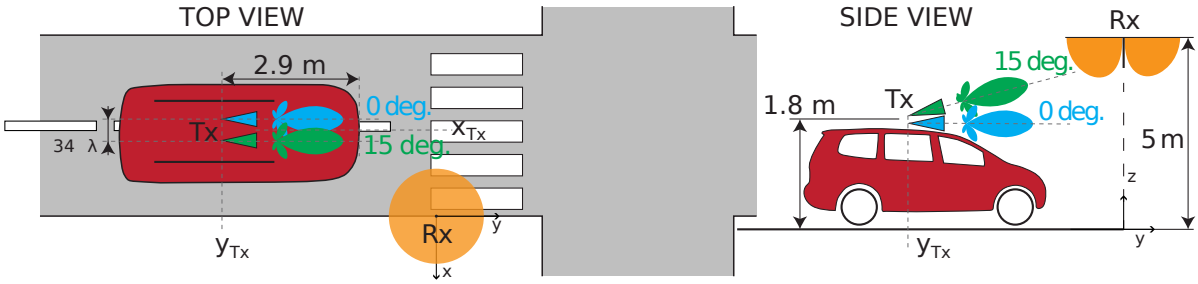

Figure 4.1: Vehicle to infrastructure (V2I) scenario for antenna tilt investigation with TX car moving mainly along y-axis. The origin of the Cartesian coordinate system is below the RX antenna at ground level. The front face center point of the TX platform defines the reference point for the position of the TX car.

a constant c. The Kolmogorov-Smirnov test evaluates the probability $p = \Pr\{D_n > c\}$, where a small value for the p-value casts doubt about the validity of hypothesis $\mathcal{H}_0$. I reject hypothesis $\mathcal{H}_0$ if $p < \alpha$ with the widely employed significance level $\alpha = 0.05$.
For the validity of the Kolmogorov-Smirnov test, it is important that the parameter estimates of $F_0(x)$ and the empirical CDF $\hat{F}_x(x)$ are from independent samples [123]. The authors in [123] consider $n \geq 50$ as a moderate to large sample size and I employ this lower bound for the number of samples during the goodness-of-fit tests on the measurement data. However, the required sample size for rejecting hypothesis $\mathcal{H}_0$ at a given α also depends on D_n [124].

4.3 Simulation and Measurement Scenario

The scenario for assessing the impact of different antenna tilts is a V2I communications urban street scenario with a moving car and a RSU located at a street crossing. A wireless system with a channel bandwidth of 100 MHz communicates at mm-wave frequencies at 60.15 GHz center frequency. This scenario is also interpretable in a mobile communications scope as an urban microcell with a mobile station and a base station, placed at low elevation near the street [6]. A schematic of the scenario is shown in fig. 4.1.
The perceived wireless channel between the car's TX system to the RSU's RX system is under investigation for two antenna beams. One TX antenna emits a beam horizontally, named TX 0°. The second TX antenna emits a beam with a 15° uptilt, named TX 15°. The TX antennas are integrated on a TX platform and mounted on the roof of the car. The RX is positioned at the crossroads of a street canyon, at 5 m height. The RX antenna has an omnidirectional beam pattern and its influence on the perceived channel is considered equal for both employed antennas in this thesis. Furthermore, the employed channel model considers the antennas as an integral part of the channel.
This scenario is the basis for the simulation study in section 4.4 and the measurement campaign in section 4.5.

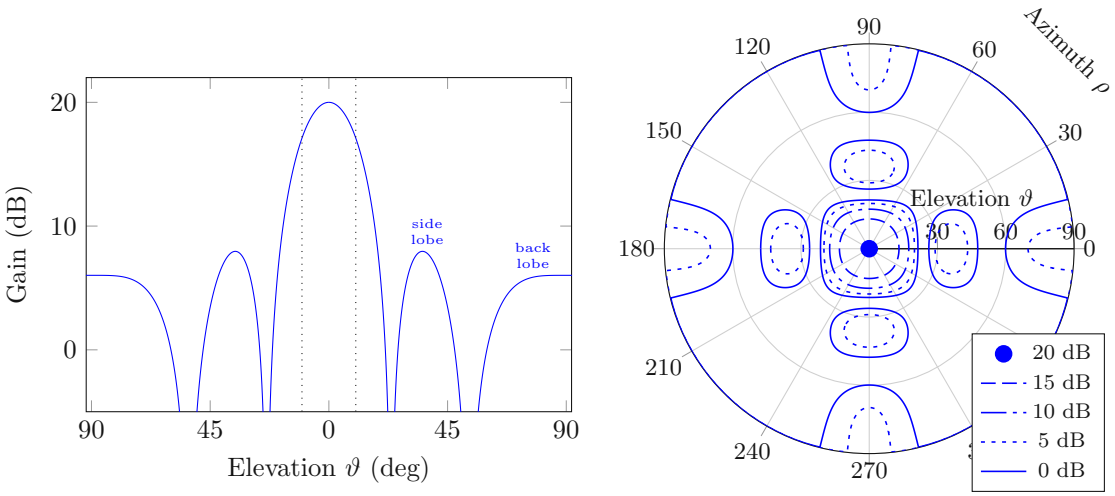

(a) (b)

Figure 4.2: Elevation cut (a) and elevation-azimuth plane (b) of a broadside beam for a 5x5 standard rectangular array, with half power beam width 20.4°. Backlobe is modeled as constant for $\vartheta > 90°$.

4.4 Variability Simulation

I investigate the different antennas in terms of variability of the channel in a simulation of the scenario fig. 4.1. The simulation geometry is modeled after the geometry of the environment of the measurement campaign in section 4.5. I employ 5×5 rectangular arrays with half-wavelength spacing as TX antennas with directional beams. The beam pattern's backlobe has a constant gain for $\vartheta > 0$ but its influence on the simulation is negligible. An elevation cut of the TX array's broadside beam and the elevation-azimuth plane are shown in fig. 4.2 with elevation angle ϑ and azimuth angle ρ.

The broadside beam is directed in driving direction y, where one array is mounted with $\theta = 0°$ and a second array with $\theta = 15°$ uptilt.

Figure 4.3 shows the $y - z$ plane of the simulation scenario with the TX platform for the TX antennas on the roof of the car. The two rectangular arrays are in the $x'' - y''$ plane of their respective antenna coordinate system $x''y''z''$. The elevation tilt angle θ is the angle between the z''-axis and the y'-axis of the TX coordinate system $x'y'z'$. The TX coordinate system changes with respect to the global coordinate system xyz as the car moves along the y-axis, whereas the relations between $x'y'z'$ and the $x''y''z''$ of each TX antenna are constant.

I consider the geometry-based channel model in eq. (2.7) with $S = 3$ dominant paths and an additive complex Gaussian term for diffuse components. The chosen scenario allows to treat the time-varying channel $h(t, \tau)$ as a time-invariant channel $h(y, \tau)$, which depends on the TX position on the y-axis. The component $s = 1$ is the LOS, $s = 2$ is a MPC due

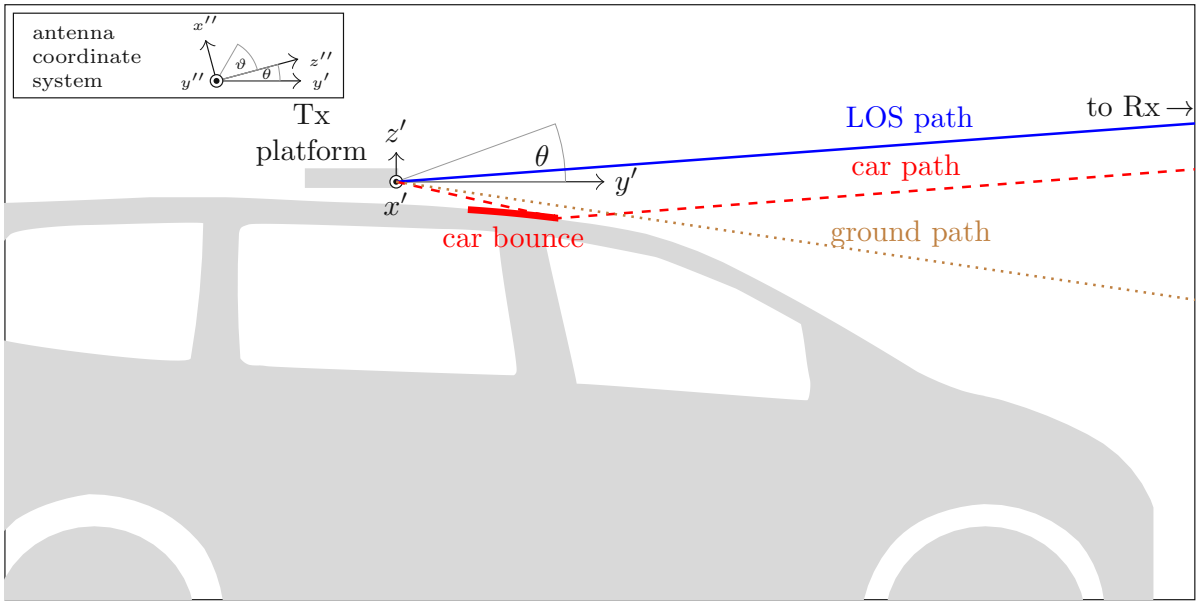

Figure 4.3: Geometric schematic of three paths from TX to RX. A direct LOS path, a ground path due to ground reflection, and a path due to a bounce at the car's roof. The elevation tilt angle θ is shown for TX 15°.

to ground reflection, and $s = 3$ is a MPC due to a possible specular component with a bounce at the roof of the TX car. I model the power of diffuse components independent of TX power and directionality for the sake of simplicity.

4.4.1 Simulation Setup

When treating the delay of a LOS component as deterministic, the wireless system can align the delay domain, such that $\tau_{\mathrm{LOS}}(y)$ is at the center of the LOS delay tap. The delays of the paths $s = 2$ and $s = 3$ in fig. 4.3 are defined by the excess delays $\Delta\tau_s(y)$ measured from $\tau_{\mathrm{LOS}}(y)$, i.e. $\Delta\tau_s(y) = \tau_s(y) - \tau_{\mathrm{LOS}}(y)$. Figure 4.4 shows $\Delta\tau_s(y)$ for a short track along the y-axis for the chosen scenario. The channel bandwidth of the wireless system determines the width of a delay tap. A wireless system is able to resolve the ground path from the LOS path within observed y-positions of the TX at a high channel bandwidth of 800 MHz. At a medium channel bandwidth of 100 MHz, the wireless system is not able to resolve the three paths anymore.
In the unresolved case, the relations of those complex magnitudes play an important role for the variability of the channel. Each path's complex magnitude $c_s(y)$ in the model eq. (2.7) incorporates free space path loss, antenna gain, and reflection coefficient if applicable. Moreover, I incorporate the attenuation due to the bandlimited receive filter into $c_s(y)$, which depends on the excess delay. Figure 4.5 shows the resulting magnitudes $|c_s(y)|$ for the chosen track along the y-axis. Wide variations in direction of departure

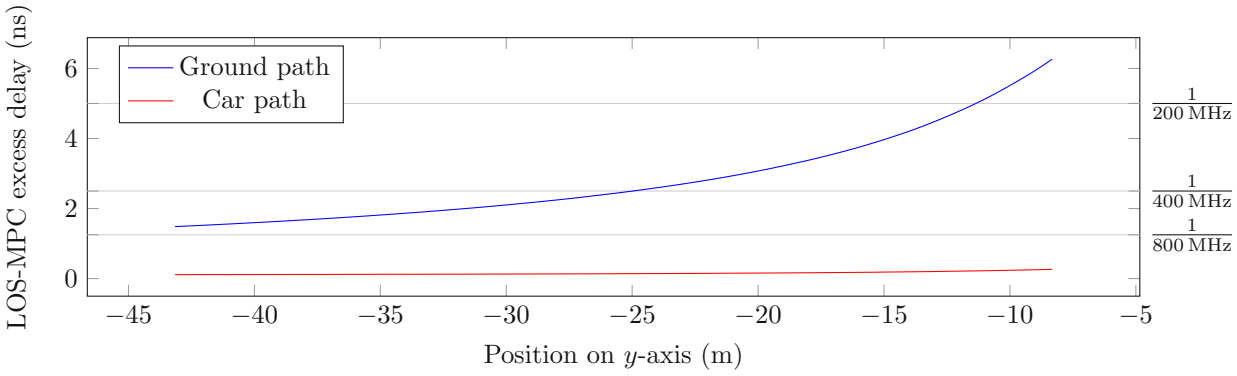

Figure 4.4: Excess delays of ground path and car paths.

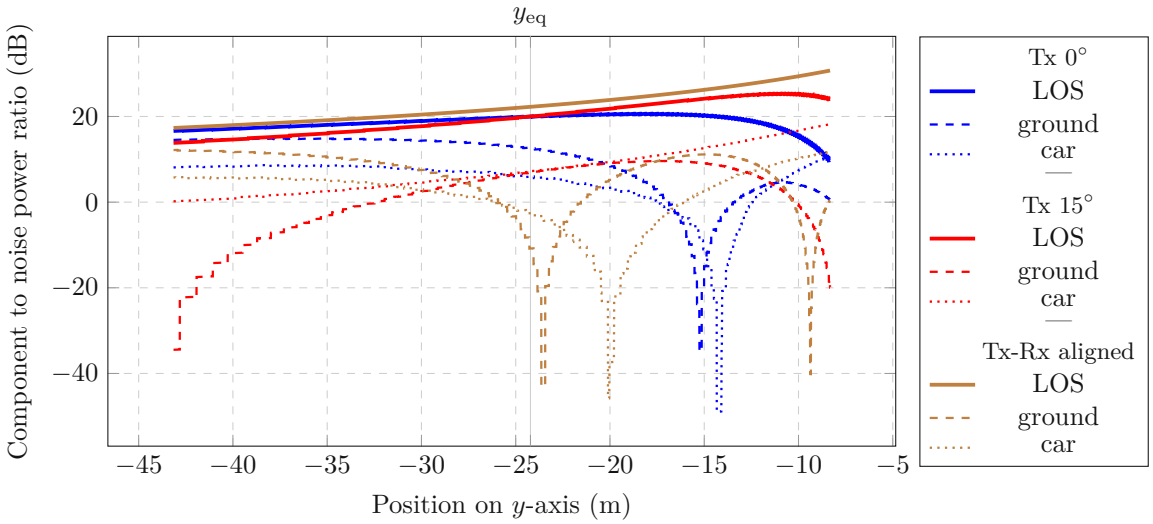

Figure 4.5: Magnitudes $|c_s(y)|$ of the components depending on the TX position on y-axis. The LOS components of both antennas have equal magnitude at y_{eq}.

of the propagation paths in the antenna coordinate system $x''y''z''$ lead to significant variations of the antenna gain and thus significant variations of $c_s(y)$.
The beam of TX 0° is slightly better aligned to the RX than TX 15° in the first part of the track when moving towards positive y, which leads to a difference in power between antennas of the LOS components. The LOS component powers are equally 20 dB above the noise floor when the TX is at $y = y_{\text{equ}} = -24.3\,\text{m}$, where both antennas are aligned equally to the RX. The LOS component power of TX 0° decreases for $y > y_{\text{equ}}$ due to beam misalignment, whereas it is higher for TX 15°.
In the first part of the track ($y < -28\,\text{m}$), the magnitudes of the other MPCs, $|c_2(y)|$ and $|c_3(y)|$, are smaller for TX 15° than for TX 0° due to spatial filtering according to the beam pattern in fig. 4.2. In the remaining part of the track, the sidelobes of the beam pattern dominate $|c_2(y)|$ and $|c_3(y)|$ and cause high variability.
For the following analysis of the LOS delay tap of the wireless channel $h(y, \tau_{\text{LOS}})$ at a center frequency $f_c = 60\,\text{GHz}$, the channel bandwidth is 100 MHz with delay resolution $\Delta\tau = 10\,\text{ns}$. The LOS delay relative to the delay resolution, i.e. $\frac{\tau_{\text{LOS}}(y)}{\Delta\tau}$, changes with y at a low rate and thus a deterministic model is appropriate. The path lengths relative to wavelength change with y at a high rate due to the short wavelengths at mm-wave frequencies. Due to uncertainty of a car's position in V2I scenarios higher than the wavelengths for mm-wave, a stochastic model is appropriate for the path lengths.
I model each realization of the LOS delay tap $h(y, \tau_{\text{LOS}})$ with a random initial path length offset for each path, drawn uniformly from the interval $[0, \lambda_c)$. The resulting LOS power $|h(y, \tau_{\text{LOS}})|^2$ in terms of SNR is shown in fig. 4.6 for two different realizations of the simulation scenario. The trend of the LOS power is equal for both realizations. However, the y-positions of fading holes are not equal due to different initial path length offsets between realizations.

4.4.2 Variability Results

The variability of the LOS delay tap SNR is expressed in terms of the coefficient of variation (CV) introduced in eq. (4.1). The expectation in eq. (4.1) is taken over an ensemble of 50 trials. Furthermore, samples within a spatial window of 2 m on the y-axis are included in the ensemble. Each trial introduces a random path length offset, uniform within $[0, \lambda_c)$, for $s = 2$ and $s = 3$ to create different realizations of interference patterns. Figure 4.7(top) shows the CV of $|h(y, \tau_{\text{LOS}})|^2$ for TX 0° and TX 15°. Furthermore, the CV for a TX, perfectly aligned to RX, and analytical CVs CV_{R} and CV_{TWDP}, cf. eq. (4.15) and eq. (4.14), for TX 0°, TX 15° are shown for comparison in fig. 4.7(top).
The CV for TX 0° is more severe than for TX 15° for the first part of the track. The CV is lower for TX 0° than for TX 15° only for a short y-span. The aligned TX in fig. 4.7(top) has lowest CV for almost the whole track. However, at larger distances around $y = -40\,\text{m}$, even the aligned TX has higher CV than TX 15°.
Next, I analyze the impact of neglecting the MPC due to a bounce on the car in the

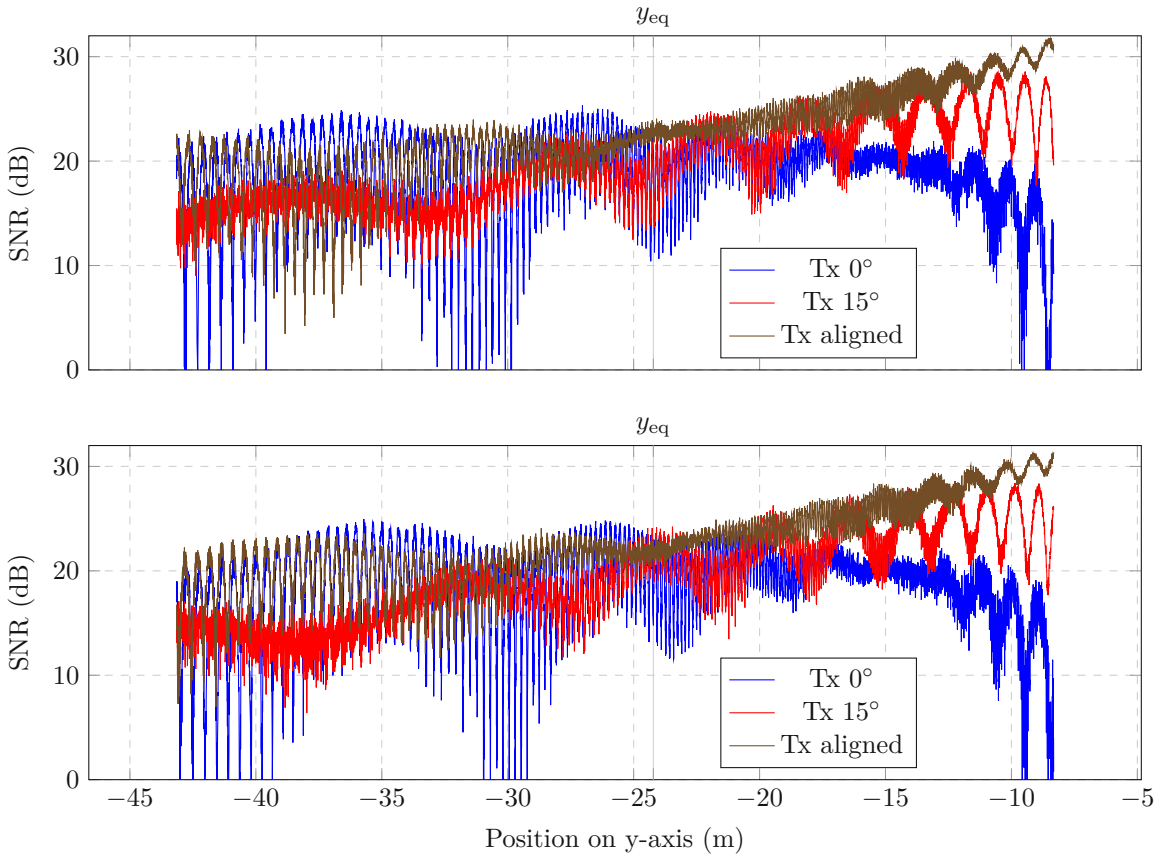

Figure 4.6: Instantaneous specular to diffuse power ratio. Equal gain for Tx 0° and 15° at y_{equ}.

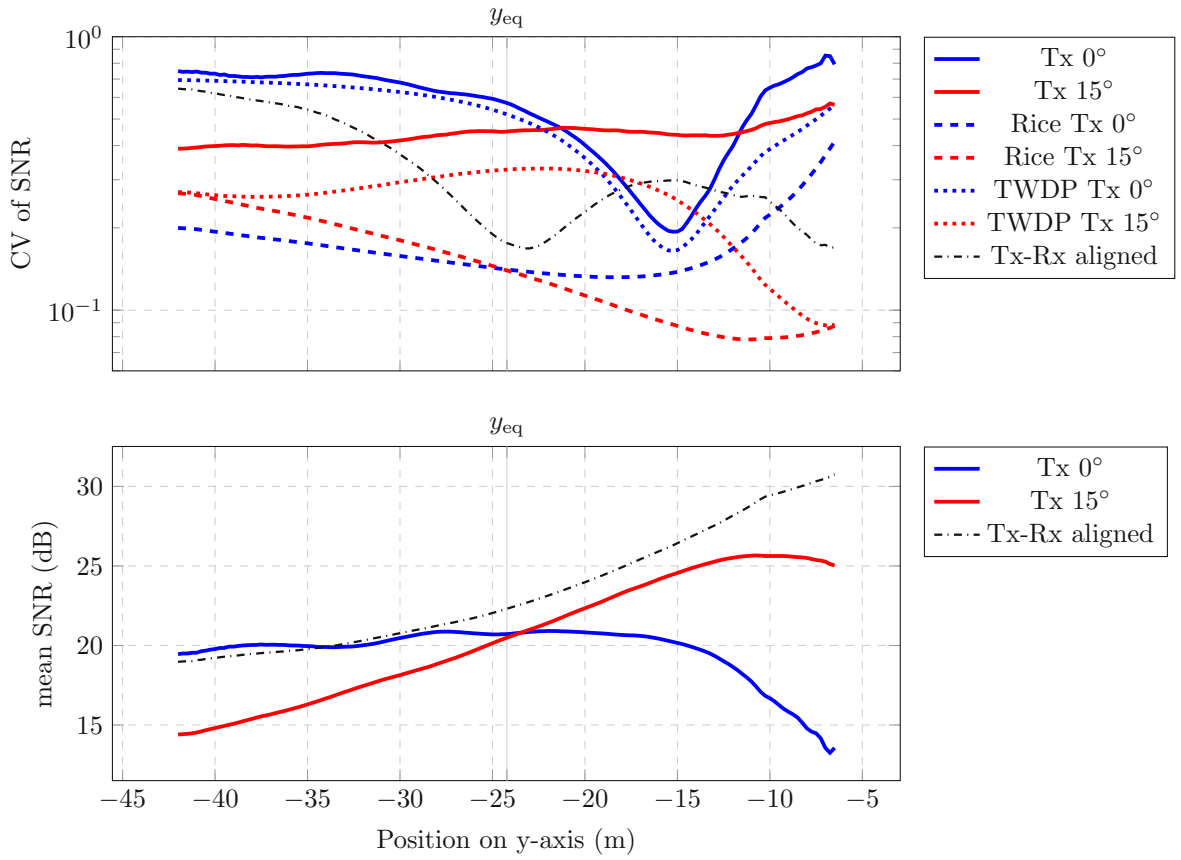

Figure 4.7: Variability of the receiver SNR for TX 0°, TX 15°, and a TX aligned to the RX. LOS components of both antennas have equal magnitude at y_{equ}. Top: Sample based CV and analytical CV_{R}, cf. eq. (4.15), and CV_{TWDP}, cf. eq. (4.14), for TX 0° and TX 15°. CV_{R} considers only the magnitude of the LOS component. CV_{TWDP} considers the magnitudes of the LOS component and a ground path. Bottom: Mean SNR.

evaluation of the CV in fig. 4.7(top). The analytical $\mathrm{CV}_{\mathrm{TWDP}}$, as defined in eq. (4.14), is based on TWDP fading involving the LOS and a MPC from ground reflection. Furthermore, the analytic CV_{R}, as defined in eq. (4.15), is based on Rician fading involving the LOS. It serves as a comparison in case no other MPCs is involved. The sample based CV is very close to the corresponding $\mathrm{CV}_{\mathrm{TWDP}}$ for TX 0°. There is a significant gap between the sample based CV and the corresponding $\mathrm{CV}_{\mathrm{TWDP}}$ for TX 15°. The CVs for both antennas deviate significantly from CV_{R}, where only the LOS was considered.
The mean SNR of $|h(y, \tau_{\mathrm{LOS}})|^2$ for TX 0°, TX 15°, and an aligned TX is shown in fig. 4.7(bottom). In the first part of the track ($y < y_{\mathrm{equ}}$), mean SNR is higher for TX 0° than for TX 15°. The situation reverses in the second part of the track ($y > y_{\mathrm{equ}}$). The aligned TX has highest mean SNR for almost the whole track.

4.4.3 CDF Fit of Simulation Data

The goal is to find a parametric distribution to infer an adequate small-scale fading model for the LOS delay tap power $|h(y, \tau_{\mathrm{LOS}})|^2$ as a random process. The distributions' characterizing parameter values and their trend may provide valuable information in channel modeling.
To this end, I fit parametric distributions to the empirical CDFs of samples from $|h(y, \tau_{\mathrm{LOS}})|^2$. It is often acceptable for measurements, to treat samples from a random process as ergodic within a short window of time or space. Therefore, the large trends in $|h(y, \tau_{\mathrm{LOS}})|^2$, cf. fig. 4.6, require a very small spatial window for a satisfactory result. However, the fading pattern of $|h(y, \tau_{\mathrm{LOS}})|^2$ reveals spatial fading with small and large spatial fading periods. On the one hand, an empirical CDF needs to encompass enough representative samples within the large spatial fading period for parameter estimation. On the other hand, magnitudes of the MPCs, cf. fig. 4.5, are varying too much within the large spatial fading period to be treated as constant.
The chosen simulation setup, as described in section 4.4.1, provides an ensemble of realizations. For measurements in a realistic vehicular environment, however, there is often only one realization available.
Therefore, the simplified three-wave with diffuse power model in section 4.1.4 enables fitting of CDFs by employing the TWDP fading model within a y-span smaller than the large spatial fading periods.
The estimated TWDP parameter $\hat{K}_{\mathrm{TWDP}}$ captures the ratio of specular power to diffuse power. The specular power is $\tilde{V}_1^2 + V_2^2$, where $\tilde{V}_1$ is the magnitude of two specular components in approximately constant superposition and V_2 is the magnitude of a third specular component. I choose y-spans around local peaks of the LOS delay tap power in fig. 4.6.
Figure 4.8 shows the specular to diffuse components parameter K_{S3WDP} for known path magnitudes $\tilde{V}_1$ and V_2 based on fig. 4.5. Furthermore, the mean $\hat{K}_{\mathrm{TWDP}}$ from TWDP CDF fits, and the mean $\hat{K}_{\mathrm{R}}$ from Rice CDF fits are shown. Data points where the Kolmogorov-Smirnov test rejects the candidate distribution are not shown. The mean

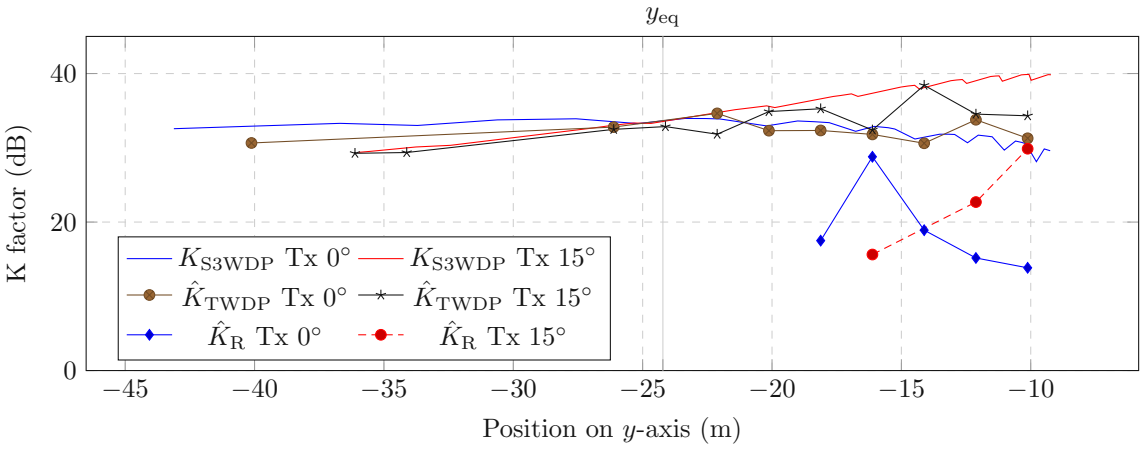

Figure 4.8: Specular to diffuse components K_{S3WDP} for known path magnitudes $\tilde{V}_1$ and V_2, mean $\hat{K}_{\text{TWDP}}$ from TWDP CDF fits, and mean $\hat{K}_{\text{R}}$ from Rice CDF fits. The empirical CDFs contain only samples within a small spatial window around peaks of the LOS power. The mean for $\hat{K}_{\text{TWDP}}$ and $\hat{K}_{\text{R}}$ is taken across 5 realizations.

for $\hat{K}_{\text{TWDP}}$ and $\hat{K}_{\text{R}}$ is taken across 5 realizations. The estimated parameter $\hat{K}_{\text{TWDP}}$ of the fitted TWDP CDF nicely follows the analytical K_{S3WDP} for both antennas. In contrast, the estimated parameter $\hat{K}_{\text{R}}$ of the Rice distribution fit shows large deviations from K_{S3WDP}. Moreover, the Rice distribution is rejected in more than two thirds of the track.

4.5 Measurement Campaign

I designed a measurement campaign in [8] to assess the impact of different tilt angles, of the employed antennas on a moving car, on the variability of the V2I mm-wave communications channel. The scenario of interest is a moving car approaching a street crossing in an urban street environment as shown in fig. 4.1. The car communicates in the mm-wave frequency band with an elevated infrastructure node at the traffic lights. The measurement campaign consists of several runs of the approaching maneuver shown in fig. 4.9, conducted on Sept. 25, 2018, near *Gußhausstraße 25* during normal business hours with random traffic and some parked vehicles present. The TX position trajectories of this campaign are derived from video data as described in [125].
I've not detected any interferences from other users in the occupied frequency band during the measurement. The car is equipped with two TXs with directive horn antennas mounted on the car's roof. The orientation of both antennas is in driving direction, such that most of the power is radiated towards the street crossing. One horn emits a beam horizontally, named TX 0°. The second horn emits a beam with a 15° uptilt, named

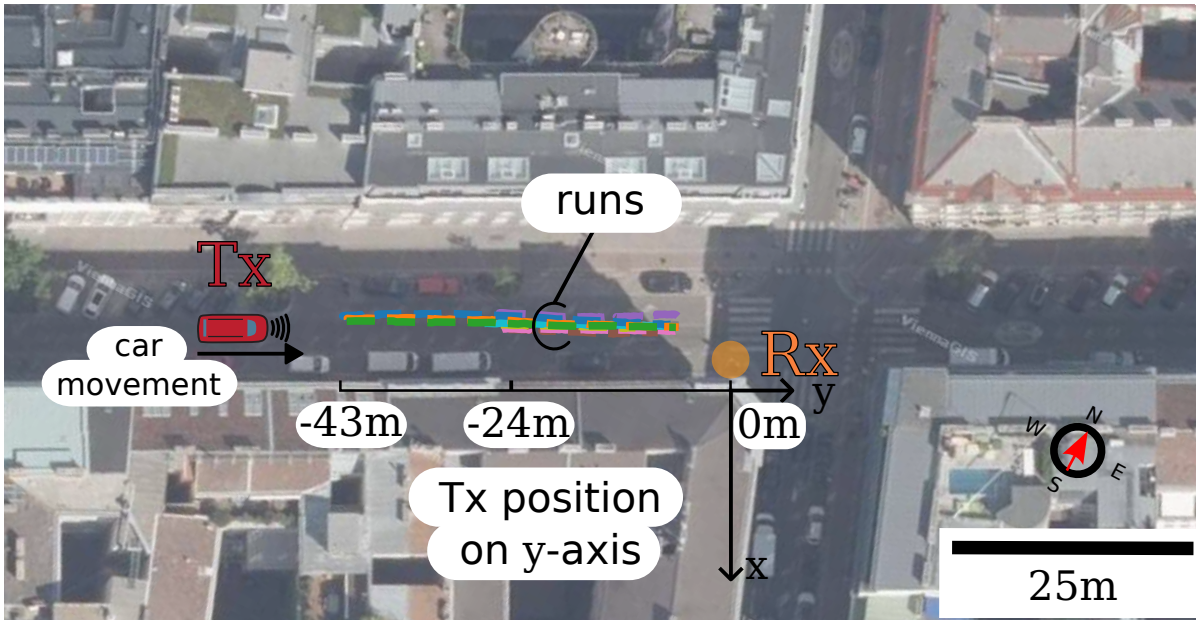

Figure 4.9: Orthophoto map of transmitter (TX) trajectories of several measurement runs, and receiver (RX) position during measurement campaign [8]. The cars on the background map do not correspond to cars present during the measurement. Map background: Stadt Wien – https://data.wien.gv.at.

TX 15°. Both horn antennas have a gain of 20 dBi. The 60 GHz free space path loss calculates to 100 dB at the maximum distance of interest of the scenario. The RX employs an omnidirectional $\lambda/4$ monopole antenna with an antenna gain of approximately -4 dBi including cable losses.
A custom built dual TX channel sounder measures the wireless channel at a center frequency $f_c = 60.15$ GHz with bandwidth $B = 100$ MHz. The channel sounder operates in FDM mode as described in section 3.3.1, with number of tones per antenna $N_\tau = 21$, tone spacing $\Delta f = 4.76$ MHz, and maximum alias free delay $\tau_{\max} = 210$ ns.
The parameters of the utilized channel sounder are summarized in table 4.1. The multitone sounding sequence has a period of 840 ns. Multiple periods are required to achieve an averaging gain G_{avg}, see section 3.3.3, and thereby improve the SNR of one TVTF snapshot.

Measurement Setup

Figure 4.10 shows a schematic of the measurement setup with the employed channel sounder. An arbitrary waveform generator[2] provides multitone signals (I_1/Q_2 and I_2/Q_2) to two TX IQ upconverter modules[3] with directly connected TX antennas. The RX is a

[2] *Keysight M8195A*
[3] custom built modules employing an *Analog Devices HMC6000* chipset

Table 4.1: Channel sounder parameters [8]

Parameter	Value
center frequency	$f_c = 60.15\,\text{GHz}$
tone spacing	$\Delta f = 4.76\,\text{MHz}$
number of tones	$N_\tau = 21$
number of TX antennas	2
tone spacing between antennas	$\Delta f_{\text{Ant}} = 1.19\,\text{MHz}$
bandwidth	$B = 100\,\text{MHz}$
maximum alias free delay	$\tau_{\max} = 210\,\text{ns}$
transmit antennas	20 dBi conical horn
receive antenna	$\lambda/4$ monopole
recording time	$T_{\text{rec}} = 3.6\,\text{s}$

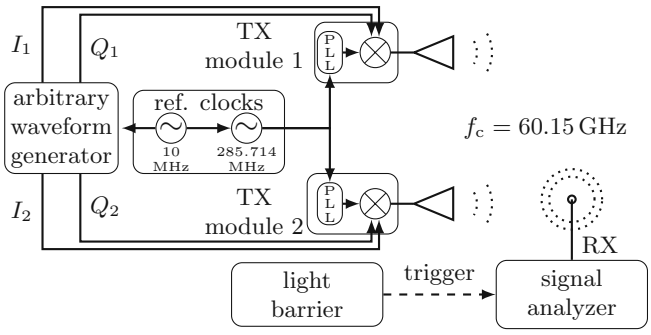

Figure 4.10: Measurement setup for the measurement campaign in [8].

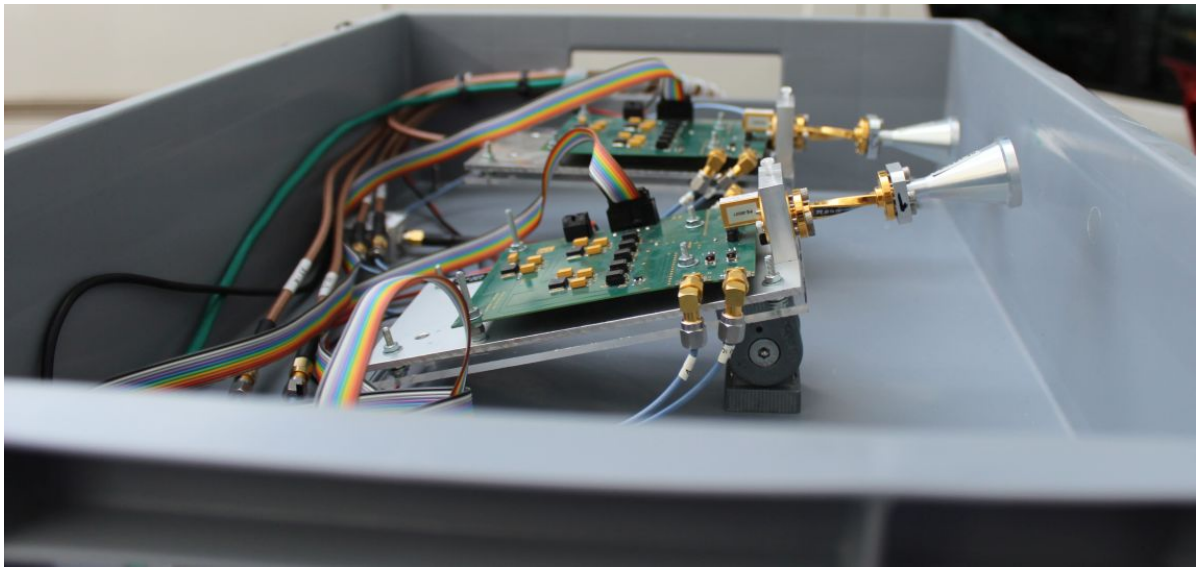

Figure 4.11: Transmitter (TX) platform with TXs modules and directly attached horn antennas.

signal analyzer[4] with an antenna connected through a cable. A oven controlled oscillator provides reference clocks[5] for both TXs and the signal analyzer employs its internal oven controlled oscillator. A light barrier triggers the recording of a measurement run and provides an indicator for the synchronization of a video recording [125].
Figure 4.11 shows the TX modules mounted on a TX platform on the roof of the car. A case protects the TXs from headwind and potential wind gusts. I neglect the influence of the case on the resulting antenna pattern.

4.5.1 Preprocessing

Some preprocessing is necessary to retrieve an estimate of the LOS delay tap $\hat{h}_{\mathrm{LOS}}[k]$ from the received signal $r(t)$ in eq. (3.3) with sufficient SNR.
First, I estimate the TVTF $\hat{H}[k,l]$ with a Hann window as receive filter $\gamma(t)$, which spans 10 repetitions of the sounding sequence. Second, I correct the center frequency offset (CFO). Third, I track delay and Doppler estimates from a LOS tracker with a Kalman filter. Fourth, I transform $\hat{H}[k,l]$ into a CIR employing the inverse DFT and zero-padding for an interpolated delay domain with delay l''. Fifth, I correct for the Doppler shift of the LOS component to enable further coherent averaging with sufficient averaging gain. This procedure of tracking the phase of this deterministic phase due to motion is known as phase synchronization [126] and important in evaluating the channel as composite deterministic and random channel.

[4] *Rohde & Schwarz FSW67*
[5] *Rohde & Schwarz SMA 100 A*

The result is an average CIR $\hat{h}[k, l'']$ and the center delay of the LOS delay tap $\hat{h}_{\mathrm{LOS}}[k] = \hat{h}[k, l''_{\mathrm{LOS}}[k]]$ is aligned with the LOS delay determined with the LOS tracker. A LOS delay adjusted channel estimate is comparable to a receiver, which has successfully synchronized to the LOS component in time delay and adjusts for changes in the delay of the LOS component.

Coherent Averaging. The choice of the averaging time window determines the time resolution of the average channel. The maximum window length is limited by phase drift of the measurement system, e.g. oscillator drift, such that coherency is lost.
To this end, I measure a single tone over a duration of one second before each run to estimate the mean CFO between the TX at standstill and the RX. After CFO correction of the tone, the phases of the corresponding complex phasor drift up to 90° within 0.9 ms. Therefore, I assume a negligible phase drift for coherent averaging with $T_{\mathrm{R}} \ll 0.9\,\mathrm{ms}$.
Furthermore, the dynamic range of the measurement system is not only limited by receiver noise, but also interference from limited cross-channel isolation I_{ij} between TXs of channel i and j, cf. eq. (3.14). Therefore, the effective dynamic range is instantaneous and depends on the instantaneous channel power ratios $p_i(t)/p_j(t)$ between TX-RX pairs. If the ratio $p_i(t)/p_j(t) \geq I_{ij}$, with $i \neq j$, then $p_j(t)$ has severe measurement errors. To this end, I limit the averaging length to an effective channel snapshot period $T_{\mathrm{R}} = 176.4\,\mu\mathrm{s}$, such that the inferring power is always at least 3 dB lower than the estimated noise floor and thus negligible.

4.5.2 Variability Results

I analyze the variability of the LOS delay tap SNR $|\hat{h}_{\mathrm{LOS}}[y]|^2$ through the CV in eq. (4.1). The video recording enables the mapping from time index k to the position of the TXon y-axis. The expectation in eq. (4.1) is replaced by the sample average of all the instantaneous SNR samples across all measurement runs within a spatial window. The spatial window has a RMS-width across measurement runs of 0.3 m in x-direction and I choose a 2 m width in y-direction. Figure 4.12 shows the CV of the instantaneous SNR and mean SNR of the LOS delay tap for different TX antennas with a moving spatial window along the y-axis. The CV is mostly higher for the TX antenna with horizontal beam compared to the uptilt TX antenna. When both antennas are combined at the RX, the sum of the instantaneous SNRs of both TXs has lower CV most of the time, with greatest reduction near $y = -20\,\mathrm{m}$. For $y > -10\,\mathrm{m}$, beam alignment between RX and each TX is very poor according to the geometry. There the low mean SNR leads to unreliable values of CV.

4.5.3 Small-scale Fading Evaluation

Small-scale fading effects of the channel occur on the order of half a wavelength [127]. Therefore, the spatial sample rate of the coherently averaged channel, while the TX

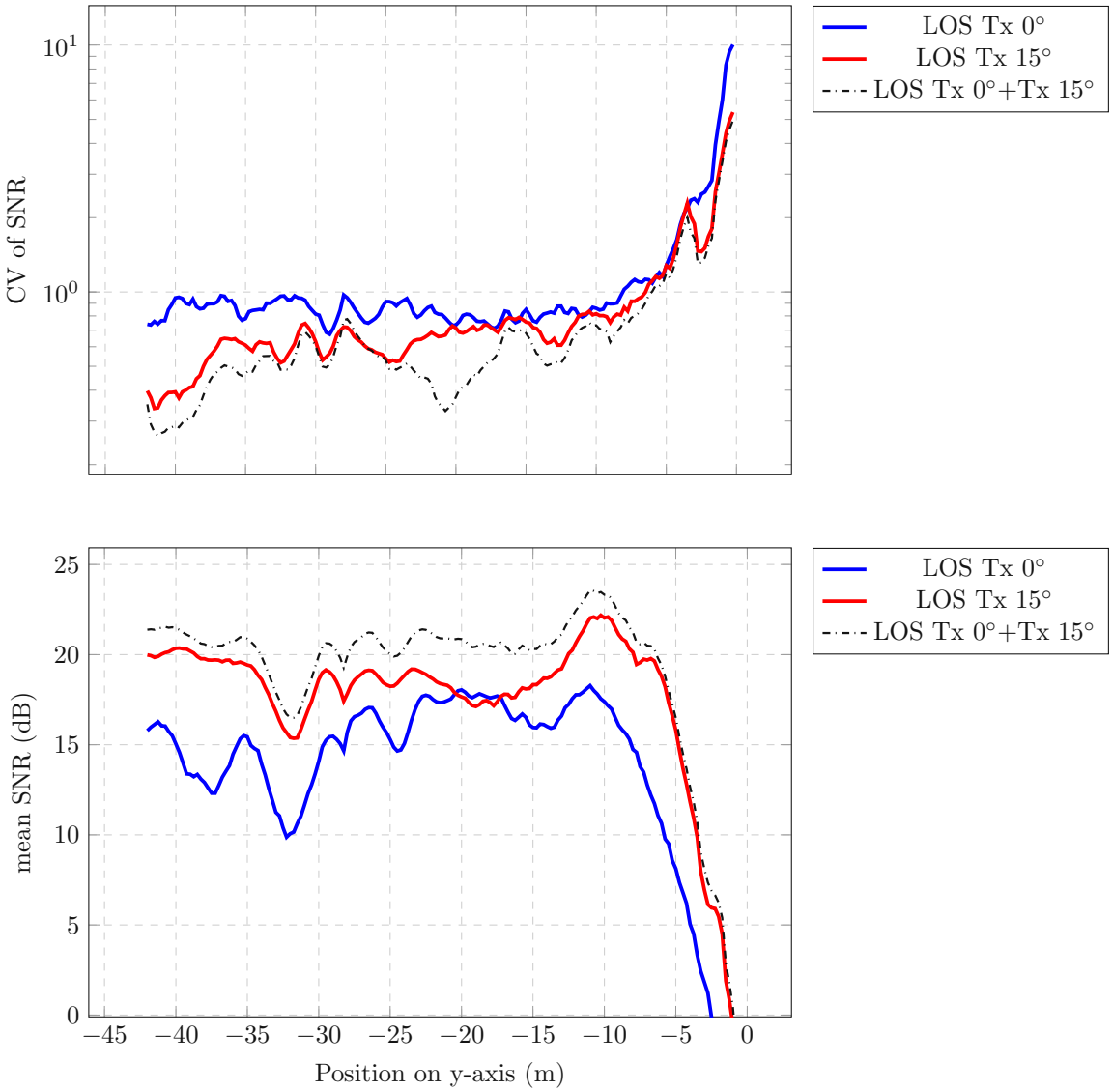

Figure 4.12: Variability of the instantaneous LOS delay tap SNR for each TX and sum SNR depending on the position on y-axis. Top: Coefficient of variation (CV) eq. (4.1) of instantaneous LOS delay tap SNR. Bottom: Mean LOS SNR.

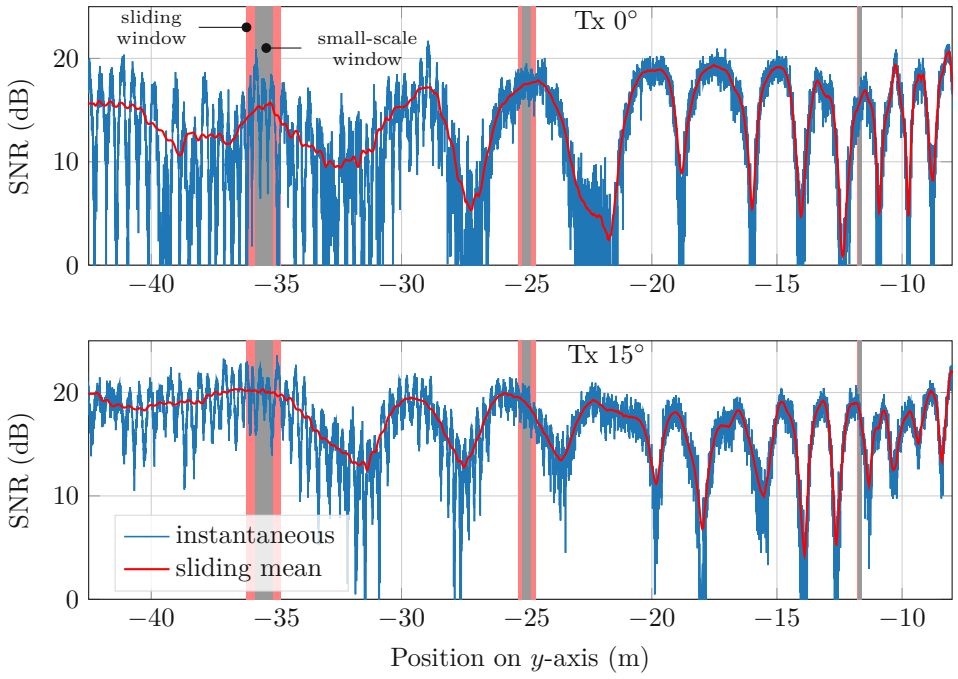

Figure 4.13: Instantaneous and mean SNR of LOS delay tap dependent on the TX y-position for a single measurement. The sliding window for the mean SNR is double the width of the window for small-scale fading investigation. Top: Tx 0°. Bottom: Tx 15°.

moves towards the RX, must be sufficiently high to evaluate small-scale fading. The fading process is assumed stationary within a small-scale window of spatial length L_{SS}. Large-scale fading occurs over larger scales. It is common to assume a multiplicative model and to separate the two effects by a local power average of spatial length $L_{AV} > L_{SS}$ to remove the small-scale fading effects. However, a classification of fading into small-scale or large-scale may be subjective, even for fading according a two-ray model [118]. In the presence of two-ray fading, the small-scale window should be larger than or equal to the spatial fading period $d_{\mathrm{TR}} = \frac{\lambda d^2}{2 h_{\mathrm{Tx}} h_{\mathrm{Rx}}}$ of a two-ray fading model [119, eq. (8)], with ground distance d, TX height h_{Tx}, and RX height h_{Rx}, to collect sufficient samples during a single run to be able to estimate parameters of an underlying distribution, i.e. $L_{AV} > L_{SS} \geq d_{\mathrm{TR}}$. The two-ray model considers a LOS path and a ground reflected path. I choose $L_{SS} = 2d_{\mathrm{TR}}$ for the investigation of small-scale fading, with a minimum of 30λ for L_{SS}.

Figure 4.13 shows an example of the instantaneous and sliding mean SNR of the LOS delay tap for a single measurement run and both antennas, Tx 0° and Tx 15°. The TX moves towards the elevated RX and simultaneously approaches the street crossing. The length L_{AV} of the sliding window for the sliding mean SNR is adapted to the double the width of the considered small-scale window L_{SS} to cover at least the required d_{TR}.

The sliding mean SNR shows severe fading holes with a spatial fading period larger than L_{AV} and significantly larger than d_{TR} for both antennas.
Even though the effects of small-scale fading due to a ground reflection should be removed in the mean SNR, deep fading holes remain visible. I suspect that there is at least a third strong path present during the measurement. To average all small-scale fading effects, this would lead to an increase of the small-scale window beyond a spatial region where the channel statistics can be considered constant [128]. Therefore, I apply the simplified three-wave with diffuse power model in section 4.1.4 to enable fitting of CDFs by employing the TWDP fading model within a y-span of L_{SS} which is smaller than the large spatial fading periods.

4.5.4 Measurement CDF Results

First, I choose y-spans around local peaks in SNR of the LOS delay tap, e.g. in fig. 4.13. Second, I partition the samples of the LOS delay tap of the measured channel randomly into two groups with 60% for parameter estimation and 40% for goodness-of-fit testing to ensure the validity of statistical tests. Third, I fit parametric CDFs to an empirical CDF from the first group of samples. The set of parametric CDFs include the CDF of TWDP fading, the Rice distribution, and the Rayleigh distribution.
Forth, I employ the Kolmogorov-Smirnov test, cf. section 4.2.1, as a goodness-of-fit test between the candidate CDFs with estimated parameters from samples of the first group, and the empirical CDF from samples of the second group. I accept the hypothesis $\mathcal{H}_0$, i.e. the test samples are from an estimated candidate CDF, if the p-value is above the significance level $\alpha = 0.05$.
Figure 4.14 shows CDFs of TWDP fading, Rice distribution, and Rayleigh distribution fitted to the empirical CDF with samples within a window L_{SS} centered at $y = -9.2\,\mathrm{m}$ for TX 0° and $y = -43\,\mathrm{m}$ for TX 15°. The Rayleigh distribution provides no good fit in this example, as expected from a LOS scenario. The TWDP fading model provides a better fit than the Rice distribution. For the examples shown fig. 4.14, the Kolmogorov-Smirnov test accepts $\mathcal{H}_0$ for TWDP CDFs and rejects $\mathcal{H}_0$ for the Rice distribution and the Rayleigh distribution.
Figure 4.15(bottom) shows the p-values, cf. section 4.2.1, for TX 0° and TX 15° depending on the position of the TX on y-axis. The rate of accepting $\mathcal{H}_0$ within 5 m on the y-axis is shown in fig. 4.15(top). For positions around $y = -40\,\mathrm{m}$, TWDP CDFs are accepted most often among the test distributions for both antennas. The Rice distribution is accepted at a higher rate for $y \geq -35\,\mathrm{m}$.
Table 4.2 gives an overview of the total number of accepted $\mathcal{H}_0$. For TX 0°, $\mathcal{H}_0$ is accepted more often for TWDP than for Rician fading. For TX 15°, $\mathcal{H}_0$ is accepted nearly equally often for TWDP and for Rician fading. In this scenario and for both antennas, $\mathcal{H}_0$ was almost never accepted for Rayleigh fading.
The estimated parameters of the distributions for Rician and TWDP fading are varying along the driving trajectory. Figure 4.16(a) shows the estimated Rician K-factor $\hat{K}_{\mathrm{R}}$ and

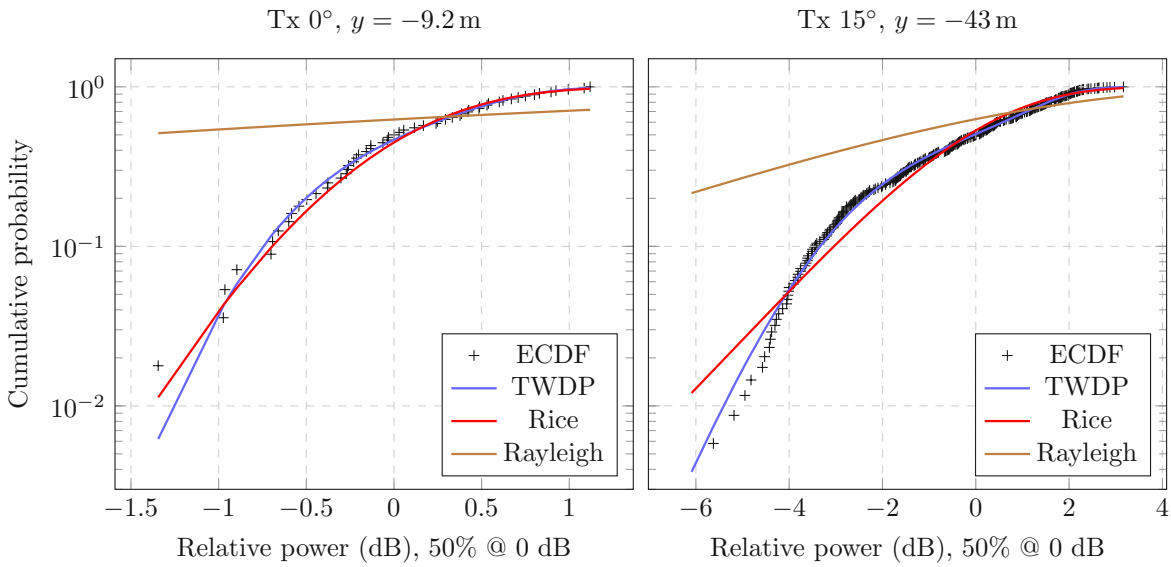

Figure 4.14: Results for cumulative distribution functions (CDFs) of TWDP fading, Rice distribution, and Rayleigh distribution fitted to empirical CDFs with samples from measurement data.

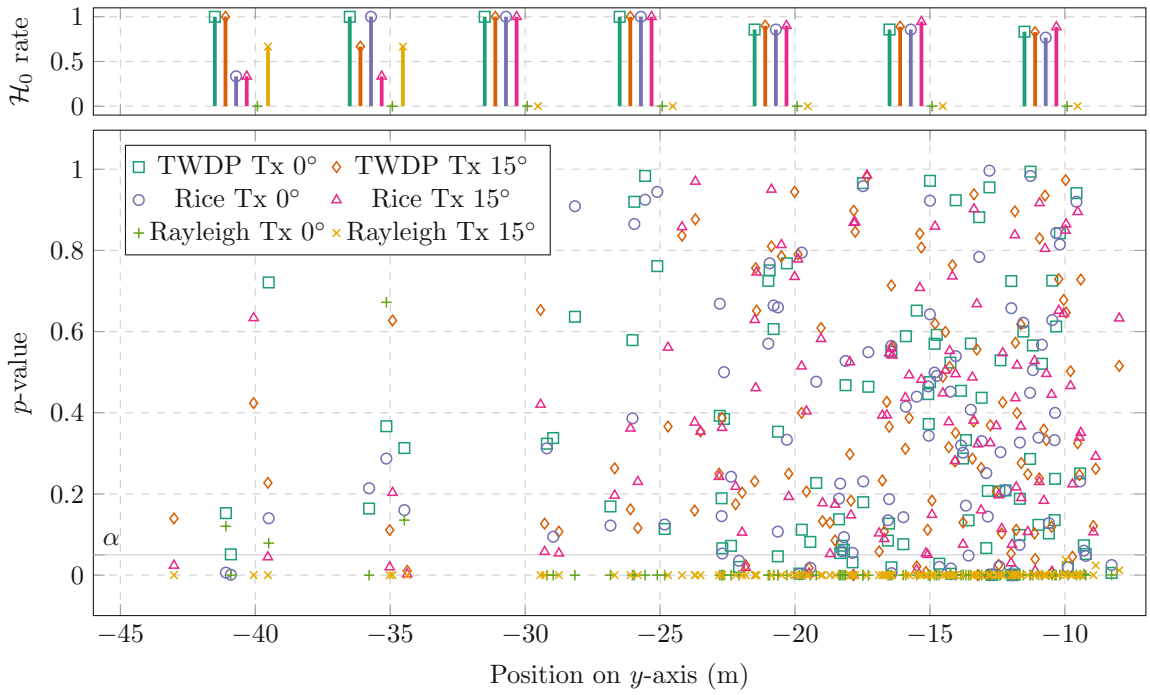

Figure 4.15: Kolmogorov-Smirnov test $\mathcal{H}_0$ acceptance rate within 5 m (top). p-values for estimated candidate CDFs of two-wave with diffuse power (TWDP) fading, Rice distribution, or Rayleigh distribution (bottom).

	TWDP	Rice	Rayleigh	Total
TX 0°	82	78	4	82
TX 15°	96	97	0	109

Table 4.2: Accepted H_0 for LOS tap

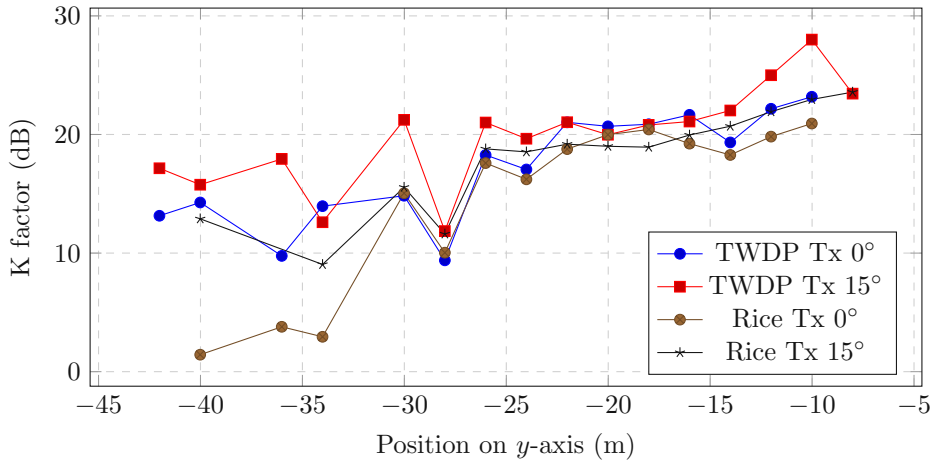

(a) K-factor

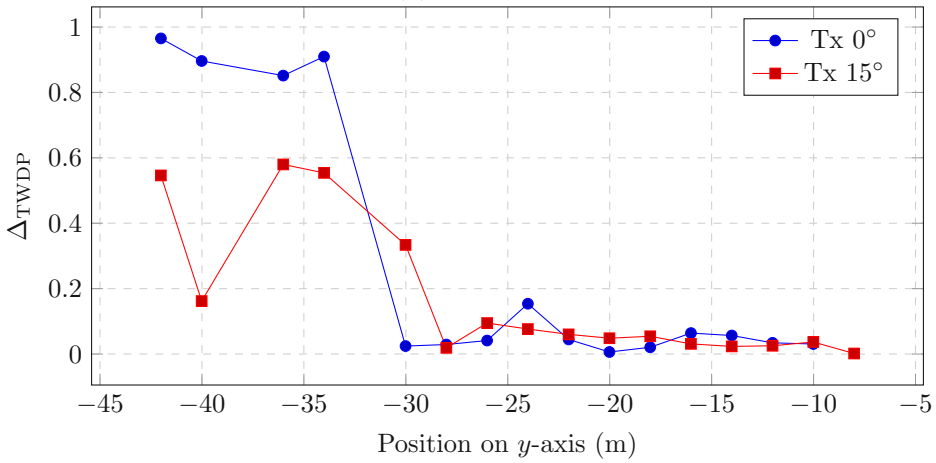

(b) Delta

Figure 4.16: 2 m mean along y-axis of fitting parameter results for K factor (a) and Δ_{TWDP} for TWDP only(b). Only results with accepted $\mathcal{H}_0$ are considered.

$\hat{K}_{\mathrm{TWDP}}$ for TWDP fading. The K-factors follow a positive trend as the TX approaches the RX. Furthermore, $\hat{K}_{\mathrm{R}}$ and $\hat{K}_{\mathrm{TWDP}}$ are higher for TX 15° than for TX 0°. $\hat{K}_{\mathrm{TWDP}}$ is almost always higher than $\hat{K}_{\mathrm{R}}$ for both antennas. $\hat{K}_{\mathrm{R}}$ is significantly lower than $\hat{K}_{\mathrm{TWDP}}$ for TX 0° in the y-span $-40 \leq y < -30$, where also the rate of accepting $\mathcal{H}_0$ for Rician fading is low, cf. fig. 4.15.
Figure 4.16(b) shows the estimated $\hat{\Delta}_{\mathrm{TWDP}}$ parameters of the fitted TWDP CDFs. For $y \leq -30$, $\hat{\Delta}_{\mathrm{TWDP}}$ is significantly higher than zero for both antennas and higher for TX 0° than for TX 15°. A high Δ_{TWDP} indicates similar magnitudes of the two dominant specular components in the TWDP model. $\hat{\Delta}_{\mathrm{TWDP}}$ is low for $y > -30$, where the rate of accepting $\mathcal{H}_0$ for Rician fading is high, cf. fig. 4.15.
At positions with high $\hat{\Delta}_{\mathrm{TWDP}}$, the TWDP fading model is required, because the Rician model is not adequate.

4.6 Discussion

In this chapter, I've employed the coefficient of variation (CV) as a moment-based metric for the variability of the channel in a V2I scenario due to its simplicity and the comparability with analytic CV from well-known fading distributions. It is common in literature to separate large-scale fading effects from small-scale fading effects of measured wireless channels by a multiplicative model where the average channel power within a small window is the large-scale part and fluctuations about this average are small-scale fading effects. However, this approach is troublesome when large periods are present in the channel's fading pattern due to the following two aspects. First, the averaging window for the channel power needs to encompass the large spatial fading period where the magnitudes of dominant specular components are hardly constant. Second, large-scale and small-scale fading are not multiplicative for a small averaging windows. I've introduced the simplified three-wave with diffuse power model, which helps to fit a parametric distribution to the empirical CDFs from samples of three interfering dominant specular components with a specific phase relationship.
Power from diffuse MPC is likely influenced by spatial filtering using directive beams. Therefore, the dynamic of the diffuse MPC power needs to be considered for more advanced simulations.

5 Sparsity in Delay-Doppler Domain

Preliminary results of this research have been published in [8]:

H. Groll, E. Zöchmann, S. Pratschner, *et al.*, „Sparsity in the delay-Doppler domain for measured 60 GHz vehicle-to-infrastructure communication channels“, in *2019 IEEE International Conference on Communications Workshops (ICC Workshops)*, May 2019. DOI: 10.1109/iccw.2019.8756930

In chapter 4 I analyze the propagation paths with delay differences smaller than the temporal resolution, which leads to a fading magnitude of a single delay tap of a bandlimited. The full time delay domain, available from a bandlimited multicarrier system, enables an analysis of how the power is spread in delay through the wireless channel, which can reveal scatterers with significant power specific to the propagation environment. The framework of LTV channels in section 2.3 additionally enables an analysis of how the power is spread in the Doppler domain through the wireless channel, which provide further information about significant scatterers. For underspread LTV channels, the delay and Doppler domains can be treated independent in a two-dimensional description of the wireless channel. A sparse LTV channel model as in section 2.3.3 seems appropriate for V2I mm-wave wireless communications due to the use of directional beams for mm-wave wireless systems on either one or both sides of the channel. The presence of a LOS component is typical for the V2I scenario.

In this chapter, I extend the analysis of the V2I mm-wave measurement campaign in chapter 4 to the delay-Doppler domain and identify scatterers with significant powers. The LSF in section 5.1.1 serves as a tool for the analysis in the delay-Doppler domain. An estimator for the LSF is discussed in section 5.1.2. Reducing the LSF to only the time delay or the Doppler domain together with second order moments is considered in section 5.1.2. I analyze the V2I mm-wave measurement campaign of section 4.5 in section 5.2. I show identified scatterers with significant power in section 5.3.2. I investigate the impact of LOS delay tracking the measured channel in delay in section 5.3.3 and provide a discussion at the end of the chapter in section 5.4.

5.1 Method

5.1.1 Local Scattering Function

An underspread channel allows to treat the time domain finely sampled for delay estimation and coarsely sampled for Doppler estimation.
The LSF $\mathcal{C}(\tau, \nu; t, f)$ is a useful framework for statistical characterization of nonstationary random time-varying channels [129]. It provides a time t and frequency f dependent description in the delay τ and Doppler ν domain. Especially for investigating delay spread and Doppler spreads, the LSF is a good starting point. The LSF is a second-order statistic for LTV random channels, where $H(t, f)$ is a 2D nonstationary process. In general, the channel has a mixed deterministic and a random part, see section 2.3.2, where the original goal of the LSF is to describe the random part only. Nonetheless, LSF estimators $\hat{\mathcal{C}}(\tau, \nu; t, f)$, e.g. with a modulus squared 2D multitaper estimator [130], provide useful insights also in the mixed channel case.

5.1.2 Two-dimensional Multitaper Spectral Estimates

An estimate of the nonstationary spectral process of the channel, known as the LSF estimator $\hat{\mathcal{C}}[l', k'; t_b, f_l]$, is calculated with the following local multitaper spectral estimates [130], [131]

$$\hat{\mathcal{C}}[l', k'; t_b, f_l] = \sum_{i=0}^{I-1} \gamma_i \left| \hat{G}_i[l', k'; t_b, f_l] \right|^2, \tag{5.1}$$

with delay index l', Doppler index k', and I different local tapered spectral estimate $\hat{G}_i[l', k'; t_b, f_l]$ centered at time t_b and frequency f_l with weighting γ_i. Basically, the estimator applies the STFT on estimates of the TVTF $\hat{H}[k, l]$ in eq. (3.5) in two dimensions. Each tapered spectral estimate is

$$\hat{G}_i[l', k'; t_b, f_l] = \frac{1}{\sqrt{N_\nu N_\tau}} \sum_{l=0}^{N_\tau - 1} \sum_{k=0}^{N_\nu - 1} \hat{H}[t_b + k, f_l + l] D_i[k - k', l - l'] e^{j2\pi(\Delta\nu T_\mathrm{R} k k' - \Delta\tau \Delta f l l')}, \tag{5.2}$$

where k is the local time index, l is the frequency index, and $D_i[k, l]$ with $i = 1, \ldots, I$ are suitable 2D time-frequency windows, i.e. the data tapers. For simplicity, often $\gamma_i = 1/I$ and $D_i[k, l] = u_i[k] v_i[l]$ as separable time window $u_i[k]$ and frequency windows $v_i[l]$. In this thesis, the variation in center frequency f_l is omitted and therefore I employ the shorter notation $\hat{\mathcal{C}}[l', k'; t_b]$.
The choice of the windows is a trade-off between bias, variance, and resolution. Employing a single data taper reduces estimation bias due to leakage. However, it also reduces the effective sample size where the multitaper method counteracts the increase in estimation variance [131].

LSF Estimator Windowing Filter

The multitaper spectral estimator allows to use the number of available efficiently, whereas other single data tapers sacrifice part of available information.
Another issue is the nonstationarity of the process such that data tapers need to be localized. The multitaper spectral estimator employing discrete prolate spheroidal sequences is less localized with increasing taper number. Therefore, less than the recommended $\lceil 2NW \rceil - 1$ tapers for a stationary process should be used in the nonstationary case.

Reduced Description

Generally, the LSF describes the energy shift in the time-frequency domain locally at specific time and frequency. Delay and Doppler power profiles are derived from the LSF for a suitable local description of the energy shift in only time or frequency, respectively [129].
Likewise from the LSF estimator, estimates of the delay power profile at time t_b and frequency f_c is derived as

$$\hat{\mathcal{P}}_\tau[l'; t_b, f_c] = \frac{1}{N_\nu} \sum_{k'} \hat{\mathcal{C}}[l', k'; t_b, f_c], \tag{5.3}$$

and of the Doppler power profile of the channel centered at t_b and f_c is derived as

$$\hat{\mathcal{P}}_\nu[k'; t_b, f_c] = \frac{1}{N_\tau} \sum_{l'} \hat{\mathcal{C}}[l', k'; t_b, f_c]. \tag{5.4}$$

The first and the second central moments of the time-varying delay power profile eq. (5.3) are the time-varying mean delay and the time-varying RMS delay spread [11]. Correspondingly, the moments of the time-varying Doppler power profile eq. (5.4) are the time-varying mean Doppler and the time-varying RMS Doppler spread. Those moments are well-known wireless channel parameters.
An estimate of the mean LSF is calculated as

$$\bar{\mathcal{C}}[l', k'] = \frac{1}{N_b} \sum_{t_b \in \mathcal{T}_b} \hat{\mathcal{C}}[l', k'; t_b, f_c], \tag{5.5}$$

where N_b is the number of different time blocks t_b in a region of interest $\mathcal{T}_b$, and a single frequency block at f_c is assumed.

5.2 V2I Measurement Campaign

The investigated V2I mm-wave scenario is again the measurement campaign introduced in previous work [8] and in section 4.5 of chapter 4. The TX car moves along the street

towards the street crossing, where the RX is positioned at elevated position, as shown in figs. 4.1 and 4.9. At first, the measured channel is delay aligned at the light barrier positions $y = -43\,\mathrm{m}$ and $y = -24\,\mathrm{m}$, respectively, where the time-of-flight of the LOS path is known. Knowing the approximate velocity of the car $\mathrm{v}_{\mathrm{Tx}}(t)$, the LOS path has an effective velocity from the RX's point of view determined by $\mathrm{v}_{\mathrm{tx}}(t)$ and the enclosed angle between the direction of driving and the direction from TX to RX. By following the path analogy for MPCs, each path's delay rate of change $\frac{\partial \tau_s(t)}{\partial t}$ causes a Doppler shift as defined in eq. (2.8) (see also [132]). Let v_s now be the Doppler velocity of a path s, which is the effective velocity derived from a specific Doppler shift ν_s as

$$\mathrm{v}_s(t) = \frac{\partial \tau_s(t)}{\partial t} c_0 = -\nu_s(t)\lambda_{\mathrm{c}}. \tag{5.6}$$

The LOS path has $-1 \leq \frac{\mathrm{v}_s(t)}{\mathrm{v}_{\mathrm{Tx}}(t)} \leq 1$ if only the TX moves and the RX is static. Other paths can have larger $|\frac{\mathrm{v}_s(t)}{\mathrm{v}_{\mathrm{Tx}}(t)}|$ depending on the number of bounces and the velocity of interacting objects.

5.3 Results

5.3.1 RMS Spread

The investigated LOS scenario shows weak power contributions from MPCs resolvable in the delay-Doppler domain. This leads to negligible RMS delay spreads and RMS Doppler spreads if the received power within the LOS tap is high. For low power within the LOS tap, the sensitivity of the employed channel sounder is insufficient for evaluating RMS spreads.

5.3.2 Identified Scatterer Results

The wireless vehicular mm-wave channel could be modeled in a purely random or in a deterministic way. The accuracy of a vehicle's position increases with each technology evolution step through high-resolution street maps and precise *global navigation satellite systems*. Knowledge of the vehicle's position could enable a deterministic modeling of specular components. The benefits of knowing the deterministic part of the V2I mm-wave channel for designing future wireless systems have yet to be evaluated through measurement campaigns.
The measurement runs in section 5.2 allow to cross-reference the measured wireless channel with time-synchronized video data of the street crossing environment. From the available measurement runs, I describe the most noteworthy scatterers including the appearance of a delivery truck, a parked car, far scatters in driving direction, a van, and a passenger bus.

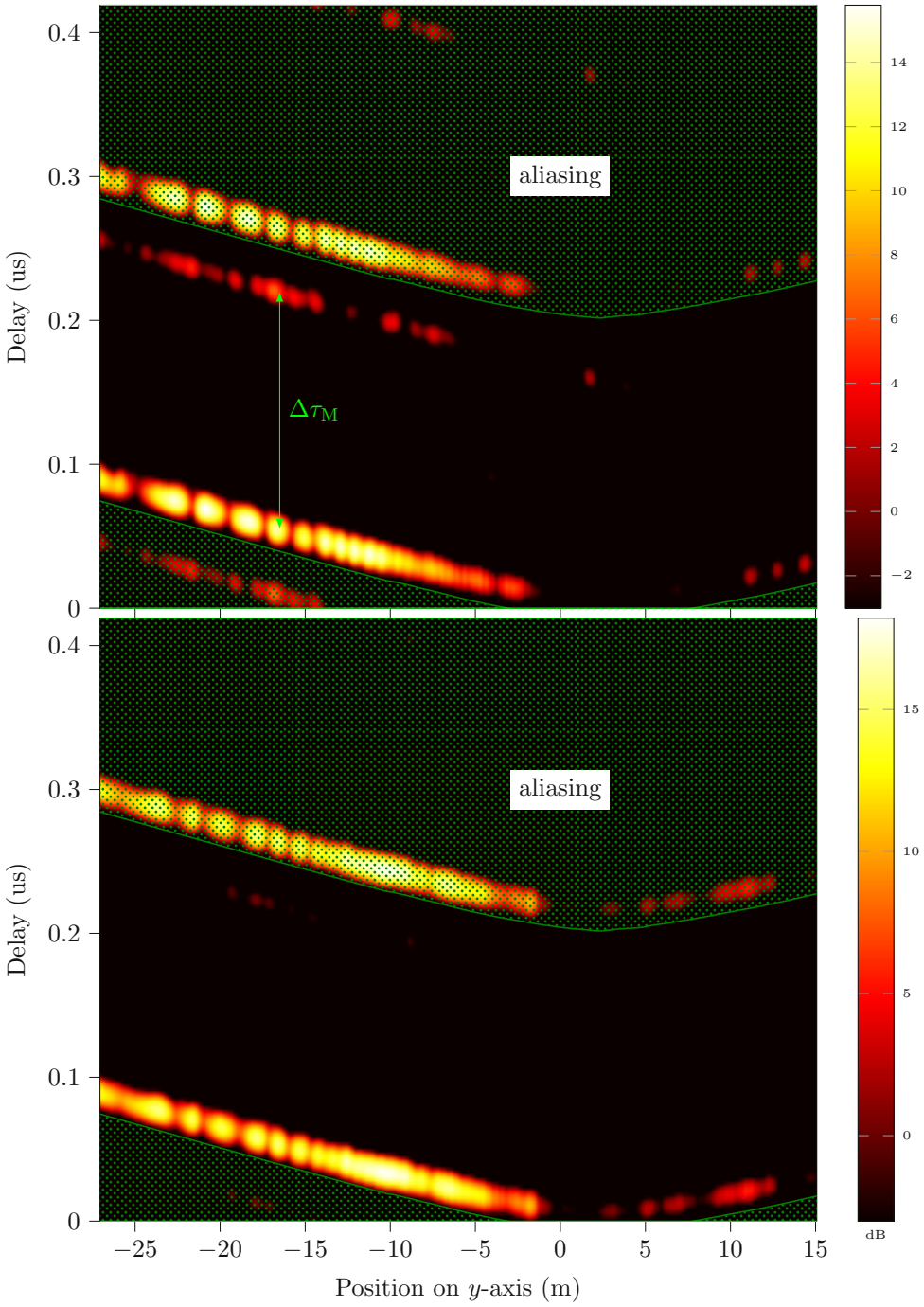

Figure 5.1: Estimated delay power profile of measurement run 6 for Tx 0° and Tx 15°. The tracked line of sight (LOS) component defines the region without aliasing. A MPC with significant power has excess delay $\Delta\tau_{\mathrm{M}}$.

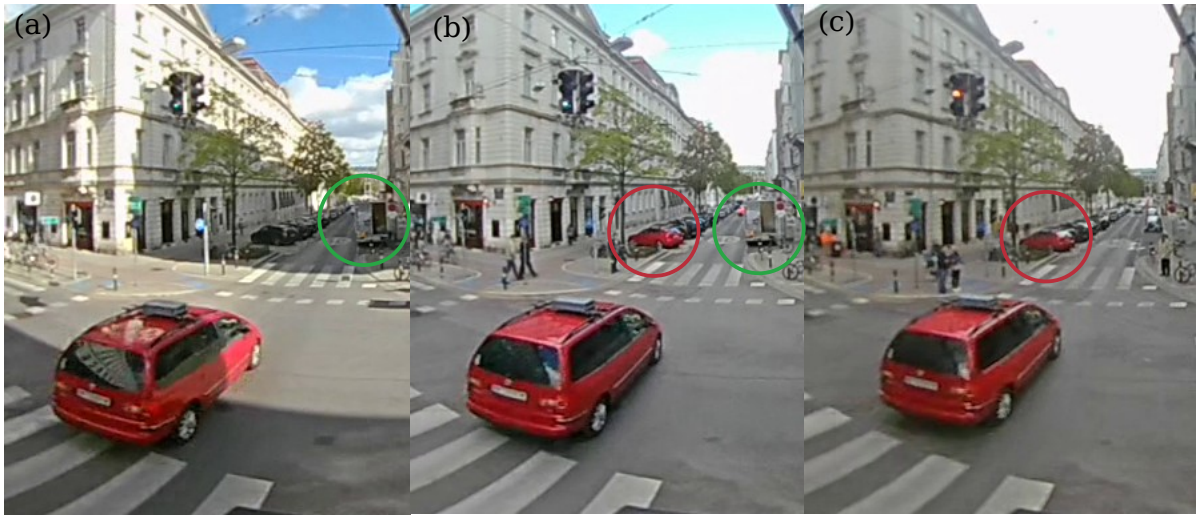

Figure 5.2: Photos of the moving TX car from three runs approximately at the receiver ground line (0 m). The green circles show the presence of a parked delivery truck in (a) and (b). The red circles show the presence of a parked car in (b) and (c).

Delivery truck. In measurement run 5 and 6 with the TX at 16.5 m from the RX line, one of the MPCs with significant power in the delay power profile of each antenna has an excess delay of $\Delta\tau_{\mathrm{M}} = 165\,\mathrm{ns}$. The power of the MPC is at least 5 dB higher for Tx 0° than for Tx 15° The delay of that MPC is in good agreement with the geometric positions of a delivery truck, which was parked next to Gusshausstraße 19, approximately at $y = 25\,\mathrm{m}$ after the RX as shown in fig. 5.2(a) and fig. 5.2(b). This particular MPC is not visible in other measurement runs, e.g. fig. 5.2(d), where the delivery truck was not present, which strengthens the attribution between video data and wireless channel data. A MPC corresponding to a parked car in (b) and (c), but not in (a) of fig. 5.2, could not be detected within the channel sounders dynamic range.

Far scatterers in driving direction. Scatterers far in front of the TX in driving direction could constitute MPCs of the wireless channel with significant power. Those MPCs are well within the broad main lobe of a antenna directed towards the RX due to the increased distance. The sensitivity of the employed channel sounder might be insufficient to distinguish them from noise in the delay domain. However, those MPCs with similar Doppler shifts can accumulate enough power to distinguish a peak in power in the Doppler power profile. An estimate of the Doppler power profile for both antennas is shown in fig. 5.3 normalized in terms of $\frac{\mathrm{v_s}(t)}{\mathrm{v_{Tx}}(t)}$. The LOS component (M1) in fig. 5.3 dominates for both antennas throughout the track of the TX. When the moving TX approaches the RX ground line at $y = 0\,\mathrm{m}$, the Doppler velocity of the LOS component approaches the point of inflection where the direction of driving is perpendicular to the

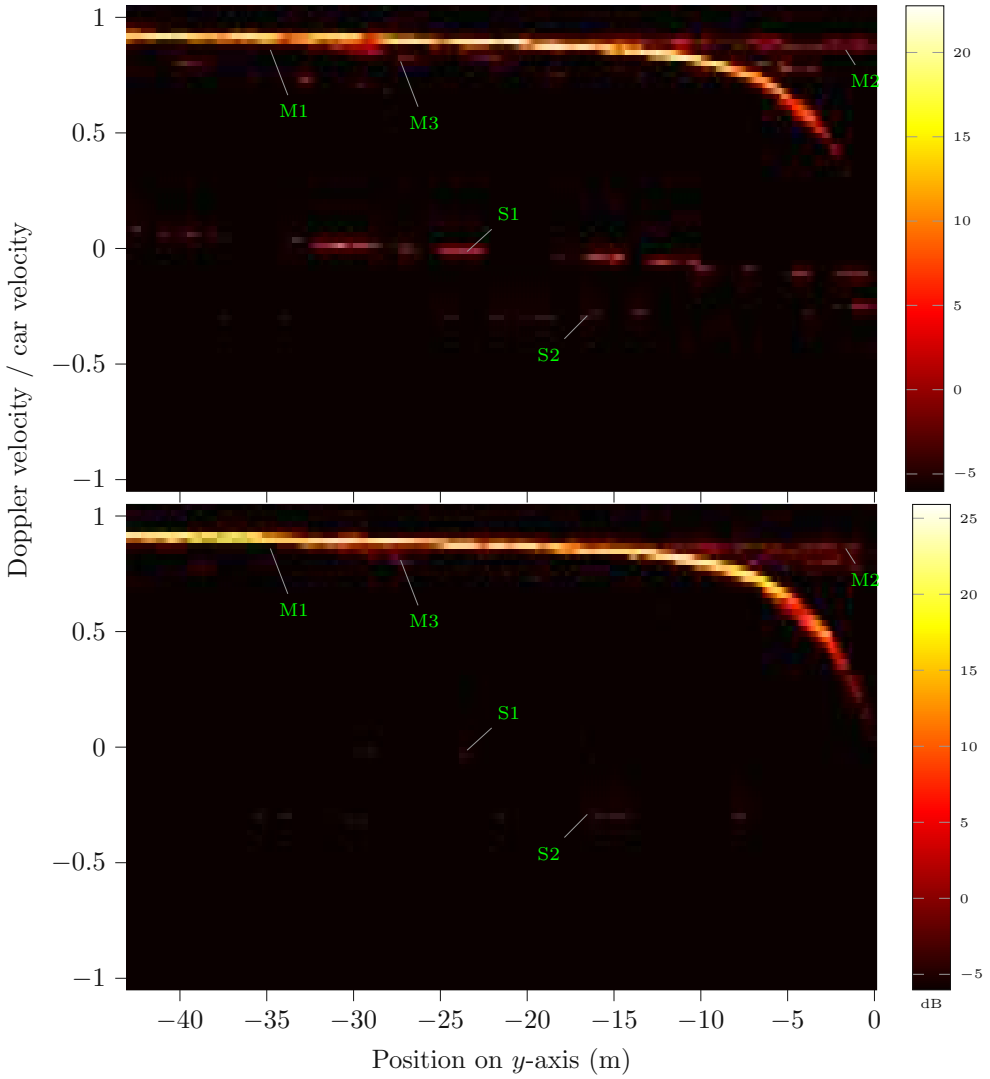

Figure 5.3: Estimate of the Doppler power profile of a single measurement run. M1: LOS component. M2: Far scatterers in driving direction. M3: MPCs due to TX passing scatterers. S1 and S2: Unknown MPC with significant power. Top: Tx 0°. Bottom: Tx 15°.

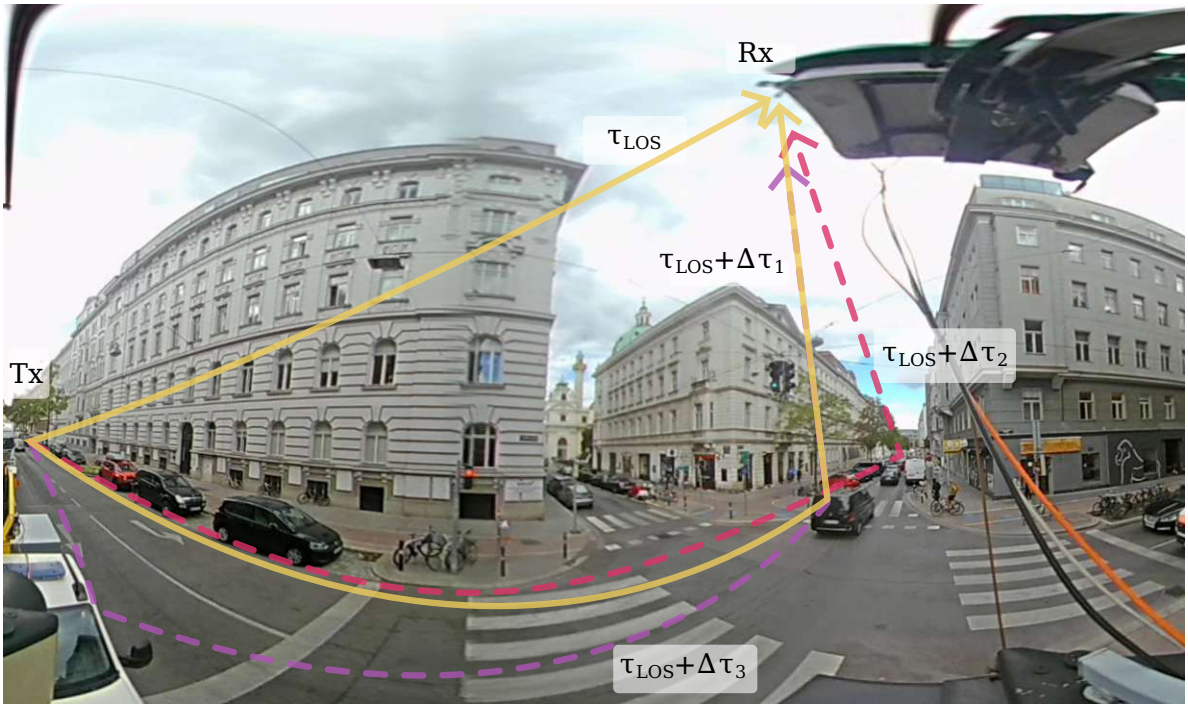

Figure 5.4: Photo of street scenario with moving TX at a large distance from receiver ground line. A moving black van is ahead of the receiver ground line. The LOS delay τ_{LOS} is 150 ns. A possible path with a single bounce at the rear side of a black van with excess delay $\Delta\tau_1 = 70\,\mathrm{ns}$. Further possible paths are, e.g. with a single bounce at the rear side of a moving truck with $\Delta\tau_2 = 430\,\mathrm{ns}$ or with multiple bounces via a parked truck with $\Delta\tau_3$.

direction from TX to RX. From $y = 5\,\mathrm{m}$ to $y = 0\,\mathrm{m}$, the power of the LOS drops below the noise floor, where the power transition takes longer for the uptilt antenna, possibly due to a better beam alignment between TX and RX. As the car velocity stays constant, MPCs with Doppler velocity close to the car velocity as shown in (M2) fig. 5.3 indicate scatterers ahead of the TX. The power of the MPCs (M2) is spread over the delay domain, thus the MPC might not be visible in the delay-Doppler domain. When the TX passes a scatterer causing a MPC with sufficient power, the Doppler velocity of the MPC transitions from close to car velocity towards negative Doppler shift, as shown in e.g. (M3) fig. 5.3. The effects (M1),(M2), and (M3) are characteristic to the static environment of this V2I measurement scenario and can be seen in all measurement runs.

Black van and passenger bus. MPCs with notable power are visible along the lines (S1) and (S2) in fig. 5.3. The line (S1) has negative Doppler shift and low power for both antennas. The line (S2) starts with a slightly positive Doppler shift, ends with a slightly negative Doppler shift, and has higher power for Tx 0° than for Tx 15°. In

measurement run of fig. 5.3, a black van had passed the RX when TX was at the light barrier as shown in fig. 5.4. A possible geometric interpretation of (S1) or (S2) could be the path starting from the TX with a single bounce at the rear side of a black van and ending at the RX. The excess delay of this path is $\Delta\tau_1 = 70\,\text{ns}$. Another path with excess delay $\Delta\tau_2 = 430\,\text{ns}$ could be due to a single bounce at the rear side of a moving truck or a parked truck leading to a path with excess delay $\Delta\tau_3 = 85\,\text{ns}$. However, a unique attribution of (S1) or (S2) to a physical object was not possible due to aliasing in the delay domain and low sensitivity of the employed channel sounder.
The power ratio of this MPC to the LOS component is slightly higher for the antenna with horizontal antenna compared to the uptilt antenna.
In another measurement run, fig. 5.5(a) and (b) show the mean delay-Doppler spectrogram over the full y-span to visualize the delay-Doppler regions of significant power. The TX moves from $y = -43.5\,\text{m}$ at the start until $y = -8\,\text{m}$ at the end of the measurement run. At the start, a moving passenger bus is visible in the video (not shown here), and positioned slightly further ahead compared to where the black van was in the previous run. A MPC corresponding to the passenger bus is clearly visible in the delay-Doppler domain for the horizontal beam, but less clear for the uptilt beam, possible due to spatial filtering. The MPC attributed to the passenger bus is subject to aliasing in the delay domain, as the MPC has a delay of 90 ns and it's geometrical path delay should be about $\tau_{\max}$ higher at 300 ns when the TX was at the light barrier at $y = -43.5\,\text{m}$.

5.3.3 LOS Delay Tracked Channel

The high availability of the MPC could be beneficial for diversity techniques. If the appearance and the position of large vehicles in the propagation environment is known, dominant specular components could be modeled with deterministic delay and Doppler. For a LOS delay tracked version of the time-varying channel with the previously mentioned passenger bus, the mean delay-Doppler spectrogram is shown in fig. 5.5(c) and fig. 5.5(d). A MPC corresponding to the passenger bus changes in delay-Doppler along a curve. The passenger bus delay-Doppler curve in (a) and (c) is estimated by finding the delay-Doppler bins of the spectrogram with largest power and negative Doppler velocities. A Kalman filter improves the estimate of the delay-Doppler curve.
Here, the passenger bus delay-Doppler curve crosses the LOS delay due to aliasing. This aliasing introduces interference at the LOS delay tap of the wireless channel as the wraparound delay of the MPC falls into the same delay bin as the LOS component, i.e. $\Delta\tau_w = \tau_{\text{LOS}} + n\tau_{\max}$ for $n \in \mathbb{N}$. However, the MPC due to the passenger bus remains resolvable in the delay-Doppler domain. When tracking of the MPC's delay is the objective, the ambiguity due to aliasing needs to be considered. At the end of the measurement run, the passenger bus moved further ahead such that the path delay should be at 375 ns. Consequently, the maximum excess delay $\tau_{\max}$ of a transmission system needs to take the long path delays into account. The mean power of the LOS delay-Doppler bin, $\bar{\mathcal{C}}[l'_{\text{LOS}}, k'_{\text{LOS}}; y]$, and the mean power of the passenger bus delay-

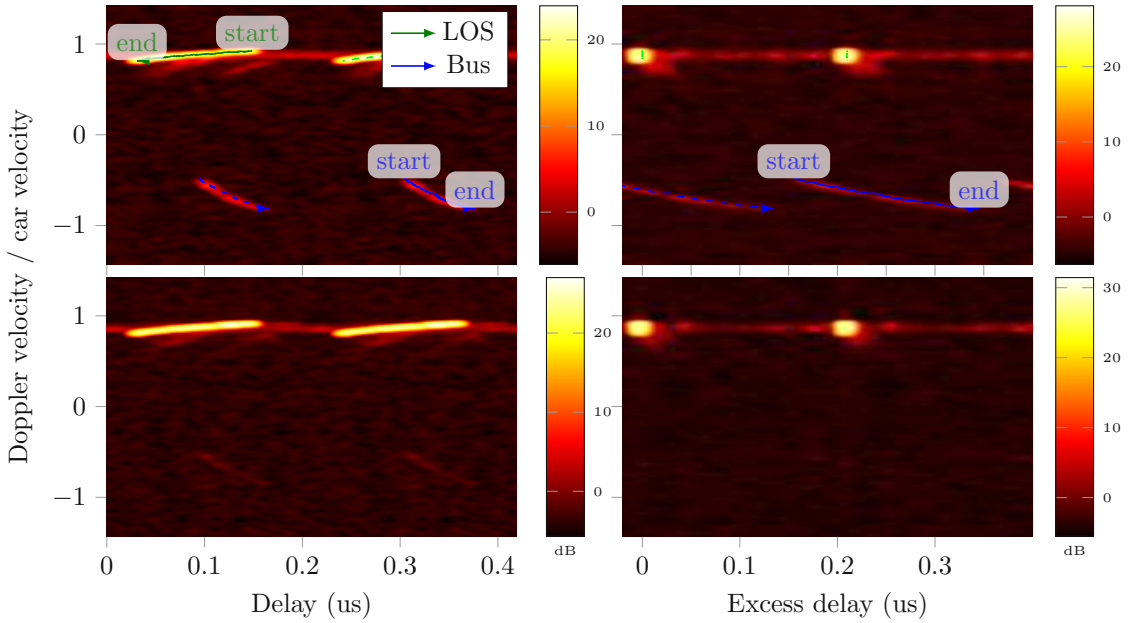

Figure 5.5: Mean delay-Doppler spectrogram (a) and (b) of the time-varying channel of a single measurement run. Delays larger than 0.21 µs are due to aliasing. Mean delay-Doppler spectrogram (c) and (d) of the LOS delay tracked time-varying channel. For averaging, the TX moved within the region $-43.5\,\mathrm{m} < y \leq -8\,\mathrm{m}$. The heatmap is in dB above estimated noise power.

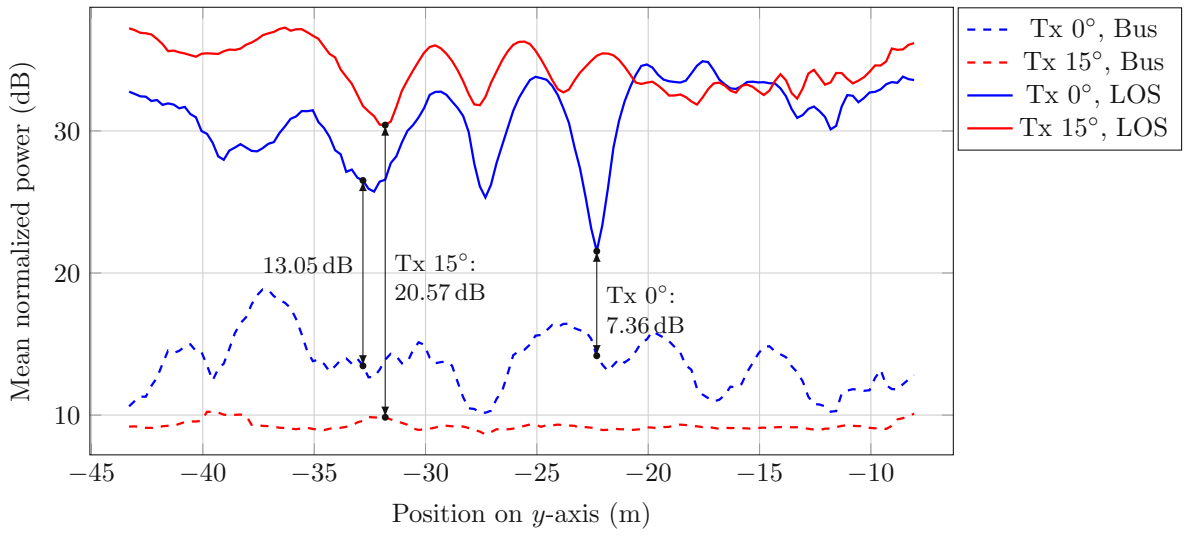

Figure 5.6: Mean power of the LOS delay-Doppler bin and passenger bus delay-Doppler bin for both antennas. Sliding window of 2 m along the position of the TX on y-axis. Minimum power ratio is 7.36 dB for Tx 0° and 20.57 dB for Tx 15°. The power ratio at y-position with wraparound delay is 13 dB.

Doppler bin, $\bar{\mathcal{C}}[l'_{\mathrm{Bus}}, k'_{\mathrm{Bus}}; y]$, are shown in fig. 5.6 with a 2 m sliding window along the y-axis position of the TX for both antennas. $\bar{\mathcal{C}}[l'_{\mathrm{LOS}}, k'_{\mathrm{LOS}}; y]$ is higher for Tx 15° than for Tx 0° for the most part of the track. However, $\bar{\mathcal{C}}[l'_{\mathrm{Bus}}, k'_{\mathrm{Bus}}; y]$ is lower Tx 15° than for Tx 0° and mostly below a noise floor. At $y = y_w$ where the passenger bus MPC has wraparound delay $\Delta\tau_w$, the power ratio between LOS and passenger bus MPC is only 13.05 dB for Tx 0°. The overall minimum power ratio is only 7.36 dB for Tx 0°, and 20.57 dB for Tx 15°.

5.4 Discussion

RMS can not be measured sufficiently with the available channel sounder. Employing omnidirectional antennas at both ends of the channel would probably lead to a higher RMS spread with enough dynamic range of the channel sounder. However, it is questionable if higher dynamic range and directional antennas would lead to fundamentally different results.
The chosen aliasing free max excess delay should be increased for future V2I mm-wave measurement campaigns.
The channel can be split into an environment-specific and in a traffic-specific part. The LOS component is subject to small-scale fading when there is not sufficient spatial filtering of the street surface. For antennas on vehicle roofs, the vehicle surface contributes to small-scale fading. Uptilt beam has higher amount of fading than horizontal beam. More MPCs with significant power can be seen for the horizontal beam than for the uptilt beam. Delay-Doppler domain improves resolvability for tracking.
Tracking the channel in delay leads to smaller delay and Doppler spread of the LOS component. Although other MPCs could experience an increase in delay and Doppler spread, their contribution in power is smaller than the LOS component.

6 Scatterer Identification with Sparse Methods

This chapter is largely based on the published work [72]:

H. Groll, P. Gerstoft, M. Hofer, *et al.*, „Scatterer identification by atomic norm minimization in vehicular mm-wave propagation channels“, *IEEE Access*, vol. 10, pp. 102 334–102 354, 2022. DOI: 10.1109/ACCESS.2022.3205616

The delay-Doppler domain provides an two-dimensional description of the wireless channel with an geometric interpretation when the channel is sparse. Identifying scatterers in a non-parametric spectral approach as in chapter 5 is achieved by finding the spectral peaks of the estimated LSF. However, selecting peaks is related to selecting the model order, a challenging problem inherent also for parametric estimation approaches when the model order is unknown. Parametric approaches can lead to superior results compared to non-parametric approaches with correct model order assumptions and to inferior results with wrong assumptions. Semi-parametric estimation approaches aim at achieving a balance between non-parametric and parametric approaches and impose only a weak model structure, e.g. on the sparsity of the signal. Moreover for estimation methods, the parameters are often restricted to lie on a grid, which could be a severe model mismatch and introduce estimation errors. The atomic norm framework is a semi-parametric approach, assumes sparsity of the signal, and enables gridless parameter estimation by solving a convex optimization problem. To achieve a minimum level of resolution for the investigated V2I mm-wave scenario, the optimization problem needs to increases to a sample size, which is difficult to solve with state-of-the-art solvers. The two-dimensional atomic norm problem can be simplified to a decoupled atomic norm, which reduces the effective size of the optimization problem and allows to identify scatterers of V2I mm-wave channels. Consequently, the identified scatters enable the construction of a sparse parametric representation of a measured channel. The sparse representation should not only be in agreement with the measured channel in terms of the measurement vector, but also in terms of power dispersion in the delay-Doppler domain when the channel is sparse.

In this chapter, I employ the atomic norm framework to identify scatterers in the delay-Doppler domain. I give an overview of sparse methods in section 6.1. I review the atomic norm framework in section 6.1.4, its application to denoising of measurements in section 6.1.4, and the simplification to decoupled atomic norm minimization in the two-

dimensional case in section 6.1.5. I define a numerical simulation model, which is relevant to V2I mm-wave communication, in section 6.2 and briefly introduce a related measurement campaign from a collaborative work in section 6.3. I present the simulation results in section 6.4.1 and the measurement results in section 6.4.2. I provide a discussion at the end of the chapter in section 6.5.

6.1 Sparse Methods

6.1.1 Motivation for Sparse Methods

Estimation tasks require to infer some parameters from data to obtain information about the source location of a physical process, e.g. range of a scatterer from sensor data.
In a *non-parametric* approach, the locations of the highest (separated) peaks of spectrum-like functions are identified as the estimated sources [133]. Examples of non-parametric estimators are the periodogram [85], multitaper spectral estimator [85] as employed in chapter 5, or the subspace based multiple signal classification (MUSIC) [134] spectral estimator, e.g. for the ambiguity domain [135]. Non-parametric estimation techniques are limited in terms of accuracy because no data model is enforced and they suffer from poor resolution for finite samples.
Parametric estimation methods on the other hand rely heavily on data models of sampled observations to achieve higher accuracy than non-parametric methods. The maximum likelihood (ML) technique is a frequently used model-based approach in signal processing to derive the parameters of a model [133]. The statistical framework varies depending on the data generation process of signal and noise. Deterministic ML treats the signal deterministic, depending only the parameters, whereas stochastic ML treats the signal and noise as random processes. The computationally complexity for parametric methods is in general quite high. Popular parametric algorithms, which impose a certain structure of the observed data, are the subspace fitting methods with several variants of the MUSIC algorithm [134], e.g. root-MUSIC [136], or several variants of Estimation Of Signal Parameters Via Rotational Invariance Techniques [137], [138].
Semi-parametric estimation methods are in between the non-parametric and parametric class and aim at finding a trade-off between the two classes by weak assumption on the data model. An important sub-group of semi-parametric methods are sparse estimation methods, which exploit the sparsity of the signal to improve estimation results over non-parametric methods. Examples of sparse methods are the covariance-based SPICE [139], LASSO [140], and atomic norm minimization [55].

6.1.2 Definition of Sparsity

In the mathematical sense, a vector $\mathbf{x} \in \mathbb{R}^N$ is strictly S-sparse if at most S out of its possible N entries are different from zero. A signal is compressible if it allows a

sparse representation by a sparse $\mathbf{x}$ together with a basis or a frame of an inner product space. Imposing a sparsity structure on a signal can result in better quality for signal recovery [141]. In practical situations, noise contaminates a signal of interest such that the signal is never strictly sparse, i.e. the majority of entries are slightly larger than zero. A signal is then approximately S-sparse if its reconstruction from the S-sparse $\mathbf{x}$ is sufficiently good. The main difficulty is to find a transformation into a domain where the signal is approximately sparse. For a large number of problems, the Fourier transform of a signal leads to a domain where the signal representation needs a moderately small number of coefficients. However, the non-locality and oscillatory nature of this transform makes estimation of Fourier coefficients difficult due to mismatch [142].

6.1.3 Discrete Fourier Transform Basis

The basis expansion model (BEM) in eq. (2.9) represents the channel by a weighted sum of their basis vectors. A popular choice for the basis is the DFT, where the critically sampled complex exponential basis is generally not a good choice in the LTV case [143]. Introducing oversampling and windowing of the complex exponential basis usually leads to better fits of a BEM based channel to LTV channels [144]. It is common, e.g. for systems with orthogonal time frequency space modulation [145], to characterize the channel in a two-dimensional grid where one dimension is delay and the other the Doppler domain.
From channel estimates in the form of TVTF $H[k,l]$ (See eq. (3.5)), consecutive samples in time $k = k_0, \ldots, k_{K-1}$ and frequencies $l = l_0, \ldots, l_{L-1}$ are collected in the measurement matrix $\mathbf{Y} \in \mathbb{C}^{K\times L}$ (See eq. (3.10)). The matrix description of the channel in the delay-Doppler domain is $\mathbf{S} \in \mathbb{C}^{K\times L}$, analogous to the smoothed spreading function $S_{\tau,\nu}[l',k']$ (See eq. (2.13)). The inverse DFT with respect to the frequency samples exchanges frequency with delay and the DFT with respect to time samples exchanges time with Doppler domain. With the unitary DFT matrix $\mathbf{F}$ and its inverse $\mathbf{F}^{\mathrm{H}}$, the transformation from time-frequency to delay-Doppler domain is defined via the linear operation

$$\mathbf{Y} = \mathbf{F}_L \mathbf{S} \mathbf{F}_K^{\mathrm{H}} \,, \tag{6.1}$$

where $\mathbf{F}_L \in \mathbb{C}^{L\times L}$ and $\mathbf{F}_K = \mathbb{C}^{K\times K}$. The linear operation is equivalently written in vectorized form

$$\mathbf{y} = (\mathbf{F}_K^* \otimes \mathbf{F}_L)\,\mathrm{vec}(\mathbf{S}), \tag{6.2}$$

where $\mathbf{y} = \mathrm{vec}(\mathbf{Y})$. With the linear operator $\mathbf{A} = (\mathbf{F}_K^* \otimes \mathbf{F}_L)$, the linear channel plus noise model is now

$$\mathbf{y} = \mathbf{A}\,\mathrm{vec}(\mathbf{S}) + \mathbf{z}. \tag{6.3}$$

The matrix $\mathbf{A} \in \mathbb{C}^{LK\times LK}$ is a critically-sampled complex exponential basis. An over-complete complex exponential basis $\tilde{\mathbf{A}} = \tilde{\mathbf{F}}^*_{K,\tilde{K}} \otimes \tilde{\mathbf{F}}_{L,\tilde{L}}$ is obtained by a DFT matrix with more coefficients and subsequent truncation. This basis $\tilde{\mathbf{A}}$ thus represents a grid

with a smaller grid spacing than $\mathbf{A}$. The transformation matrix the delay domain is $\tilde{\mathbf{F}}_{L,\tilde{L}} \in \mathbb{C}^{L\times\tilde{L}}$ with $\tilde{L} > L$ and for the Doppler domain $\tilde{\mathbf{F}}_{K,\tilde{K}} \in \mathbb{C}^{K\times\tilde{K}}$ with $\tilde{K} > K$, such that $\tilde{\mathbf{A}}$ has more columns than rows. Based on this overcomplete basis, the linear channel plus noise model becomes

$$\mathbf{y} = \tilde{\mathbf{A}}\,\mathrm{vec}(\tilde{\mathbf{S}}) + \mathbf{z}, \tag{6.4}$$

where $\tilde{\mathbf{S}} \in \mathbb{C}^{\tilde{K}\times\tilde{L}}$ is the interpolated basis coefficient matrix. Mathematically, eq. (6.4) is a linear undetermined system of linear equations. A solution is given, e.g. by a least squares estimate $\tilde{\mathbf{S}}_{\mathrm{LS}}$. However, the number of basis coefficients needed in $\tilde{\mathbf{S}}_{\mathrm{LS}}$ is usually large, due to a grid mismatch between basis and measurements.

Sparse solution via the LASSO. Methods for finding a sparse solution for $\tilde{\mathbf{S}}$ in eq. (6.4) can put a penalty on the number of coefficients larger than zero. A direct way for this penalty is via the ℓ_0-norm $\|\mathrm{vec}(\tilde{\mathbf{S}})\|_0$, which leads to a non-convex optimization problem for finding $\tilde{\mathbf{S}}$. The LASSO [140] method relaxes this non-convex problem to the following convex optimization problem

$$\underset{\tilde{\mathbf{S}}}{\text{minimize}} \|\tilde{\mathbf{A}}\,\mathrm{vec}(\tilde{\mathbf{S}}) - \mathbf{z}\|_2 \qquad \text{subject to} \quad \|\mathrm{vec}(\tilde{\mathbf{S}})\|_1 \leq \lambda, \tag{6.5}$$

by employing a ℓ_1-norm penalty with a regularization parameter λ for tuning between the least squares solution for $\lambda = \infty$ and shrinking the coefficients for $\lambda < \infty$.
The performance of the results depend also on the choice of the basis $\tilde{\mathbf{A}}$ and its associated grid, which can lead to severe grid mismatch errors.

6.1.4 Atomic Norm

The atomic norm framework [146] overcomes the grid mismatch problem with a parametric basis. For the two-dimensional DFT basis described in section 6.1.3, the parametric basis is a set of two-dimensional complex exponentials [147]. The composition of S basis vectors is the two-dimensional complex exponential signal

$$\mathbf{X} = \sum_{s=1}^{S} c_s \mathbf{a}_\nu(\bar{\nu}_s)\mathbf{a}_\tau(\bar{\tau}_s)^{\mathrm{T}}, \tag{6.6}$$

with complex coefficient c_s, normalized delay $\bar{\tau}_s \in [0,1)$, normalized Doppler $\bar{\nu}_s \in [-0.5, 0.5)$ and complex exponential basis vectors

$$\begin{aligned} \mathbf{a}_\nu(\bar{\nu}_s) &= [1 \;\; e^{j2\pi\bar{\nu}_s} \;\; \ldots \;\; e^{j2\pi(N_\nu-1)\bar{\nu}_s}]^{\mathrm{T}}, & \bar{\nu}_s &\in [-\tfrac{1}{2}, \tfrac{1}{2}), \\ \mathbf{a}_\tau(\bar{\tau}_s) &= [1 \;\; e^{-j2\pi\bar{\tau}_s} \;\; \ldots \;\; e^{-j2\pi(N_\tau-1)\bar{\tau}_s}]^{\mathrm{T}}, & \bar{\tau}_s &\in [0,1), \end{aligned}$$

for N_ν time and N_τ frequency samples, respectively. The linear signal model for an observed two-dimensional sample matrix $\mathbf{Y} \in \mathbb{C}^{N_\nu \times N_\tau}$ is

$$\mathbf{Y} = \mathbf{X} + \mathbf{Z}, \tag{6.7}$$

with unobserved signal $\mathbf{X} \in \mathbb{C}^{N_\nu \times N_\tau}$ as in eq. (6.6) and additive noise $\mathbf{Z} \in \mathbb{C}^{N_\nu \times N_\tau}$. The framework of atomic norm minimization helps in finding the sparsest representation of $\mathbf{X}$ with atoms from the atomic set $\mathcal{A}$, i.e. a parametric basis defined as [147]

$$\mathcal{A} = \{e^{j\varphi}\mathbf{a}_\nu(\bar{\nu})\mathbf{a}_\tau(\bar{\tau})^{\mathrm{T}} \,:\, \bar{\nu} \in [-\tfrac{1}{2}, \tfrac{1}{2}), \bar{\tau} \in [0, 1), \varphi \in [0, 2\pi)\}. \tag{6.8}$$

The continuous parameters $\bar{\tau}$ and $\bar{\nu}$ are the normalized versions of delay and Doppler, respectively, with $\bar{\tau} = \frac{\tau}{\tau_{\max}}$ and $\bar{\nu} = \frac{\nu}{\nu_{\max}}$. The vectorized two-dimensional atomic norm $\|\mathrm{vec}(\mathbf{X})\|_{\mathcal{A}}$, induced by the atomic set $\mathcal{A}$, is the function

$$\|\mathrm{vec}(\mathbf{X})\|_{\mathcal{A}} = \inf\{w \geq 0 | \mathbf{X} \in w \cdot \mathrm{conv}(\mathcal{A})\} \tag{6.9}$$

which gauges the model order to express $\mathbf{X}$ as a convex combination with atoms of $\mathcal{A}$, i.e. the atomic decomposition eq. (6.6), where $\mathrm{conv}(\mathcal{A})$ is the convex hull of $\mathcal{A}$. Lagrangian duality theory is an important aspect in understanding the atomic norm. The dual of the atomic norm involves finding the maximum absolute value of a bounded complex trigonometric polynomial defined with respect to $\mathcal{A}$, for which there is an approximate semi-definite program (SDP) optimization solution for two-dimensions [55], [147].
The atomic norm in eq. (6.9) is approximated by solving a SDP [147]

$$\begin{aligned} 2 \cdot \|\mathrm{vec}(\mathbf{X})\|_{\mathcal{A}} \approx \min_{\hat{\mathbf{X}},\mathbf{u},w} \quad & \frac{1}{N_\tau N_\nu}\mathrm{Tr}\left(\mathbf{T}_2(\mathbf{u})\right) + w, \\ \text{s.t.} \quad & \begin{bmatrix} \mathbf{T}_2(\mathbf{u}) & \mathrm{vec}(\hat{\mathbf{X}}) \\ \mathrm{vec}(\hat{\mathbf{X}})^{\mathrm{H}} & w \end{bmatrix} \succeq \mathbf{0}, \\ & \hat{\mathbf{X}} = \mathbf{X}, \end{aligned} \tag{6.10}$$

where $\mathbf{T}_2(\mathbf{u}) \in \mathbb{C}^{N_\tau N_\nu \times N_\tau N_\nu}$ is a block-Toeplitz matrix with Toeplitz blocks, further described together with sequence $\mathbf{u}$ in section 6.1.4, $w \in \mathbb{R}^+$ is a free optimization variable, $(\frac{1}{N_\tau N_\nu}\mathrm{Tr}\left(\mathbf{T}_2(\mathbf{u})\right) + w)$ is the trace-norm[1] of the positive semi-definite (PSD) matrix constraint of size $(N_\tau N_\nu + 1) \times (N_\tau N_\nu + 1)$, and $\hat{\mathbf{X}}$ is an optimization variable constrained to the full noiseless observation $\mathbf{Y} = \mathbf{X}$, non-compressed sensing case. The atomic norm $\|\cdot\|_{\mathcal{A}}$ in eq. (6.9) is already a convex relaxed version similar to the convex relaxation from ℓ_0-norm to ℓ_1-norm in sparse recovery algorithms [55], e.g. LASSO.
The rank of $\mathbf{T}_2(\mathbf{u})$ and the number of atoms S are related. Therefore, a low rank solution is desired for a sparse model. Rank minimization is the connection between the trace-norm formulation and actual atomic norm minimization[148, (2.19)].

[1] also known as nuclear norm

The underlying atoms of eq. (6.6), i.e. $\mathbf{a}_\nu(\bar{\nu})\mathbf{a}_\tau(\bar{\tau})^{\mathrm{T}}$ from estimates $\hat{\bar{\tau}}$ and $\hat{\bar{\nu}}$, are retrieved only after evaluating a dual polynomial of the dual problem, finding the roots of the dual polynomial, or from Vandermonde decomposition [149] of $\mathbf{T}_2(\mathbf{u})$. For the last two cases, there is no need for model selection [55]. For Vandermonde decomposition, the number of atoms S corresponds to the rank of $\mathbf{T}_2(\mathbf{u})$ [149].
The block Toeplitz matrix obtained from atomic norm minimization SDP is now assumed to have $\operatorname{rank}(\mathbf{T}) = r < \min(N_\tau, N_\nu)$ so that a Vandermonde decomposition exists[149]. The matrix pencil and auto-pairing (MAPP) method [149] is able to recover the frequencies (τ_j, ν_j) from $\mathbf{T}$ with $j = 1, \ldots, S$.
I chose the Vandermonde decomposition with MAPP approach to recover (τ_j, ν_j), due to the implicit model selection and the availability of a robust algorithm [149].
A mapping from normalized to non-normalized estimates is achieved with $\hat{\tau} = \frac{\hat{\bar{\tau}}}{\Delta f}$ and $\hat{\nu} = \frac{\hat{\bar{\nu}}}{T_{\mathrm{R}}}$.

Resolution Limit

The atomic norm method is gridless, but even for the noiseless case it suffers from a resolution limit such that recovery guarantees exist only for the case of atoms fulfilling a separation condition [55]. However, incorporating prior knowledge can improve the resolution, e.g. with reweighted atomic norm minimization [150]. Furthermore, empirical results suggest less strict separation conditions than current theoretical results [148].

Atomic Soft Thresholding

In the presence of noise $\mathbf{Z}$, atomic norm minimization requires an additional term for denoising [43] the observed sample matrix $\mathbf{Y}$. The two-dimensional ANM problem in eq. (6.10) is modified through additional soft thresholding[2], and can approximately be retrieved with the SDP [60], [147]

$$\begin{aligned} \underset{\hat{\mathbf{X}},\mathbf{u},w}{\operatorname{argmin}} \quad & \frac{\mu'}{N_\tau N_\nu}\operatorname{Tr}(\mathbf{T}_2(\mathbf{u})) + \mu' w + \|\hat{\mathbf{X}} - \mathbf{Y}\|_F^2 \\ \text{s.t.} \quad & \begin{bmatrix} \mathbf{T}_2(\mathbf{u}) & \operatorname{vec}(\hat{\mathbf{X}}) \\ \operatorname{vec}(\hat{\mathbf{X}})^{\mathrm{H}} & w \end{bmatrix} \succeq \mathbf{0}, \end{aligned} \tag{6.11}$$

where $\|\hat{\mathbf{X}} - \mathbf{Y}\|_F$ measures quality of reconstruction and the remaining terms promote sparsity of the optimal solution. A trade-off between measurement reconstruction and sparsity is set with the regularization parameter μ', similar to the LASSO in eq. (6.5). Although no model order selection is needed, the choice of regularizer μ' depends on both the noise model and noise level as shown for the one-dimensional case in [43] and empirically set to

$$\mu_e = \sigma_Z \sqrt{N_\nu N_\tau \ln(N_\nu N_\tau)} \tag{6.12}$$

[2] denoising

for the two-dimensional case [60] for complex Gaussian matrix $\mathbf{Z}$ with i.i.d. entries $Z_{ij} \sim \mathcal{CN}(0, \sigma_Z^2)$. I refer to the vectorized ANM with soft thresholding in eq. (6.11) as ANM in the following, as the focus in this chapter is on noisy observations from measurement data.

Toeplitz Structure

In a stochastic treatment of $\mathbf{X}$ as random matrix, the covariance matrix of $\mathbf{X}$ is

$$\mathbf{R}_{\mathbf{X}} = \mathbb{E}\left\{\mathrm{vec}(\mathbf{X})\mathrm{vec}(\mathbf{X})^{\mathrm{H}}\right\}, \tag{6.13}$$

where it is common to estimate $\mathbf{R}_{\mathbf{X}}$ through the sample covariance matrix

$$\hat{\mathbf{R}}_{\mathbf{X}} = \sum_{i}^{I} \mathrm{vec}(\mathbf{X}_i)\mathrm{vec}(\mathbf{X}_i)^{\mathrm{H}} \tag{6.14}$$

from I measurement snapshots. The PSD constraint in the SDP eq. (6.10) has the role of this sample covariance matrix with lack of sufficient snapshots to be further well-conditioned [151]. The trace norm of the Toeplitz matrix acts as an ℓ_1 norm on the eigenvalues of the Toeplitz matrix, thus leading to a low-rank matrix [151].
The Hermitian block-Toeplitz matrix $\mathbf{T}_2(\mathbf{u})$ has a block structure, where each block is a Toeplitz matrix. The structure of $\mathbf{T}_2(\mathbf{u})$ originates from a single atom $\mathbf{a}_\tau(\bar{\tau}_s) \otimes \mathbf{a}_\nu(\bar{\nu}_s)$ out of $\mathcal{A}$ in the form $(\mathbf{a}_\tau(\bar{\tau}_s)\mathbf{a}_\tau(\bar{\tau}_s)^{\mathrm{H}}) \otimes (\mathbf{a}_\nu(\bar{\nu}_s)\mathbf{a}_\nu(\bar{\nu}_s)^{\mathrm{H}})$ [147]. Extending to the vectorized two-dimensional complex exponential matrix $\mathrm{vec}(\mathbf{X})$ in a deterministic view, [149, see also eq. (9)], or alternatively eq. (6.14) with a single snapshot, leads to

$$\begin{aligned}
\mathrm{vec}(\mathbf{X})\mathrm{vec}(\mathbf{X})^{\mathrm{H}} &= \sum_{s=1}^{S} |c_s|^2 \,\mathrm{vec}(\mathbf{a}_\nu(\bar{\nu}_s)\mathbf{a}_\tau(\bar{\tau}_s)^{\mathrm{T}})\mathrm{vec}(\mathbf{a}_\nu(\bar{\nu}_s)\mathbf{a}_\tau(\bar{\tau}_s)^{\mathrm{T}})^{\mathrm{H}} \\
&= \sum_{s=1}^{S} |c_s|^2 \,[\mathbf{a}_\tau(\bar{\tau}_s) \otimes \mathbf{a}_\nu(\bar{\nu}_s)][\mathbf{a}_\tau(\bar{\tau}_s) \otimes \mathbf{a}_\nu(\bar{\nu}_s)]^{\mathrm{H}} \\
&= \sum_{s=1}^{S} |c_s|^2 \,[\mathbf{a}_\tau(\bar{\tau}_s)\mathbf{a}_\tau(\bar{\tau}_s)^{\mathrm{H}}] \otimes [\mathbf{a}_\nu(\bar{\nu}_s)\mathbf{a}_\nu(\bar{\nu}_s)^{\mathrm{H}}],
\end{aligned} \tag{6.15}$$

where a block structure is evident through the Kronecker product. Although the number of paths S is unknown in eq. (6.15), the SDP eq. (6.11) allows to find a block-Toeplitz matrix $\mathbf{T}_2(\mathbf{u})$ with similar structure, where the number of significant eigenvalues of $\mathbf{T}_2(\mathbf{u})$ provide an estimate of S. Then, the complex sequence $\mathbf{u} = (u)_{n_\nu, n_\tau}$ with $n_\nu = [-(N_\nu - 1), \ldots, N_\nu - 1]$ and $n_\tau = [-(N_\tau - 1), \ldots, N_\tau - 1]$ fully parameterizes $\mathbf{T}_2(\mathbf{u})$ [149,

eq. (3)]

$$\mathbf{T}_2(\mathbf{u}) = \begin{bmatrix} \mathbf{T}_1(\mathbf{u}_0) & \mathbf{T}_1(\mathbf{u}_1) & \dots & \mathbf{T}_1(\mathbf{u}_{(N_\tau-1)}) \\ \mathbf{T}_1(\mathbf{u}_{-1}) & \mathbf{T}_1(\mathbf{u}_0) & \dots & \mathbf{T}_1(\mathbf{u}_{(N_\tau-2)}) \\ \vdots & \vdots & \ddots & \vdots \\ \mathbf{T}_1(\mathbf{u}_{(1-N_\tau)}) & \mathbf{T}_1(\mathbf{u}_{(2-N_\tau)}) & \dots & \mathbf{T}_1(\mathbf{u}_0) \end{bmatrix}, \tag{6.16}$$

where $\mathbf{u}_k = (u)_{n_\nu, n_\tau = k}$ is a subsequence of $\mathbf{u}$ and each block itself a Toeplitz matrix $\mathbf{T}_1(\mathbf{u}_k) \in \mathbb{C}^{N_\nu \times N_\nu}$ [149, eq. (2)]. In a sum-of-Kronecker-products form, $\mathbf{T}_1(\mathbf{u}_k)$ is

$$\mathbf{T}_1(\mathbf{u}_k) = (u)_{0,k}\mathbf{I}_{\mathbf{N}_\nu} + \sum_{l=1}^{N_\nu - 1} (u)_{l,k}\mathbf{\Theta}_{N_\nu}^{(l)} + (u)_{-l,k}\mathbf{\Theta}_{N_\nu}^{(-l)}, \tag{6.17}$$

where $\mathbf{\Theta}_K^{(k)} \in \mathbb{R}^{K \times K}$ is a matrix with all ones on the k-th off-diagonal and zeros elsewhere. Note, that $\mathbf{\Theta}_K^{(-k)}$ is the transpose of $\mathbf{\Theta}_K^{(k)}$. Due to the Hermitian property, $\mathbf{T}_1(\mathbf{u}_k) = \mathbf{T}_1(\mathbf{u}_{-k})^{\mathrm{H}}$. The sum-of-Kronecker-products form of eq. (6.16) is

$$\mathbf{T}_2(\mathbf{u}) = \mathbf{I}_{\mathbf{N}_\tau} \otimes \mathbf{T}_1(\mathbf{u}_0) + \sum_{k=1}^{N_\tau - 1} \mathbf{\Theta}_{N_\tau}^{(k)} \otimes \mathbf{T}_1(\mathbf{u}_k) + \sum_{k=1}^{N_\tau - 1} \mathbf{\Theta}_{N_\tau}^{(-k)} \otimes \mathbf{T}_1(\mathbf{u}_k)^{\mathrm{H}}. \tag{6.18}$$

The parameterization of $\mathbf{T}_2(\mathbf{u})$ through the sequence $\mathbf{u}$ limits the degrees of freedom of the PSD matrix in the optimization eq. (6.11).

6.1.5 Decoupled Atomic Norm Minimization

SDPs based algorithms for atomic norm minimization grow in complexity with the problem size, especially for more than one dimension as considered in the vectorized two-dimensional delay-Doppler case in this thesis. The authors [152] propose to solve the atomic norm minimization problem in a decoupled way. In view of the reweighted atomic norm minimization [150], a reweighted decoupled atomic norm minimization algorithm is derived in [153]. Increasing snapshots in time N_ν or frequency samples N_τ, the SDP considered in eq. (6.11) quickly increases the Toeplitz matrix size in eq. (6.16) beyond a feasible size for available SDP solvers[3].

The atomic norm in a matrix formulation enables to solve the atomic norm minimization problem efficiently approximately solved in an decoupled way [154], instead of the vectorized model matrix $\mathrm{vec}(\mathbf{X})$ in eq. (6.9). Taking N_ν sequential snapshots of a signal with one-dimensional complex exponentials

$$\mathbf{x}[n_\nu] = \sum_{s=1}^{S} c_s[n_\nu]\mathbf{a}_\tau(\bar{\tau}_s), \tag{6.19}$$

[3] See sections III-D and IV-C in [72] for a discussion on limited observation time and SDP solver complexity.

with equidistant time spacing between $\mathbf{x}[n_\nu]$, the multiple measurement snapshot $[\mathbf{x}[0] \ \dots \ \mathbf{x}[N_\nu - 1]]^{\mathrm{T}} \approx \mathbf{X}$ exhibits a two-dimensional structure as in eq. (6.6) for $[c_s[0] \ \dots \ c_s[N_\nu - 1]]^{\mathrm{T}} = c_s \mathbf{a}_\nu(\bar{\nu}_s)$ and stationary τ_s. This is applicable to the sample matrix $\mathbf{Y}$ and model matrix $\mathbf{X}$ and thus interpreted as a two-dimensional snapshot.
For the number of paths $S \leq \min(N_\nu, N_\tau)$, the solution for the optimization problem is found with the D-ANM SDP [154, eq. (28)]

$$\begin{aligned} \underset{\hat{\mathbf{X}}, \mathbf{u}_\nu, \mathbf{u}_\tau}{\operatorname{argmin}} \quad & \frac{\mu}{\sqrt{N_\nu N_\tau}} \left[\operatorname{Tr}\left(\mathbf{T}_1(\mathbf{u}_\tau)\right) + \operatorname{Tr}\left(\mathbf{T}_1(\mathbf{u}_\nu)\right) \right] + \|\hat{\mathbf{X}} - \mathbf{Y}\|_F^2 \\ \text{s.t.} \quad & \begin{bmatrix} \mathbf{T}_1(\mathbf{u}_\tau) & \hat{\mathbf{X}}^{\mathrm{H}} \\ \hat{\mathbf{X}} & \mathbf{T}_1(\mathbf{u}_\nu) \end{bmatrix} \succeq \mathbf{0}, \end{aligned} \tag{6.20}$$

where $\mathbf{T}_1(\mathbf{u}_\tau) \in \mathbb{C}^{N_\tau \times N_\tau}$ and $\mathbf{T}_1(\mathbf{u}_\nu) \in \mathbb{C}^{N_\nu \times N_\nu}$ denote single level Toeplitz matrices with recoverable delay $\hat{\tau}$ and Doppler frequency $\hat{\nu}$ by separate Vandermonde decomposition of each Toeplitz matrix. The choice of regularizer μ in eq. (6.20) trades sparsity for data reconstruction, similar to ANM in eq. (6.11). Furthermore, for D-ANM I employ the same empirical value μ_e eq. (6.12) as for ANM.
Note the reduced size of the PSD constraint in eq. (6.20) is $(N_\tau + N_\nu) \times (N_\tau + N_\nu)$ compared to the ANM formulation in eq. (6.11) where it is $(N_\tau N_\nu + 1) \times (N_\tau N_\nu + 1)$. The model order S depends on $\operatorname{rank}(\mathbf{T}_1(\mathbf{u}_\tau))$, $\operatorname{rank}(\mathbf{T}_1(\mathbf{u}_\nu))$, and on if delay or Doppler of paths do overlap [154].
I employ a matrix pencil method [149, eq. (33)] for Vandermonde decomposition and parameter recovery where the poles of the characteristic polynomial of $\mathbf{T}_1$ are found as a solution of a generalized eigenvalue problem [155, eq. (13)]. In contrast to vectorized ANM, an additional pairing step is now necessary. First, I try all possible combinations of $(\hat{\tilde{\tau}}_i, \hat{\tilde{\nu}}_s), i = 1, \dots, S_\tau, \ s = 1, \dots, S_\nu$ and then I only keep the pairs with strongest contribution $|\mathbf{a}_\nu(\hat{\tilde{\nu}}_s)^{\mathrm{H}} \hat{\mathbf{X}} \mathbf{a}_\tau(\hat{\tilde{\tau}}_i)^*|$. As an additional constraint for pairing, each $\hat{\tilde{\tau}}_i$ and $\hat{\tilde{\nu}}_s$ can appear only once. This approach is similar to finding the main peaks in the two-dimensional conventional beamformer. The number of significant eigenvalues of $\mathbf{T}_1(\mathbf{u}_\tau)$ and $\mathbf{T}_1(\mathbf{u}_\nu)$ provide estimates of S_τ and S_ν, respectively.
The applicability of D-ANM on the estimated TVTF matrix (see section 3.2) is justified due to the interpretation of the multiple snapshots of one-dimensional channel transfer functions as a single snapshot in a time-frequency region, where Doppler modulation introduces phase changes only visible across multiple snapshots, i.e. delay and Doppler domains can be treated independently for underspread LTV channels.

6.1.6 Sparse Representation

The goal is to estimate delay and Doppler of the significant MPCs. The ANM SDP in eq. (6.11) and D-ANM in eq. (6.20) both derive from the sample matrix $\mathbf{Y}$ a denoised version $\hat{\mathbf{X}}$ and a block-Toeplitz matrix with Toeplitz blocks $\mathbf{T}_2(\mathbf{u})$ or $\mathbf{T}_1(\mathbf{u}_\tau)$ and $\mathbf{T}_1(\mathbf{u}_\nu)$, respectively, from where S delay-Doppler pairs $\{\hat{\tau}_s, \hat{\nu}_s \mid s = 1, \dots, S\}$ are recovered.

A parameterized atomic decomposition as in eq. (6.6), where also $\mathbf{X} = \mathbf{Y} - \mathbf{Z}$, still requires complex-valued path amplitudes $\mathbf{c} = [c_1 \ \dots \ c_S]^{\mathrm{T}}$. Therefore, I construct a basis $\mathbf{A}_{\hat{\tau}} = [\mathbf{a}_\tau(\hat{\tau}_1) \ \dots \ \mathbf{a}_\tau(\hat{\tau}_S)]$ and $\mathbf{A}_{\hat{\nu}} = [\mathbf{a}_\nu(\hat{\nu}_1) \ \dots \ \mathbf{a}_\nu(\hat{\nu}_S)]$ and retrieve an estimate $\hat{\mathbf{c}} = [\hat{c}_1 \ \dots \ \hat{c}_S]^{\mathrm{T}}$ from the sample matrix $\mathbf{Y}$ with a common least-squares approach

$$\hat{\mathbf{c}} = \mathbf{B}^{\dagger}\mathrm{vec}(\mathbf{Y}), \tag{6.21}$$

where $\mathbf{B} = [\mathbf{b}(\hat{\tau}_1, \hat{\nu}_1) \ \dots \ \mathbf{b}(\hat{\tau}_S, \hat{\nu}_S)]$ with column-wise Kronecker products $\mathbf{b}(\hat{\tau}_s, \hat{\nu}_s) = \mathbf{a}_\tau(\hat{\tau}_s) \otimes \mathbf{a}_\nu(\hat{\nu}_s)$.
A sparse representation of the wireless channel, limited in time and frequency, is now given with

$$\tilde{\mathbf{H}} = \mathbf{A}_{\hat{\nu}} \, \mathrm{diag}\,(\hat{\mathbf{c}}) \mathbf{A}_{\hat{\tau}}^{\mathrm{T}}, \tag{6.22}$$

and described by the parameter set $\{\hat{c}_s, \hat{\tau}_s, \hat{\nu}_s \mid s = 1, \dots, S\}$ only.
For model evaluation, I define the normalized approximation error (NAE)

$$\mathrm{NAE}(\tilde{\mathbf{H}}; \mathbf{Y}) = \sqrt{E\left\{ \frac{\|\mathbf{Y} - \tilde{\mathbf{H}}\|_F^2}{\|\mathbf{Y}\|_F^2} \right\}}, \tag{6.23}$$

as an error metric for measuring the quality of reconstructing the sample matrix $\mathbf{Y}$ with the sparse representation $\tilde{\mathbf{H}}$.

6.2 Numerical Simulation Model

For the application of ANM methods to V2I mm-wave channels, a direct path between a moving TX and a low number of further resolvable specular components seems characteristic. Due to the employment of band-limited system , fading of MPCs magnitudes need to be considered in simulation.
I simulate a nonstationary radio channel based on the geometry-based stochastic channel model as shown in fig. 6.1. The simulated propagation environment consists of a static RX at the origin, a TX moving with constant magnitude velocity vector $|\mathbf{v}_{\mathrm{TX}}|$, and several static point-scatterers with coordinates drawn from two independent spatial distributions. The location parameters of the spatial distributions are random with $r_1, r_2 \sim \mathcal{U}(r_{\min}, r_{\max})$ and $\phi_1, \phi_2 \sim \mathcal{U}(0, 2\pi)$. I define a cluster as a group of point-scatterers with parameters from the same distribution and the cluster center as the distribution's location parameter. Each cluster consists of N_{MPC} point-scatterers, i.i.d. Gaussian in two-dimensional space with cluster spread a_s, i.e. point-scatterer positions are at spatial coordinate $x \sim \mathcal{N}(r_s \cos\phi_s, a_s^2)$, $y \sim \mathcal{N}(r_s \sin\phi_s, a_s^2)$. I consider multi-path propagation where the LOS component is associated with a direct path from TX to RX and several MPCs are each associated with a path from TX to RX trough a single bounce at a single point-scatterer. The MPC amplitudes are complex Gaussian distributed. For large N_{MPC} this leads to a Rayleigh distributed envelope of the received

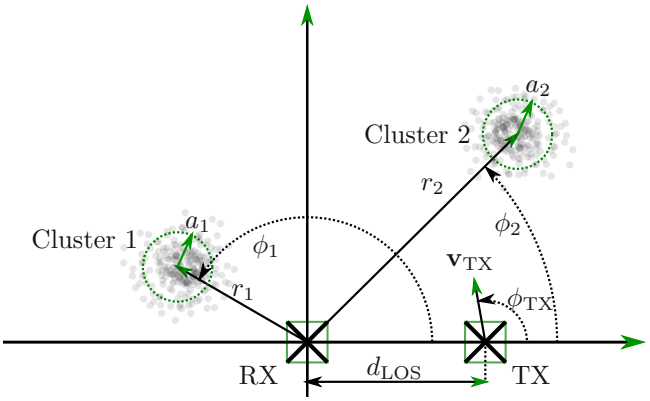

Figure 6.1: Simple cluster model with a receiver (RX), one moving transmitter (TX), and two clusters of point-scatterers with cluster spread a_1 and a_2.

signal, which is a suitable model for spatially uniform terrain for mm-wave [156]. A similar time-varying scattering model for diffuse scattering is shown in [157]. The MPCs due to point-scatterers located within a small area are later identified as a resulting single MPC due to insufficient resolution. Furthermore, the magnitude of a resulting MPC fluctuates.

First, a single realization of all positions and a randomly chosen direction ϕ_{TX} drawn from the uniform distribution $\mathcal{U}(0, 2\pi)$ is fixed. Then, the TX starts at distance d_{LOS} from RX at $t = 0$ and moves in direction ϕ_{TX}. The movement of the TX leads to a change in path delays for the LOS component and all scattered MPCs, which introduces a Doppler shift, c.f. eq. (5.6).

The frequency domain channel model is defined in terms of the band-limited, complex valued base-band formulation

$$H_{\mathrm{SC}}[k,l] = H_{\mathrm{LOS}}[k,l] + \sum_{s=1}^{S-1} H_{\mathrm{Cl}(s)}[k,l], \tag{6.24}$$

where the k-th transfer functions corresponds to time $t = kT_{\mathrm{R}}$, l is the frequency index, $H_{\mathrm{LOS}}[k,l]$ is the LOS component, and $H_{\mathrm{Cl}(s)}[k,l]$ is the s-th cluster of several MPCs. I define the components as

$$H_{\mathrm{LOS}}[k,l] = g_{\mathrm{LOS}}[k] e^{-j2\pi f_l \tau_{\mathrm{LOS}}[k]}, \tag{6.25}$$

$$H_{\mathrm{Cl}(s)}[k,l] = \sum_{m=1}^{N_{\mathrm{MPC(s)}}} g_{\mathrm{MPC}(s,m)}[k] e^{-j2\pi f_l \tau_{\mathrm{MPC}(s,m)}[k]}, \tag{6.26}$$

where $g_{\mathrm{LOS}}[k]$ and $g_{\mathrm{MPC}(s,m)}[k]$ are complex-valued amplitudes, $\tau_{\mathrm{LOS}}[k]$ is LOS propagation delay, $\tau_{\mathrm{MPC}(s,m)}[k] = \tau_{\mathrm{Cl}(s)}[k] + \Delta\tau_{\mathrm{MPC}(s,m)}[k]$ is the propagation delay of a multipath centered around cluster delay $\tau_{\mathrm{Cl}(s)}[k]$ of the geometric model with deviations

$\Delta\tau_{\mathrm{MPC}(s,m)}[k]$, and $f_l = f_\mathrm{c} + l\Delta f - \frac{B}{2}$ is the subcarrier frequency. I approximate the time-varying delays for $0 \leq kT_\mathrm{R} < T_\mathrm{obs}$ as

$$\tau[k] = \tau - kT_\mathrm{R}\frac{\nu}{f_\mathrm{c}} \tag{6.27}$$

such that for $\frac{B}{f_\mathrm{c}} \ll 1$

$$\begin{aligned} e^{-j2\pi f_l \tau[k]} &= e^{-j2\pi\left(f_\mathrm{c}+l\Delta f-\frac{B}{2}\right)\left(\tau-kT_\mathrm{R}\frac{\nu}{f_\mathrm{c}}\right)} \\ &\approx e^{j2\pi(kT_\mathrm{R}\nu - l\Delta f\tau)-j\varphi} \end{aligned} \tag{6.28}$$

and insert it into eq. (6.25) and eq. (6.26) to get the approximations

$$H_\mathrm{LOS}[k,l] \approx g_\mathrm{LOS}[k] e^{j2\pi(kT_\mathrm{R}\nu_\mathrm{LOS} - l\Delta f\tau_\mathrm{LOS})-j\varphi_{\tau_\mathrm{LOS}}}, \tag{6.29}$$

$$\begin{aligned} H_{\mathrm{Cl}(s)}[k,l] &= g_{\mathrm{Cl}(s)}[k,l] e^{-j2\pi l\Delta f\tau_{\mathrm{Cl}(s)}[k]} \\ &\approx g_{\mathrm{Cl}(s)}[k,l] e^{j2\pi\left(kT_\mathrm{R}\nu_{\mathrm{Cl}(s)} - l\Delta f\tau_{\mathrm{Cl}(s)}\right)-j\varphi_{\tau_{\mathrm{Cl}(s)}}}, \end{aligned} \tag{6.30}$$

where ν_LOS and $\nu_{\mathrm{Cl}(s)}$ are Doppler shifts for the LOS component and the cluster, respectively. The complex-valued amplitudes are combined in the fluctuating cluster amplitude

$$g_{\mathrm{Cl}(s)}[k,l] = \sum_{m=1}^{N_{\mathrm{MPC(s)}}} g_{\mathrm{MPC}(s,m)}[k] e^{-j2\pi l\Delta f\Delta\tau_{\mathrm{MPC}(s,m)}[k]}. \tag{6.31}$$

The fluctuations in $g_\mathrm{LOS}[k]$ and $g_{\mathrm{Cl}(s)}[k,l]$ are important factors for a deviation of eq. (6.24) from the model in eq. (2.9), where the number of discrete MPCs is S. It includes one LOS component and $S-1$ clusters.
I model the path amplitude for the LOS component as

$$g_\mathrm{LOS}[k] = \frac{1}{\sqrt{L_P[k]}} e^{j\varphi_0}, \tag{6.32}$$

where $L_P[k] = (4\pi d_\mathrm{LOS}[k] f_\mathrm{c}/c_0)^2$ is the free-space path loss of the LOS component, φ_0 is an initial phase offset, and c_0 is the speed of light. For the MPCs

$$g_{\mathrm{MPC}(s,m)}[k] = g_\mathrm{LOS}[k] a_{\mathrm{MPC}(s,m)} \frac{g_s}{\sqrt{N_{\mathrm{MPC(s)}}}}, \tag{6.33}$$

with $a_{\mathrm{MPC}(s,m)} \sim \mathcal{CN}(0,1)$ and an additional coefficient g_s due to additional path loss and reflectivity. The phase offsets $\varphi_{\tau_\mathrm{LOS}}$ and $\varphi_{\tau_{\mathrm{Cl}(s)}}$ are absorbed into φ_0 and $a_{\mathrm{MPC}(s,m)}$. N_ν snapshots in time, and N_τ frequency samples of $H_\mathrm{SC}[k,l]$ are combined into the time-frequency matrix $\mathbf{X}_\mathrm{SC} \in \mathbb{C}^{N_\tau \times N_\nu}$. For each realization of $\mathbf{X}_\mathrm{SC}$, only the position of TX changes. I aim in estimating the parameters for the LOS component and clusters of a realization $\mathbf{X}_\mathrm{SC} \approx \mathbf{X}$, where the discrete MPC model in eq. (6.6) serves as an approximation.

6.3 Measurement Campaign

The application of algorithms like MUSIC often leads to poor estimation results in small samples and at low SNR scenarios [133]. Unfortunately, the measurement data employed in previous sections provides only low SNR. A follow-up V2I mm-wave multiband measurement campaign was presented in [9] and provides measurement data of the wireless channel at 62.35 GHz at higher SNR and slightly more bandwidth.

Figure 6.2 shows a map of the measurement scenario with a static RX and a moving TX car. The car drives along the street towards the cross-roads in a urban street environment. The effective velocity of the LOS component, see eq. (5.6), is visible as heatmap.

Figure 6.3 shows the antenna platforms with employed antennas. The RX employs a directive antenna, directed towards the traffic light. The TX employs an omnidirectional antenna mounted at the roof of the car. Of all the bands in this measurement campaign [9], only the 62.35 GHz band is considered in this thesis.

The wireless channel is measured with a multicarrier channel sounder, see section 3.2, with $N_\tau = 155$ subcarriers, freqeuncy spacing $\Delta f = 1\,\text{MHz}$, and a bandwidth of $B = 155\,\text{MHz}$. Therefore, $\Delta\tau = 6.45\,\text{ns}$ is the spacing between delay taps, which corresponds to 1.93 m separation in propagation distance. Estimates of the time-varying transfer function (TVTF) $\hat{H}[k,l]$, see eq. (3.5), are available at a channel snapshot period $T_\text{R} = 125\,\mu\text{s}$.

The LSF estimate $\hat{\mathcal{C}}[l',k';t_b]$ in eq. (5.1) enables to investigate the wireless channel in the delay-Doppler domain within an observation time $T_\text{obs} = N_\nu T_\text{R} = 64\,\text{ms}$, i.e. $N_\nu = 512$ snapshots of TVTF, and centered at time t_b. Figure 6.4 shows $\hat{\mathcal{C}}[l',k';t_1]$ and $\hat{\mathcal{C}}[l',k';t_2]$, which are calculated using eq. (5.1) for two selected time regions t_1 and t_2 during a passing maneuver. The LOS component is clearly visible and most dominant MPCs could be from a nearby fence on the western side of the road [9] and from light posts.

At the beginning of the recording, the first arrived path has minimum delay as the TX car passes the RX and enters the main lobe of the receive antenna pattern. The car heads towards the cross-roads and a maximum negative Doppler shift is observed in $\hat{\mathcal{C}}[l',k';t_1]$ at t_1 with MPCs reaching $\nu > 2\,\text{kHz}$. The difference in delay between the first arrival and the next MPCs is still relatively high at t_1. The first arrival and follow-up MPCs start to merge in delay domain for $\hat{\mathcal{C}}[l',k';t_2]$ at t_2 and the given bandwidth. I assume the presence of a LOS component and several clusters of MPCs in the delay-Doppler domain, by inspection of the LSFs at t_1 and t_2. Single bounce paths allow a trivial geometric interpretation by employing delay-Doppler estimates of MPCs and positions of RX and TX, as analyzed for the measurement campaign in chapter 5. Here, a possible location of the single bounce for the path, with the earliest arrival time after the LOS component, is close to a lamp post, as shown in fig. 6.2.

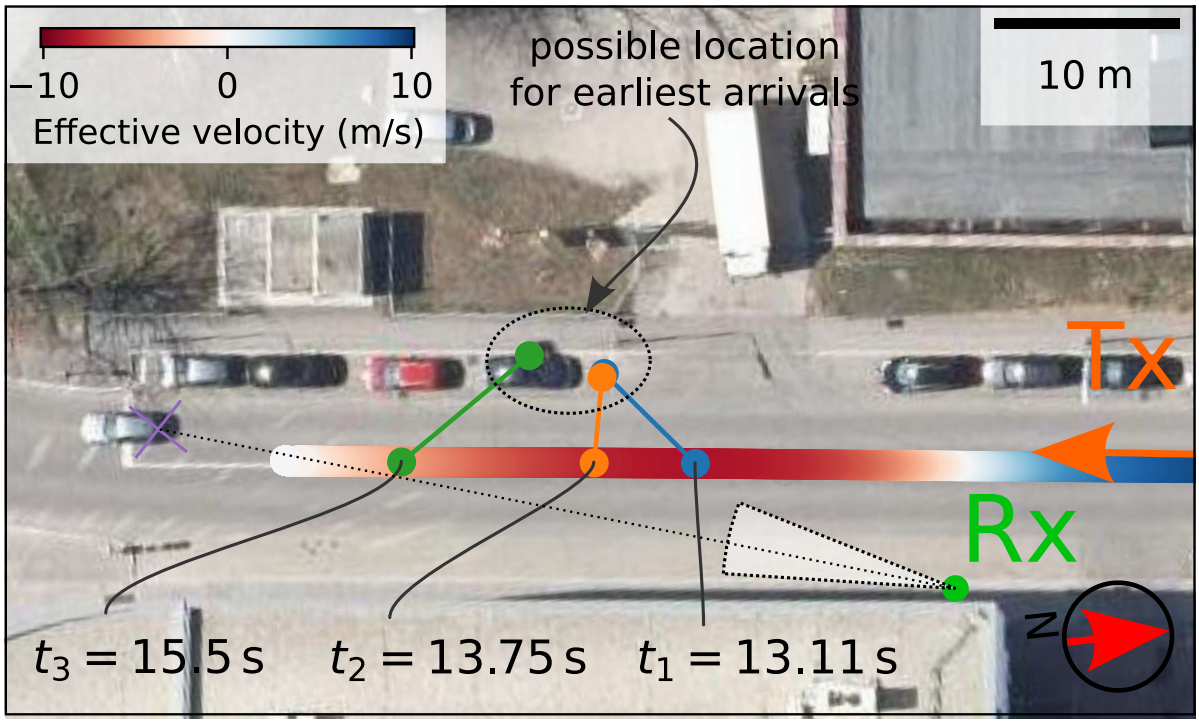

Figure 6.2: Orthophoto map of the TX trajectory, the static RX at position, the RX steering direction of the employed antenna, and its half power beam width (HPBW) during the measurement campaign [9]. The effective velocity v_{TX} of the TX with respect to RX is shown along the trajectory. Single bounce paths allow a geometric interpretation using the delay-Doppler estimates and positions of RX and TX. A possible location of the single bounce for the path, with the earliest arrival time after the line of sight component, is close to a lamp post for t_1, t_2, and t_3. Only one parked car was present during the measurement (the second from left). Map: Stadt Wien – https://data.wien.gv.at.

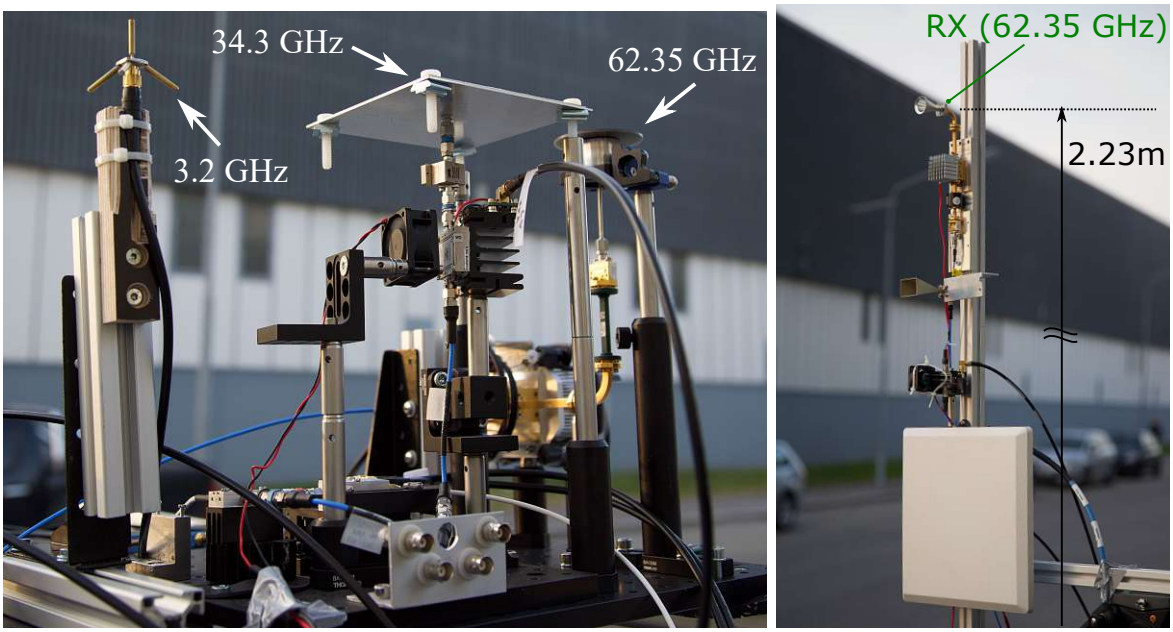

Figure 6.3: Antenna platforms of (left) the TX car and (right) the fixed RX of the multiband measurement campaign [9].

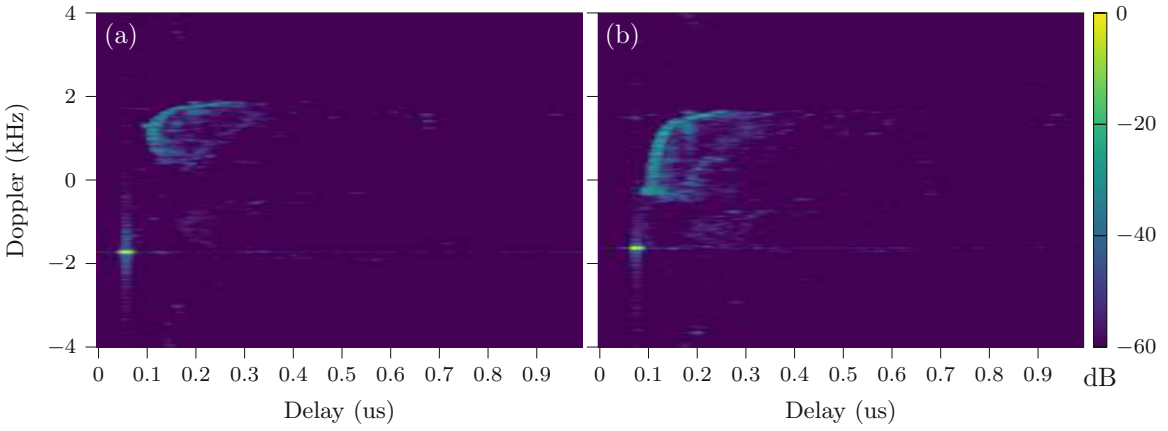

Figure 6.4: Local scattering function (LSF) with $\Delta\nu = 15.625\,\text{Hz}$ Doppler resolution due to 64 ms observation time ($N_\nu = 512$, $T_\text{R} = 125\,\text{us}$) for selected times (a) 13.11 s and (b) 13.75 s.

6.4 Results

First, I apply the methods ANM and D-ANM on simulations of the presented simulation model of section 6.2 in section 6.4.1. Then, I apply the same methods on measurement data in section 6.4.2.

6.4.1 Simulation Data

I choose the simulation parameters for a vehicular communication system designed for maximum resolvable velocity $\mathrm{v}_{\max} = 20\,\mathrm{m/s}$, maximum excess delay $\tau_{\max} = 0.3\,\mu\mathrm{s}$, center frequency $f_\mathrm{c} = 60\,\mathrm{GHz}$, and bandwidth $B = 160\,\mathrm{MHz}$. The maximum Doppler frequency is $\nu_{\max} = \mathrm{v}_{\max}\frac{f_\mathrm{c}}{c_0} = 4\,\mathrm{kHz}$ for single bounce paths. The TX starts at a distance $d_{\mathrm{LOS}} = 5\,\mathrm{m}$. The location parameters r_1 and r_1 of the point-scatterers' spatial distributions are randomly distributed between $r_{\min} = 5\,\mathrm{m}$ and $r_{\max} = \tau_{\max}\frac{c_0}{2} - \frac{d_{\mathrm{LOS}}}{2} = 42.5\,\mathrm{m}$. They consist of $N_{\mathrm{MPC}} = 1000$ point-scatterers each with a cluster spread $a_s \in [0, 8\,\mathrm{m}]$. According to [109, Sec. 9.1 p. 239], 6 MPCs are sufficient for a Rayleigh distributed envelope. However, when the spatial density of the point-scatterers decreases, individual scatterers may become resolvable and 6 MPCs could be insufficient to achieve a Rayleigh distributed envelope. For MPCs to become resolvable by ANM or D-ANM, they have to fulfill a minimum separation condition [154], i.e. $\Delta_{\min,\tau} \geq \frac{N_\tau \Delta\tau}{\lfloor (N_\tau - 1)/4 \rfloor} = \frac{50 \cdot 6.25\,\mathrm{ns}}{12} = 26.0\,\mathrm{ns}$ for $N_\tau = 50$ or $\Delta_{\min,\nu} \geq \frac{N_\nu \Delta\nu}{\lfloor (N_\nu - 1)/4 \rfloor} = \frac{16 \cdot 500\,\mathrm{Hz}}{3} = 2.67\,\mathrm{kHz}$ for $N_\nu = 16$. To this end, I discard realizations of the simple cluster model if the minimum separation condition is violated regarding the cluster centers.
I choose $N_\tau \geq \tau_{\max} B = 0.3 \times 160 = 48$ to prevent aliasing in delay. Each cluster is attenuated by $-g_s = 6\,\mathrm{dB}$ relative to the LOS component.
I generate multiple LTV realizations $\mathbf{X}_{\mathrm{SC}}$ of the model in Sec. section 6.2 and add complex Gaussian noise $\mathbf{Z} \in \mathbb{C}^{N_\nu \times N_\tau}$, with i.i.d. entries $Z_{ij} \sim \mathcal{CN}(0, \sigma_Z^2)$. The velocity vector and scatterer positions are constant during one realization $\mathbf{X}_{\mathrm{SC}}$. I define the array SNR as $\mathrm{SNR} = 10\log_{10}\left(\|\mathbf{X}_{\mathrm{SC}}\|_F^2 / \left(N_\tau N_\nu \sigma_Z^2\right)\right)$. I set $\mathrm{SNR} = 30\,\mathrm{dB}$ and normalize the sample matrix $\mathbf{Y} = \mathbf{X}_{\mathrm{SC}} + \mathbf{Z}$ such that $\|\mathbf{Y}\|_F^2 = N_\tau N_\nu$. I apply the ANM of eq. (6.11), where the result of the SDP is a denoised matrix $\hat{\mathbf{X}}$ and a generated block-Toeplitz matrix $\mathbf{T}_2(\mathbf{u})$, where each block is a Toeplitz matrix itself. The regularizer μ' defines the trade-off between sparsity of the model structure and reconstruction error of the simulation data with added noise and model mismatch. A Vandermonde decomposition of $\mathbf{T}_2(\mathbf{u})$ with the MAPP method [149] recovers delay-Doppler pairs $(\hat{\tau}_s, \hat{\nu}_s)$. The number of pairs is known for the simulation and limited to $S = 3$.
Next, I employ D-ANM to estimate delay-Doppler pairs. The sample matrix $\mathbf{Y}$ for D-ANM is normalized as in the ANM case. The solution of the SDP in eq. (6.20) is a denoised matrix $\hat{\mathbf{X}}$ and two Toeplitz matrices $\mathbf{T}_1(\mathbf{u}_\tau)$ and $\mathbf{T}_1(\mathbf{u}_\nu)$. For recovering the parameters from $\mathbf{T}_1(\mathbf{u}_\tau)$ and $\mathbf{T}_1(\mathbf{u}_\nu)$, the number of estimated parameters S (significant MPCs) corresponds to the number of significant eigenvalues of the Toeplitz matrices. I set $S_\tau = \min(3, N_{\lambda(\tau)})$ and $S_\nu = \min(3, N_{\lambda(\nu)})$, where $N_{\lambda(\nu)}$ and $N_{\lambda(\tau)}$ are the number

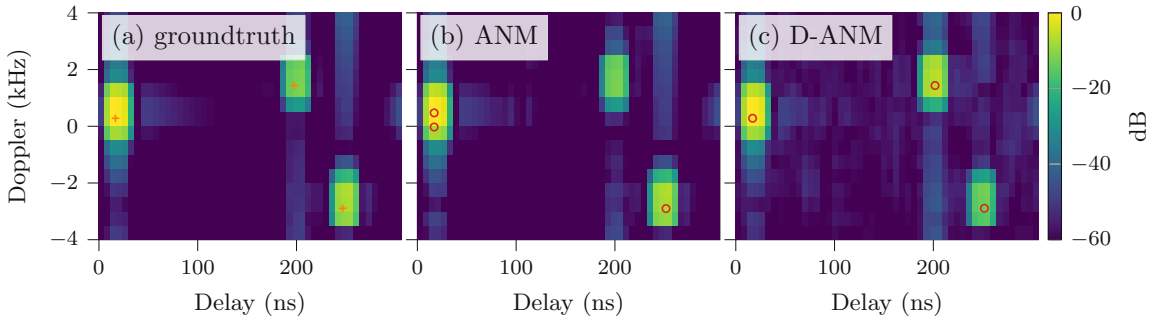

Figure 6.5: Simulation with cluster spread 2 mm, $N_\tau = 50$, $N_\nu = 16$. (a) The true cluster parameters (+) $(\tau_{\mathrm{Cl}(s)}, \nu_{\mathrm{Cl}(s)})$. Recovered delay-Doppler pairs (o) $(\hat{\tau}_s, \hat{\nu}_s)$ with (b) atomic norm minimization (ANM) eq. (6.11) with $\mu' = \mu_e$ and (c) decoupled ANM (D-ANM) eq. (6.20) with $\mu = \mu_e$. Background colors are the LSFs, normalized to maximum, with the samples from (a) $\mathbf{X}_{\mathrm{SC}}$, (b) ANM denoised $\hat{\mathbf{X}}$, and (c) D-ANM denoised $\hat{\mathbf{X}}$, respectively.

of significant eigenvalues of $\mathbf{T}_1(\mathbf{u}_\tau)$ and $\mathbf{T}_1(\mathbf{u}_\nu)$ with magnitude not smaller than 20 dB of the largest eigenvalue each. Pairing of delay and Doppler parameters is described in section 6.1.5.

Figure 6.5(a) shows the true cluster parameters (+) $(\tau_{\mathrm{Cl}(s)}, \nu_{\mathrm{Cl}(s)})$ for the simulation with cluster spread 2 mm, $N_\tau = 50$, and $N_\nu = 16$. Delay-Doppler pairs (o) $(\hat{\tau}_s, \hat{\nu}_s)$ are shown in fig. 6.5(b) for recovery with ANM eq. (6.11) with $\mu' = \mu_e$ and in fig. 6.5(c) for recovery with D-ANM eq. (6.20) with $\mu = \mu_e$. Although the strong LOS component is modeled as a single discrete path, two delay-Doppler estimates with ANM are quite near to the strong LOS component (fig. 6.5(b) (20 ns, 0.5 kHz)). This frequency splitting effect is visible in all the simulations with ANM eq. (6.11), which could be due to spectral leakage [85]. A further significant MPC corresponding to the remaining cluster is not identified. The delay-Doppler estimates with D-ANM in fig. 6.5(c) are in high agreement with the true cluster parameters.

For random LTV channels, I estimate the nonstationary spectral process with the LSF in eq. (5.1) from the TVTF $\hat{H}[k, l; t_b]$ eq. (3.9) limited to a region in time and frequency. Similarly, I now calculate an equivalent LSF with the samples of the time-frequency regions $\mathbf{X}_{\mathrm{SC}}$ and $\hat{\mathbf{X}}$, respectively, for their description in the delay-Doppler domain. The background color in fig. 6.5(a) shows the LSF of a single realization $\mathbf{X}_{\mathrm{SC}}$ from the simulation model eq. (6.24), the LSF of the denoised $\hat{\mathbf{X}}$ with ANM eq. (6.11) in fig. 6.5(b), and LSF of the denoised $\hat{\mathbf{X}}$ with D-ANM eq. (6.20) in fig. 6.5(c). The delay-Doppler estimates with D-ANM in fig. 6.5(c) are in high agreement with the LSF of the denoised $\hat{\mathbf{X}}$ in the background. Compared to fig. 6.5(b), the effect of denoising is less pronounced in fig. 6.5(c). Although the LSF of the denoised $\hat{\mathbf{X}}$ in fig. 6.5(b) looks remarkably similar to the ground truth in fig. 6.5(a), the estimated parameters for ANM are only partially in agreement with the true cluster parameters. Therefore, I consider

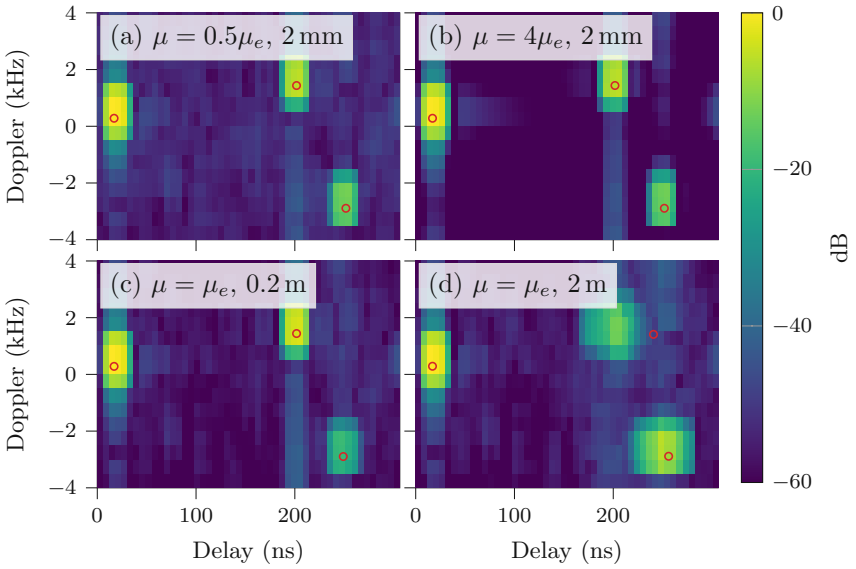

Figure 6.6: Decoupled ANM (D-ANM) applied to the simple cluster model eq. (6.24) with model parameters as in fig. 6.5(a). The recovered delay-Doppler pairs (o) $(\hat{\tau}_s, \hat{\nu}_s)$ are from noisy samples with D-ANM eq. (6.20). Top row: cluster spread $a_s = 2\,\text{mm}$, (a) $\mu = 0.5\mu_e$, (b) $\mu = 4\mu_e$. See also fig. 6.5(c) with $\mu = \mu_e$ and $a_s = 2\,\text{mm}$. Bottom row: $\mu = \mu_e$, increase in cluster spread (c) $100 \times a_s = 0.2\,\text{m}$, (d) $1000 \times a_s = 2\,\text{m}$. $N_\tau = 50$, $N_\nu = 16$. Background colors are the LSFs, normalized to maximum, with the samples D-ANM denoised matrix $\hat{\mathbf{X}}$.

the vectorized ANM to be of little use for the employed model. Furthermore, the high computational complexity of the SDP eq. (6.11) makes it susceptible to numerical and convergence issues [158].

To this end, I restrict the remaining discussion of the simulation results to the D-ANM method in eq. (6.20).

Figure 6.6(a)–(d) show the D-ANM recovered delay-Doppler parameter pairs (o) for $N_\tau = 50$, $N_\nu = 16$ and the LSFs of D-ANM denoised $\hat{\mathbf{X}}$ eq. (6.20) of the same single time-frequency realization $\mathbf{X}_{\text{SC}}$ as in fig. 6.5. The intensity of the denoising effect depends on the regularizer μ as shown in fig. 6.6(a) and fig. 6.6(b) (see also fig. 6.5(c)). The empirical value $\mu = \mu_e$ eq. (6.12) as in fig. 6.5(c) is a reasonable choice according to the observed simulation results. An increase in cluster spread from $a_s = 2\,\text{mm}$ in fig. 6.5 to $100 \times a_s = 0.2\,\text{m}$ in fig. 6.6(c) still achieves good estimation accuracy of the cluster centers. At larger cluster spreads $1000 \times a_s = 2\,\text{m}$ in fig. 6.6(d) the algorithm fails to identify one of the clusters because the cluster spread is too large.

I compare the estimation accuracy between the estimated and the simulated model in terms of estimated delay-Doppler pairs $(\hat{\tau}_k, \hat{\nu}_k)$ with the cluster parameters $(\tau_{\text{Cl}(s)}, \nu_{\text{Cl}(s)})$

with an Euclidean distance

$$d(s,k) = \sqrt{\left(\frac{\tau_{\mathrm{Cl}(s)} - \hat{\tau}_k}{\tau_{\max}}\right)^2 + \left(\frac{\nu_{\mathrm{Cl}(s)} - \hat{\nu}_k}{2\nu_{\max}}\right)^2}, \tag{6.34}$$

where for $s = S$, $\tau_{\mathrm{Cl}(S)} = \tau_{\mathrm{LOS}}$ and $\nu_{\mathrm{Cl}(S)} = \nu_{\mathrm{LOS}}$.
Due to an association problem, I choose the best pairing i.e.

$$d_s = \min_k d(s,k). \tag{6.35}$$

If the number of detected components $K < S$, $d(s,k) = \sqrt{2}$ for $k = K+1, \ldots, S$, i.e. the maximum error. This serves as a penalty for undetected clusters. I employ the root mean squared error (RMSE) for the metric eq. (6.35) as

$$\mathrm{RMSE} = \sqrt{E\left\{\frac{1}{S}\sum_s d_s^2\right\}}, \tag{6.36}$$

where the expectation is with respect to all realizations of the simple cluster model (see section 6.2) and different noise realizations.
The RMSE over 10 model realizations each with 4 noise realizations for different problem sizes is shown in fig. 6.7 for problem sizes (a) $N_\tau = 50$, $N_\nu = 16$, (b) $N_\tau = 100$, $N_\nu = 8$, and (c) $N_\tau = 155$, $N_\nu = 128$. The RMSE fluctuates strongest for problem size (a) and increases for all problem sizes (a)–(c) with μ, where μ close to the empirical μ_e eq. (6.12) gives the best results on average. The value of μ and cluster spread shows only minor changes for RMSE of problem size (b). The cluster spreads do not influence the RMSE significantly until spreads reach the order of the propagation distance due to delay resolution, i.e. $\Delta\tau c_0 = 1.87\,\mathrm{m}$, where the effect is most dramatic for problem size (c). However, for problem size (c), cluster spreads near $a_s = 0.4\,\mathrm{m}$ result in a very low RMSE.
Next, I evaluate the applicability of the sparse representation $\tilde{\mathbf{H}}$ eq. (6.22) on the noiseless sampled TVTF with different previously defined problem sizes (a)–(c). I denote $\tilde{\mathbf{H}}$ with parameters from the geometric model as $\tilde{\mathbf{H}}_{\mathrm{SC}}$ and $\tilde{\mathbf{H}}$ with estimated parameters through D-ANM eq. (6.20) as $\tilde{\mathbf{H}}_{\mathrm{DANM}}$. The $\mathrm{NAE}(\cdot\,; \mathbf{X}_{\mathrm{SC}})$, in eq. (6.23), of the matrix $\mathbf{X}_{\mathrm{SC}} \in \mathbb{C}^{N_\nu \times N_\tau}$ depending on the cluster spread is shown in fig. 6.8 for $\tilde{\mathbf{H}}_{\mathrm{SC}}$ and $\tilde{\mathbf{H}}_{\mathrm{DANM}}$.
$\mathrm{NAE}(\tilde{\mathbf{H}}_{\mathrm{SC}}; \mathbf{X}_{\mathrm{SC}})$ increases with cluster spread as the limited number of parameters become insufficient in approximating the MPCs constituted by a cluster of point-scatterers as a single MPC with increased delay-Doppler spread. In fig. 6.8 I see two types of mismatch: On the one hand, for low levels of cluster spread I see an error floor in (c) due to violation of the WSSUS assumption because the TX is moving. On the other hand, for high cluster spreads starting at $10^{-1}\,\mathrm{m}$, the Fourier basis does not provide a good expansion of the channel. Furthermore, for very large spreads of point-scatterers, the clusters are not an inadequate model for a specular reflection but for diffuse scattering [157].

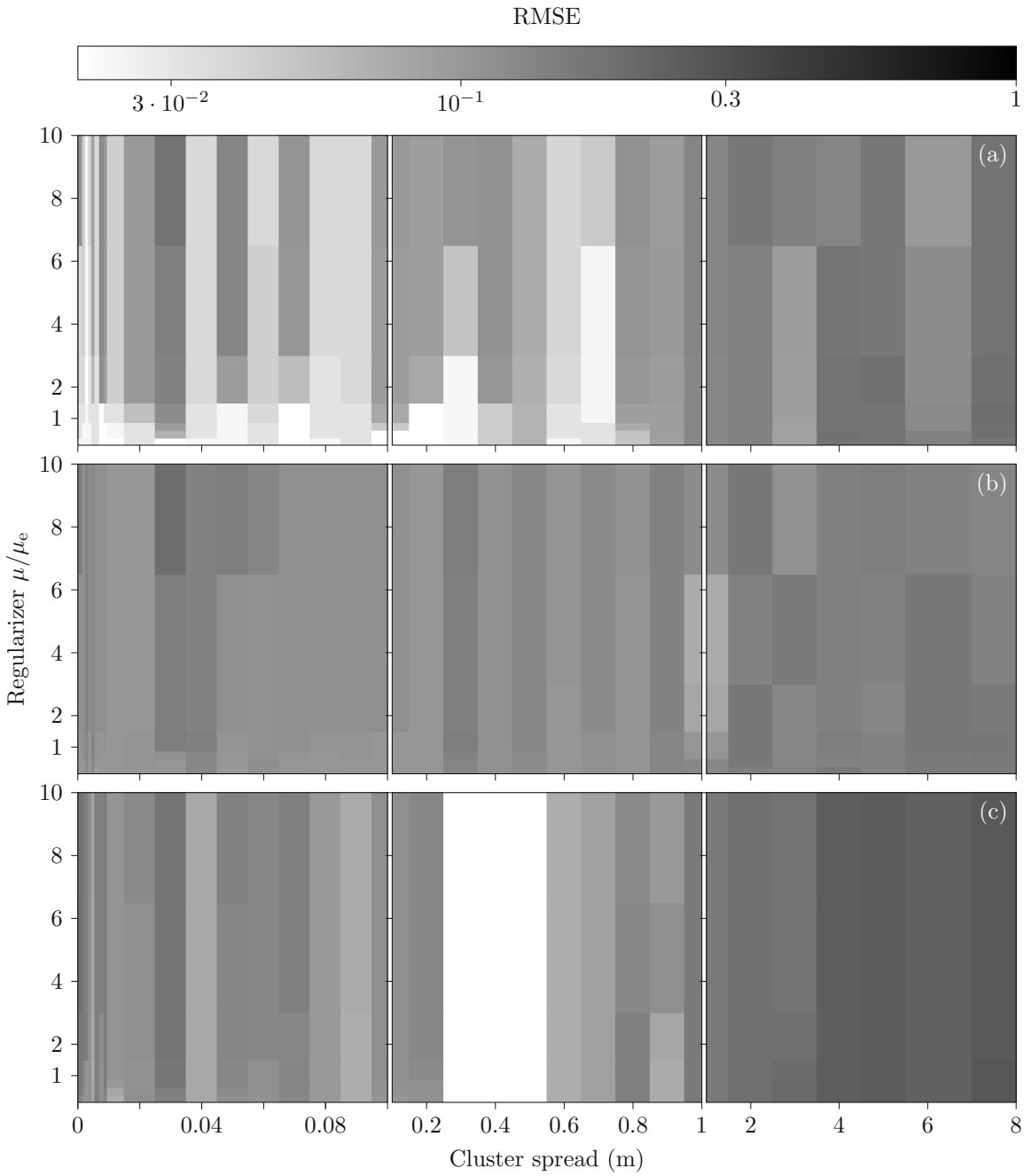

Figure 6.7: Root mean squared error (RMSE) eq. (6.36) over 10 realizations of the simple cluster model each with 4 noise realizations with different cluster spreads and regularization of D-ANM in eq. (6.20). Problem size (a) $N_\tau = 50$, $N_\nu = 16$, (b) $N_\tau = 100$, $N_\nu = 8$, and (c) $N_\tau = 155$, $N_\nu = 128$. At 60 GHz, a cluster spread 1 m corresponds to 200λ. For propagation delay $\Delta\tau = 1/B = 1/160\,\text{MHz}$, propagation distance is $\Delta\tau c_0 = 1.87\,\text{m}$.

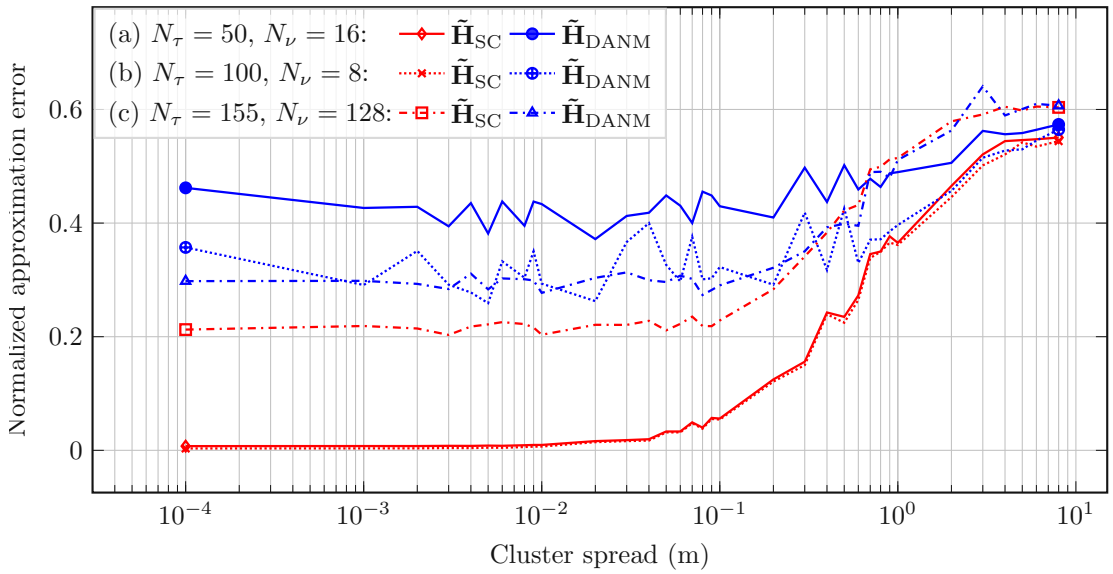

Figure 6.8: Normalized approximation error $\mathrm{NAE}(\,\cdot\,;\mathbf{X}_{\mathrm{SC}})$ eq. (6.23) vs. cluster spread over 10 realizations of the simple cluster model each with 4 noise realizations for $\mu = \mu_e$. (a) $N_\tau = 50$, $N_\nu = 16$, (b) $N_\tau = 100$, $N_\nu = 8$, (c) $N_\tau = 155$, $N_\nu = 128$. Sparse representation with cluster parameters $\tilde{\mathbf{H}}_{\mathrm{SC}}$ and estimated parameters $\tilde{\mathbf{H}}_{\mathrm{DANM}}$ from decoupled ANM (D-ANM).

The sparse representation with D-ANM parameter estimates has an $\mathrm{NAE}(\tilde{\mathbf{H}}_{\mathrm{DANM}};\mathbf{X}_{\mathrm{SC}})$ which starts at medium to high NAE (> 0.3) for low cluster spreads and approaches $\mathrm{NAE}(\tilde{\mathbf{H}}_{\mathrm{SC}};\mathbf{X}_{\mathrm{SC}})$ with increased cluster spread, see fig. 6.8. Although absolute delay drifts get larger with longer observation times as in (c), the sparse representation from estimated parameters results in a better approximation of matrix $\mathbf{X}_{\mathrm{SC}}$ with low cluster spreads than for (a)–(b) shorter observation times. Furthermore, for (c) the difference between $\mathrm{NAE}(\tilde{\mathbf{H}}_{\mathrm{DANM}};\mathbf{X}_{\mathrm{SC}})$ and $\mathrm{NAE}(\tilde{\mathbf{H}}_{\mathrm{SC}};\mathbf{X}_{\mathrm{SC}})$ is small (< 0.1).

6.4.2 Measurement Data

The weak influence of small cluster spreads in the simulation model to identify clusters as discrete MPCs prompts further investigation of D-ANM on measurement data. Nonetheless, I first analyze two selected time regions t_1 and t_2, and the corresponding sample matrices $\mathbf{Y}$ eq. (3.10) of the measurement at $f_c = 62.35\,\mathrm{GHz}$, further with vectorized ANM eq. (6.11) applied to $\mathbf{Y}$. Afterwards, I apply the D-ANM method to the measurement data.

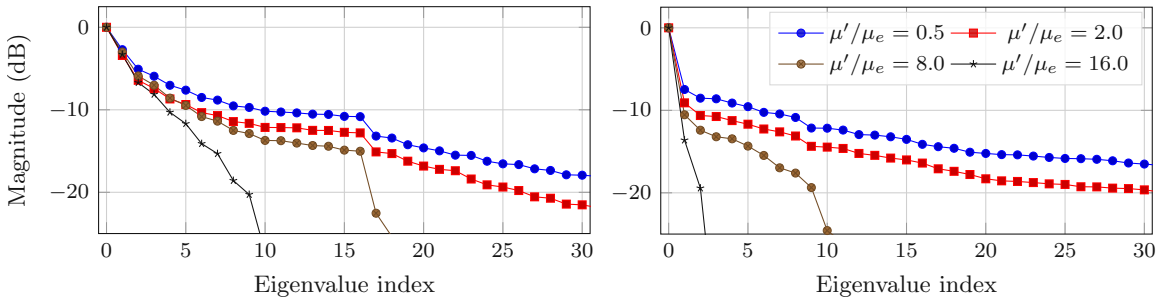

Figure 6.9: Eigenvalues of recovered Toeplitz matrix $\mathbf{T}_2(\mathbf{u})$ for different regularizer values μ'. Top: $t_1 = 13.11\,\mathrm{s}$, bottom: $t_2 = 13.75\,\mathrm{s}$ recording time. Normalized with first eigenvalue.

Measurement Evaluation with ANM

The result of the vectorized ANM SDP is a ANM denoised matrix $\hat{\mathbf{X}}$ and a block-Toeplitz matrix with Toeplitz blocks $\mathbf{T}_2(\mathbf{u})$, with delay-Doppler parameters encoded in the later. Figure 6.9 shows the eigenvalues of recovered $\mathbf{T}_2(\mathbf{u})$ for $N_\nu = 16$, $N_\tau = 77$, and different regularizer values μ'. With increasing μ', the SDP generates $\mathbf{T}_2(\mathbf{u})$ with fewer eigenvalues, where their magnitudes are close to the largest eigenvalue magnitude. A breakpoint in eigenvalue magnitude is clearly visible in t_1 at eigenvalue index 16, which could indicate the maximum rank of the Toeplitz block-Toeplitz structure. From a noise power estimate $\hat{\sigma}^2$ from measurement data, empirical values $\mu' = \mu_e$ eq. (6.12) are $\mu_e[t_1] = 4.31$ and $\mu_e[t_2] = 6.37$ for the given problem size. Higher μ' often lead to a failure in solving the SDP with the employed solver.

The number of parameter estimates corresponds to the significant eigenvalues of $\mathbf{T}_2(\mathbf{u})$. I estimate the delay-Doppler pairs with the two-dimensional MAPP algorithm on $\mathbf{T}_2(\mathbf{u})$ and restrict the number of pairs to $S = \min(N_\nu, N_\tau) = 16$ for MAPP. The restriction is a consequence of the rank of $\mathbf{T}_2(\mathbf{u})$ as described in section 6.1.6. I sort the delay-Doppler pairs in decreasing order of their corresponding power estimates with MAPP [149].

Figure 6.10 shows the $S = 16$ largest peaks of the LSF $\hat{\mathcal{C}}[l', k'; t_b]$ eq. (5.1) for time-frequency snapshots (+) and the recovered delay-Doppler pairs $(\hat{\tau}_s, \hat{\nu}_s)$ (o) from $\mathbf{T}_2(\mathbf{u})$ derived with ANM and $\mu' = 0.5\mu_e$, $\mu' = \mu_e$, and $\mu' = 4\mu_e$. At recording time t_1, the largest LSF peak (60 ns, −1.8 kHz) corresponds to the strong LOS component where neighboring peaks with similar delay or Doppler are likely due to spectral leakage despite data tapering. Further LSF peaks with delay $> 100\,\mathrm{ns}$ and Doppler $> 0\,\mathrm{kHz}$ correspond to other scatterers. The delay-Doppler ANM estimates in Doppler domain for all shown μ' suffer from a leakage effect similar to the leakage effect from spectral analysis for strong LOS. ANM identifies only one additional scatterer to the LOS. At recording time t_2, less LSF peaks are in the neighborhood corresponding to the LOS with moderate power. ANM identifies now more scatterers for $\mu' = 0.5\mu_e$ and $\mu' = \mu_e$ additional to the LOS, where delay-Doppler estimates still suffer mildly from the leakage effect. For high

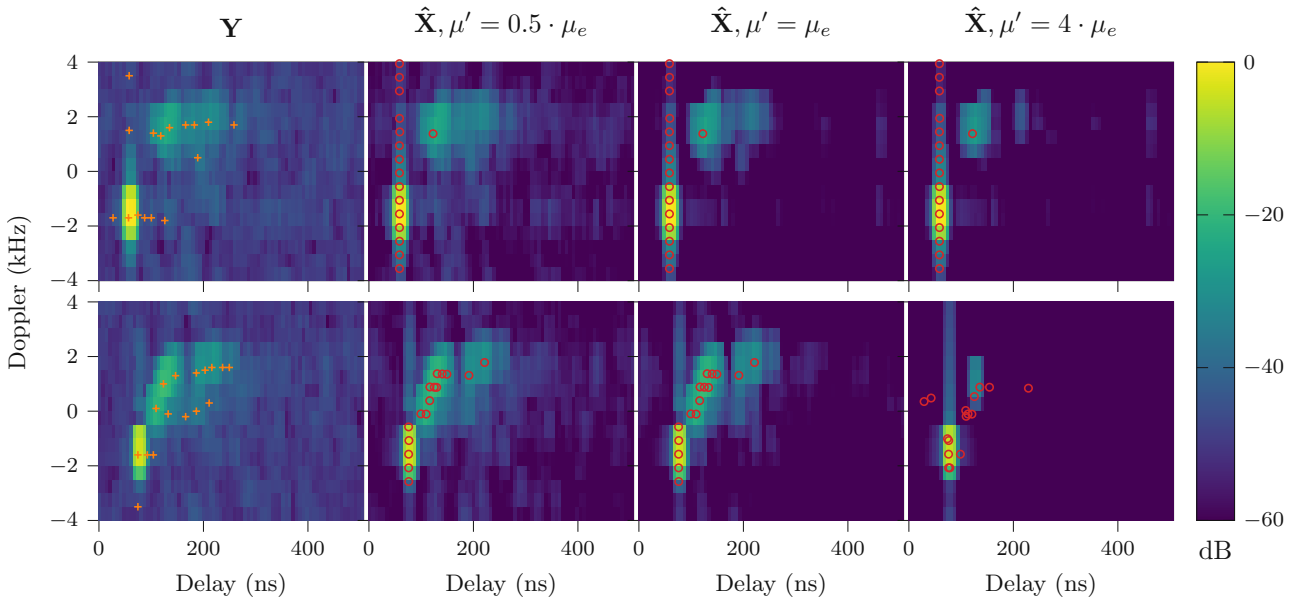

Figure 6.10: Identified scatterer with atomic norm minimization (ANM) for time-frequency limited measurement data. The S largest peaks (+) of the local scattering function (LSF) $\hat{\mathcal{C}}[l', k'; t_b]$ eq. (5.1). Recovered delay-Doppler pairs (o) with ANM eq. (6.11) applied to the sample matrix $\mathbf{Y}$ eq. (3.10) for different μ' followed by Matrix pencil and auto-pairing (MAPP). The number of pairs is limited to $S = 16$. $\mathbf{Y}$ has $N_\nu = 16$ snapshots in time and $N_\tau = 77$ samples in frequency centered around t_b and $f_c = 62.35\,\text{GHz}$, respectively. $T_{\text{obs}} = N_\nu T_{\text{R}} = 2\,\text{ms}$, $\Delta f = 2\,\text{MHz}$. Background colors are the LSFs $\hat{\mathcal{C}}[l', k'; t_b]$, normalized to maximum, with the samples from $\mathbf{Y}$, and ANM denoised matrix $\hat{\mathbf{X}}$, respectively. Top: $t_1 = 13.11\,\text{s}$, bottom: $t_2 = 13.75\,\text{s}$ recording time.

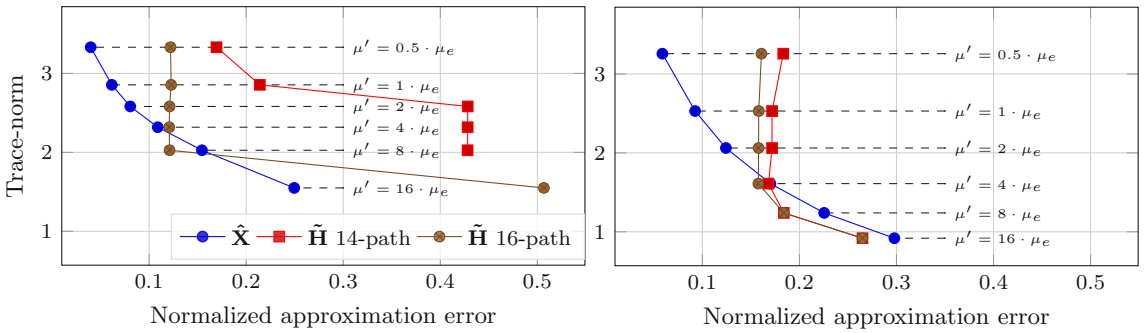

Figure 6.11: L-curve shows trade-off between sparsity with trace-norm $\mathrm{Tr}\,(\mathbf{T}_2(\mathbf{u}))\,/\,(N_\nu N_\tau)$ and normalized approximation error (NAE) eq. (6.23) of measurement reconstruction with atomic norm minimization (ANM) denoised $\hat{\mathbf{X}}$ or with a sparse representation $\tilde{\mathbf{H}}_{\mathrm{ANM}}$, each for different regularizer values μ'. The sparse channel consists of 14 or 16 paths maximum. Left: $t_1 = 13.11\,\mathrm{s}$, right: $t_2 = 13.75\,\mathrm{s}$ recording time.

$\mu' = 4\mu_e$, the ANM fails to identify most of the scatterers.

I now calculate an equivalent LSF with the samples of the time-frequency region described by the ANM denoised matrix $\hat{\mathbf{X}}$, for a description in the delay-Doppler domain. The background color in fig. 6.10 shows the LSFs $\hat{\mathcal{C}}[l', k'; t_b]$, which are calculated from the sample matrices $\mathbf{Y}$ and the denoised $\hat{\mathbf{X}}$, respectively. Increasing μ' shows an intensification of the denoising effect in the LSF, where the strong differences between the LSF from $\mathbf{Y}$ and the LSF from denoised $\hat{\mathbf{X}}$ at t_2 and at $\mu' = 4\mu_e$ coincides with failing identification of scatterers in the later.

Next, I evaluate the applicability of the sparse representation $\tilde{\mathbf{H}}$ eq. (6.22) on the sample matrix $\mathbf{Y}$ defined in eq. (3.10). I denote $\tilde{\mathbf{H}}$ with estimated parameters through ANM as $\tilde{\mathbf{H}}_{\mathrm{ANM}}$. The model order is unknown for the measurement data and estimation is limited to the previously set maximum value of 16. I show the approximation quality with $\mathrm{NAE}(\,\cdot\,;\mathbf{Y})$ eq. (6.23) for reconstructing $\mathbf{Y}$ with the sparse representation $\tilde{\mathbf{H}}_{\mathrm{ANM}}$ defined in eq. (6.22) with recovered parameters $\{\hat{c}_s, \hat{\tau}_s, \hat{\nu}_s \mid s = 1, \ldots, S\}$. The trade-off between sparsity and measurement reconstruction is shown in fig. 6.11 where the trace-norm is $\mathrm{Tr}\,(\mathbf{T}_2(\mathbf{u}))\,/(N_\nu N_\tau)$. The $\mathrm{NAE}(\hat{\mathbf{X}};\mathbf{Y})$ through the ANM denoised $\hat{\mathbf{X}}$ serves as a comparison.

$\mathrm{NAE}(\hat{\mathbf{X}};\mathbf{Y})$ decreases with decreasing μ' as the trace-norm has only insignificant weight for the objective function in eq. (6.11). $\mathrm{NAE}(\tilde{\mathbf{H}}_{\mathrm{ANM}};\mathbf{Y})$ through the estimate $\tilde{\mathbf{H}}_{\mathrm{ANM}}$ of the discrete MPCs model also decreases with decreasing μ', where $S = 16$ paths lead to $\mathrm{NAE} < 0.16$ in both cases for $\mu' = \mu_e$. For a further decrease of μ', $\mathrm{NAE}(\tilde{\mathbf{H}}_{\mathrm{ANM}};\mathbf{Y})$ saturates and does not decrease anymore. Reducing the number of paths to $S = 14$ paths slightly increases the error for t_2, but dramatically increases it for t_2 and thus leads to a bad approximation for t_1. Note that NAEs > 0.6 are not shown.

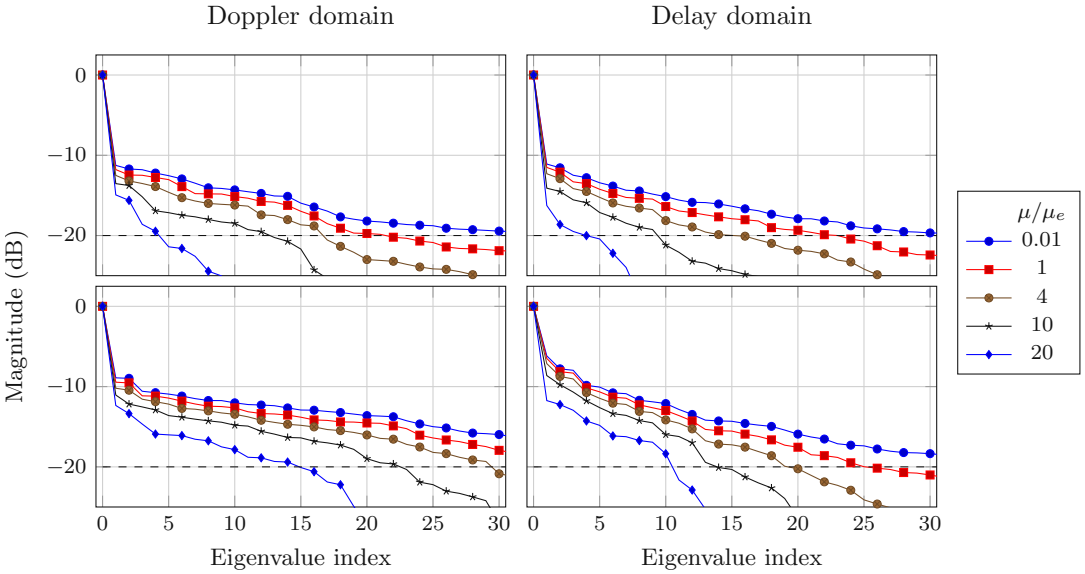

Figure 6.12: Decoupled case: Eigenvalues $\lambda(u_\nu)$ and $\lambda(u_\tau)$ of recovered Toeplitz matrices for different regularizer values μ. Top row: at 13.11 s, bottom row: at 13.75 s recording time. Left column: Doppler domain ($\mathbf{T}_1(\mathbf{u}_\nu)$) and right column: delay domain ($\mathbf{T}_1(\mathbf{u}_\tau)$). Threshold for pairing is at 20 dB. Normalized with first eigenvalue.

Measurement Evaluation with D-ANM

The ANM method eq. (6.11) is unpractical for large problem sizes. Therefore, I now analyze the previously selected time regions t_1 and t_2 at $f_c = 62.35\,\text{GHz}$ with D-ANM eq. (6.20) and are able to select a higher number of time-frequency samples. Here, a longer duration $N_\nu = 128$, i.e. $T_{\text{obs}} = 16\,\text{ms}$, and more subcarriers for similar bandwidth, $N_\tau = 155$, are taken from the measurement. First, I estimate parameters in delay domain and Doppler domain independently with a matrix pencil method from the recovered Toeplitz matrices $\mathbf{T}_1(\mathbf{u}_\tau)$ and $\mathbf{T}_1(\mathbf{u}_\nu)$, respectively.

Figure 6.12 shows the eigenvalues of the recovered Toeplitz matrices in the Doppler domain ($\mathbf{T}_1(\mathbf{u}_\nu)$) and in delay domain ($\mathbf{T}_1(\mathbf{u}_\tau)$) for different regularization parameter μ. As in the ANM case, with increasing μ, the SDP generates $\mathbf{T}_1(\mathbf{u}_\nu)$ and $\mathbf{T}_1(\mathbf{u}_\tau)$ with fewer eigenvalues each, where their magnitudes are close to the largest eigenvalue magnitude. The empirical values for μ according to eq. (6.12) are $\mu_e[t_1] = 20.76$ and $\mu_e[t_2] = 29$, where the noise power is estimated from the measurement. The number of estimated parameters S corresponds to the number of significant eigenvalues of the Toeplitz matrices. For further evaluation, I limit the number of parameters $S = S_\tau = S_\nu = \min(32, N_{\lambda(\nu)}, N_{\lambda(\tau)})$, where $N_{\lambda(\nu)}$ and $N_{\lambda(\tau)}$ are the number of significant eigenvalues of their respective Toeplitz matrices $\mathbf{T}_1(\mathbf{u}_\nu)$ and $\mathbf{T}_1(\mathbf{u}_\tau)$ with magnitudes not smaller than 20 dB from the largest eigenvalue each.

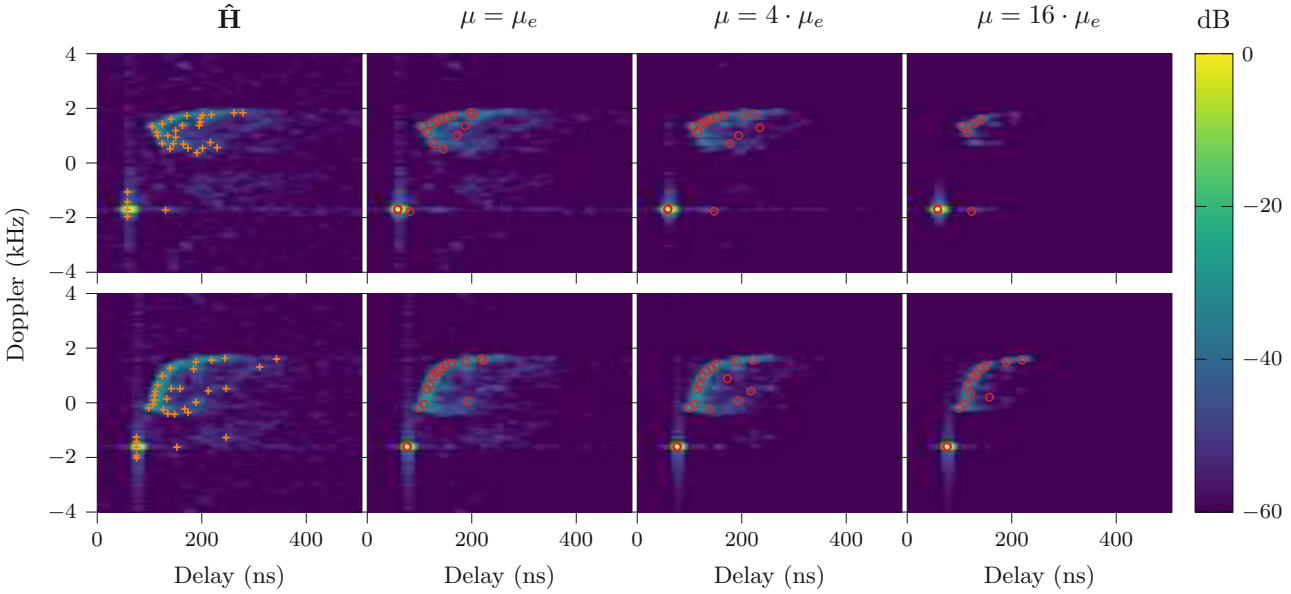

Figure 6.13: Identified scatterer with decoupled ANM (D-ANM) for time-frequency limited measurement data. The S largest peaks (+) of the local scattering function (LSF) $\hat{\mathcal{C}}[l', k'; t_b]$ eq. (5.1). Recovered delay-Doppler pairs (o) with D-ANM eq. (6.20) applied to the sample matrix $\mathbf{Y}$ eq. (3.10) for different μ followed by the matrix pencil method applied to the recovered two Toeplitz matrices and pairing approach similar to two-dimensional conventional beamformer. Only the 16 pairs of strongest magnitudes are shown. $\mathbf{Y}$ has $N_\nu = 128$ snapshots in time and $N_\tau = 155$ samples in frequency centered around t_b and $f_c = 62.35\,\text{GHz}$, respectively. $T_{\text{obs}} = N_\nu T_{\text{R}} = 16\,\text{ms}$, $\Delta f = 1\,\text{MHz}$. Unambiguous delay $500\,\text{ns} \leq \tau < 1\,\mu\text{s}$ not shown for better visual comparison with fig. 6.10. Background colors are the LSFs $\hat{\mathcal{C}}[l', k'; t_b]$, normalized to maximum, with the samples from $\mathbf{Y}$, and D-ANM denoised matrix $\hat{\mathbf{X}}$, respectively. Top: $t_1 = 13.11\,\text{s}$, bottom: $t_2 = 13.75\,\text{s}$ recording time.

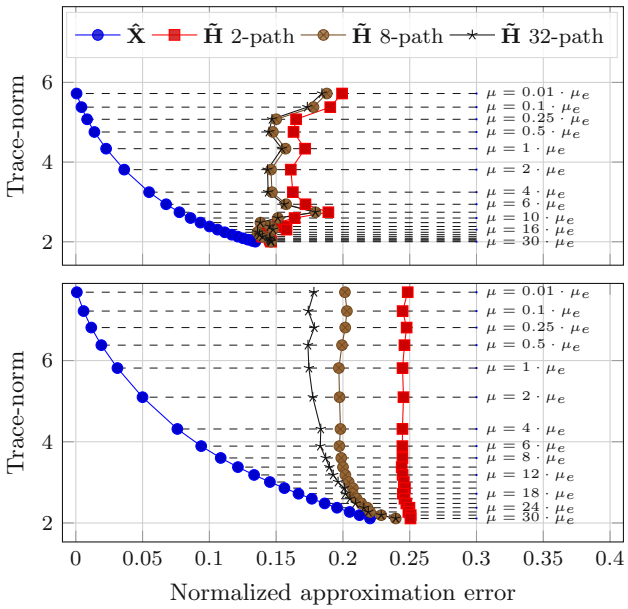

Figure 6.14: L-curve shows trade-off between sparsity with trace-norm $\left[\mathrm{Tr}\left(\mathbf{T}_1(\mathbf{u}_\tau)\right) + \mathrm{Tr}\left(\mathbf{T}_1(\mathbf{u}_\nu)\right)\right]/\sqrt{N_\nu N_\tau}$ and normalized approximation error (NAE) eq. (6.23) of measurement reconstruction with decoupled ANM (D-ANM) denoised $\hat{\mathbf{X}}$ or with a sparse representation $\tilde{\mathbf{H}}_{\mathrm{DANM}}$, each for different regularizer values μ. The sparse channel consists of 2,8, or 32 paths maximum. Top: $t_1 = 13.11\,\mathrm{s}$, bottom: $t_2 = 13.75\,\mathrm{s}$ recording time.

I pair the separate parameter estimates (see section 6.1.5) and get S delay-Doppler pairs $(\hat{\tau}_i, \hat{\nu}_s)$ as shown in fig. 6.13. A choice of lower μ leads to more significant eigenvalues and thus more detected delay-Doppler pairs. However, those pairs do not correspond to the peaks of the LSF in fig. 6.13. The estimates from D-ANM in fig. 6.13 do not severely suffer from the leakage effect as in the ANM case. The background color in fig. 6.13 shows the LSFs $\hat{\mathcal{C}}[l', k'; t_b]$, which are calculated from the sample matrices $\mathbf{Y}$ and the D-ANM denoised $\hat{\mathbf{X}}$, respectively. At increased μ, denoising reduces the number of visible peaks of the LSF and the number of delay-Doppler pairs also decreases.
Next, I evaluate the applicability of the sparse representation $\tilde{\mathbf{H}}$ eq. (6.22) on the sample matrix $\mathbf{Y}$ defined in eq. (3.10). I denote $\tilde{\mathbf{H}}$ with estimated parameters through D-ANM as $\tilde{\mathbf{H}}_{\mathrm{DANM}}$. I vary the number of paths up to S and calculate $\mathrm{NAE}(\tilde{\mathbf{H}}_{\mathrm{DANM}}; \mathbf{Y})$, in eq. (6.23), for reconstructing $\mathbf{Y}$ with a sparse representation $\tilde{\mathbf{H}}$ defined in eq. (6.22). The trade-off between sparsity and measurement reconstruction is shown in fig. 6.14 where the trace-norm is $\left[\mathrm{Tr}\left(\mathbf{T}_1(\mathbf{u}_\tau)\right) + \mathrm{Tr}\left(\mathbf{T}_1(\mathbf{u}_\nu)\right)\right]/\sqrt{N_\nu N_\tau}$. The $\mathrm{NAE}(\hat{\mathbf{X}}; \mathbf{Y})$ through the D-ANM denoised $\hat{\mathbf{X}}$ serves as a comparison. $\mathrm{NAE}(\hat{\mathbf{X}}; \mathbf{Y})$ decreases with decreasing μ as the trace-norm has only insignificant weight for the objective function as in the ANM case. $\mathrm{NAE}(\tilde{\mathbf{H}}_{\mathrm{DANM}}; \mathbf{Y})$ also decreases with decreasing μ. However, there is a saturation effect which differs strongly between the two time regions. For 8 paths and $\mu = \mu_e$,

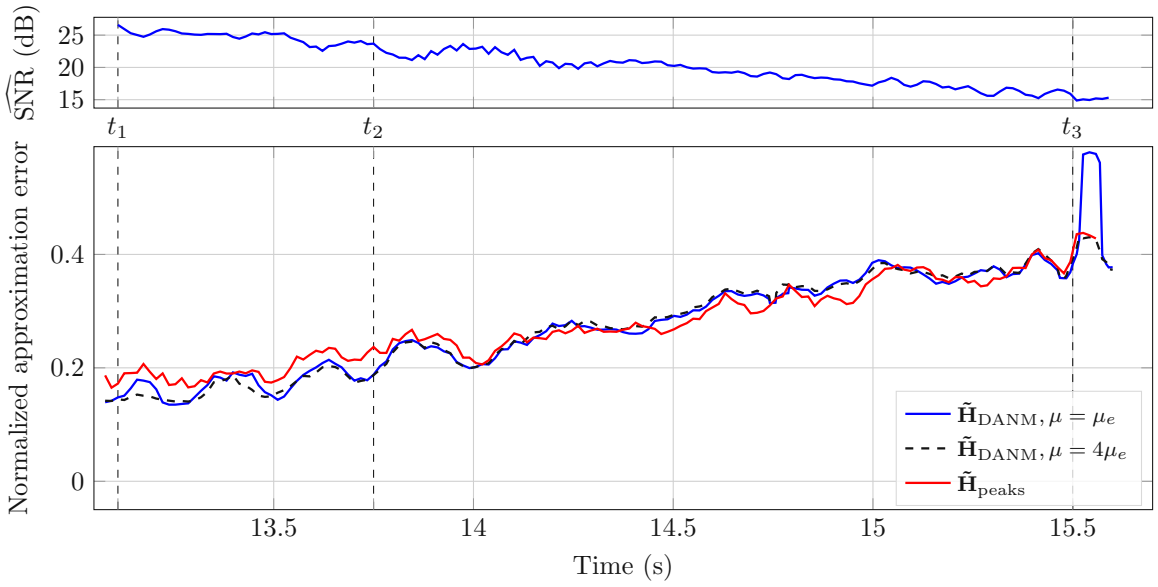

Figure 6.15: Normalized approximation error $\mathrm{NAE}(\tilde{\mathbf{H}}; \mathbf{Y})$ eq. (6.23) for approximating the sample matrix $\mathbf{Y}$ at $f_c = 62.35\,\mathrm{GHz}$ eq. (3.10) with sparse representations $\tilde{\mathbf{H}}$ eq. (6.22) from different parameter estimation techniques. $\tilde{\mathbf{H}}_{\mathrm{DANM}}$ is based on parameter estimates with decoupled ANM (D-ANM) eq. (6.20) with μ as the empirical μ_e eq. (6.12), and four times μ_e, limited to $S \leq 32$. $\tilde{\mathbf{H}}_{\mathrm{peaks}}$ is based on parameter estimates from the 32 largest peaks of the local scattering function eq. (5.1) with DFT oversampling by zero padding of a factor 5. The expectation in eq. (6.23) is taken over 64 ms (bottom). Estimated signal-to-noise ratio $\widehat{\mathrm{SNR}}$ (top).

$\mathrm{NAE} < 0.2$ in both cases.

I now analyze a larger part of the car's trajectory as shown in fig. 6.2. After the TX passed the RX, the separation in delay $\Delta\tau$ and in Doppler $\Delta\nu$ between the LOS component and several MPCs decreased significantly. The distances between the LOS component and the MPC with earliest arrival change from $\Delta\tau[t_1]$=43.7 ns and $\Delta\nu[t_1]$=3.6 kHz (fig. 6.4(a)) to $\Delta\tau[t_2]$=22.2 ns and $\Delta\nu[t_2]$=1.43 kHz (fig. 6.4(b)). Further, the estimated signal-to-noise ratio $\widehat{\mathrm{SNR}} = 10\log_{10}\left(\|\mathbf{Y}\|_F^2 / \left(N_\tau N_\nu \hat{\sigma}_Z^2\right) - 1\right)$ decreased, see fig. 6.15. I employ the NAE to compare $\tilde{\mathbf{H}}_{\mathrm{DANM}}$ from estimated parameters with the sample matrix $\mathbf{Y}$ for different recording times t_b. NAE depends further on the number of paths utilized for the sparse representation $\tilde{\mathbf{H}}_{\mathrm{DANM}}$. Figure 6.15 shows the $\mathrm{NAE}(\tilde{\mathbf{H}}_{\mathrm{DANM}}; \mathbf{Y})$ over time at fixed $\frac{\mu}{\mu_e}$ ratios, where the number of paths of the sparse representation is limited to 32. Although lower μ lead to more detected paths compared to cases with higher μ, NAE does not necessarily decrease accordingly. At $\mu = \mu_e$ and $\mu = 4 \cdot \mu_e$, the detected paths show an $\mathrm{NAE}(\tilde{\mathbf{H}}_{\mathrm{DANM}}; \mathbf{Y}) < 0.15$ at t_1, $\mathrm{NAE}(\tilde{\mathbf{H}}_{\mathrm{DANM}}; \mathbf{Y}) < 0.2$ at t_2, and the approximation is sustainable for recording time larger than 14 s.

As an alternative method I denote $\tilde{\mathbf{H}}$ with estimated parameters using the largest peaks of the multitaper spectral estimator eq. (5.1) as $\tilde{\mathbf{H}}_{\text{peaks}}$. I employ separable windows $D_i[k,l] = u_i[k]v_i[l]$ where $u_i[k]$ and $v_i[l]$ are time and frequency windows, respectively [91], [130]. I need high spectral resolution of the largest peak positions and select the first Slepian sequence [159] with $NW_\text{t} = 1.5$ as time window $u_i[k]$ and the first Slepian sequence with $NW_\text{f} = 1.5$ as frequency window $v_i[l]$, where NW_t and NW_f are the normalized time $\times$ half bandwidth products of the employed spectral windows in time and frequency, respectively. This leads to a single time-frequency window. Note, that I employ a lower number of windows in each domain than the empirical maximum $\lfloor 2NW_\text{t} \rfloor - 1$, $\lfloor 2NW_\text{f} \rfloor - 1$ respectively, to combat leakage [85, Ch. 8.2]. The spectral resolution reduces to $R_\tau = 2NW_\text{f}\Delta\tau = 19.3\,\text{ns}$ in delay and $R_\nu = 2NW_\text{t}\Delta\nu = 187.5\,\text{Hz}$ in Doppler due to the employed windows. Estimating LSF with additional DFT oversampling by zero padding allows a finer grid of the peak positions of each spectral main lobe in delay and Doppler. A trivial two-dimensional peak search selects the S largest peaks of the LSF and thus determines the paths and parameters for the sparse representation $\tilde{\mathbf{H}}_{\text{peaks}}$. The $\text{NAE}(\tilde{\mathbf{H}}_{\text{peaks}}; \mathbf{Y})$ is slightly higher than the sparse representations based on D-ANM for recording time smaller than 14 s, where $\widehat{\text{SNR}} > 20\,\text{dB}$. Overall, $\text{NAE}(\tilde{\mathbf{H}}_{\text{peaks}}; \mathbf{Y})$ is close to the D-ANM case for larger recording time.

For further statistical evaluation of the LSF, derived by the measurement or by the sparse representations, I allow lower resolution for estimator of the LSF to achieve lower variance. I select two Slepian sequences with $NW_\text{t} = 2$ as time windows $u_i[k]$ and the first two Slepian sequences with $NW_\text{f} = 2.5$ as frequency windows $v_i[l]$. This leads to a total number of $I = 4$ orthogonal windows, which is again lower than the empirical maximum to combat leakage. The spectral resolution reduces further to $R_\tau = 2NW_\text{f}\Delta\tau = 32.2\,\text{ns}$ in delay and $R_\nu = 2NW_\text{t}\Delta\nu = 250\,\text{Hz}$ in Doppler due to the employed windows. Prior to the calculation of the moments, thresholding is applied to the delay eq. (5.3) and Doppler power profiles eq. (5.4) to exclude values 30 dB lower than the peak power or values lower than 5 dB above the estimated noise power of the corresponding delay or Doppler power profiles.

Figure 6.16(a)–(d) show the first and second central moments in delay and Doppler domain of the LSF of the measurement data along the car's trajectory and their sparse representations $\tilde{\mathbf{H}}_{\text{DANM}}$ and $\tilde{\mathbf{H}}_{\text{peaks}}$.

The filled areas for $\tilde{\mathbf{H}}_{\text{DANM}}$ and $\tilde{\mathbf{H}}_{\text{peaks}}$ show the moments when the number of paths is varied between a single path to a maximum of 32 paths, if detected. The mean delays in fig. 6.16(a) and mean Doppler shifts in fig. 6.16(c) follow closely the first moments of the LSF of the measurement data. With only a single path for $\tilde{\mathbf{H}}_{\text{DANM}}$ and $\tilde{\mathbf{H}}_{\text{peaks}}$, mean delay and mean Doppler most likely coincide with delay and Doppler shift of the dominant LOS component. For $\tilde{\mathbf{H}}_{\text{peaks}}$ with a single path, mean delay and mean Doppler are step functions due to the employed delay-Doppler grid for calculating the LSF eq. (5.1).

The RMS delay spreads in fig. 6.16(b) and RMS Doppler shift spreads in fig. 6.16(d)

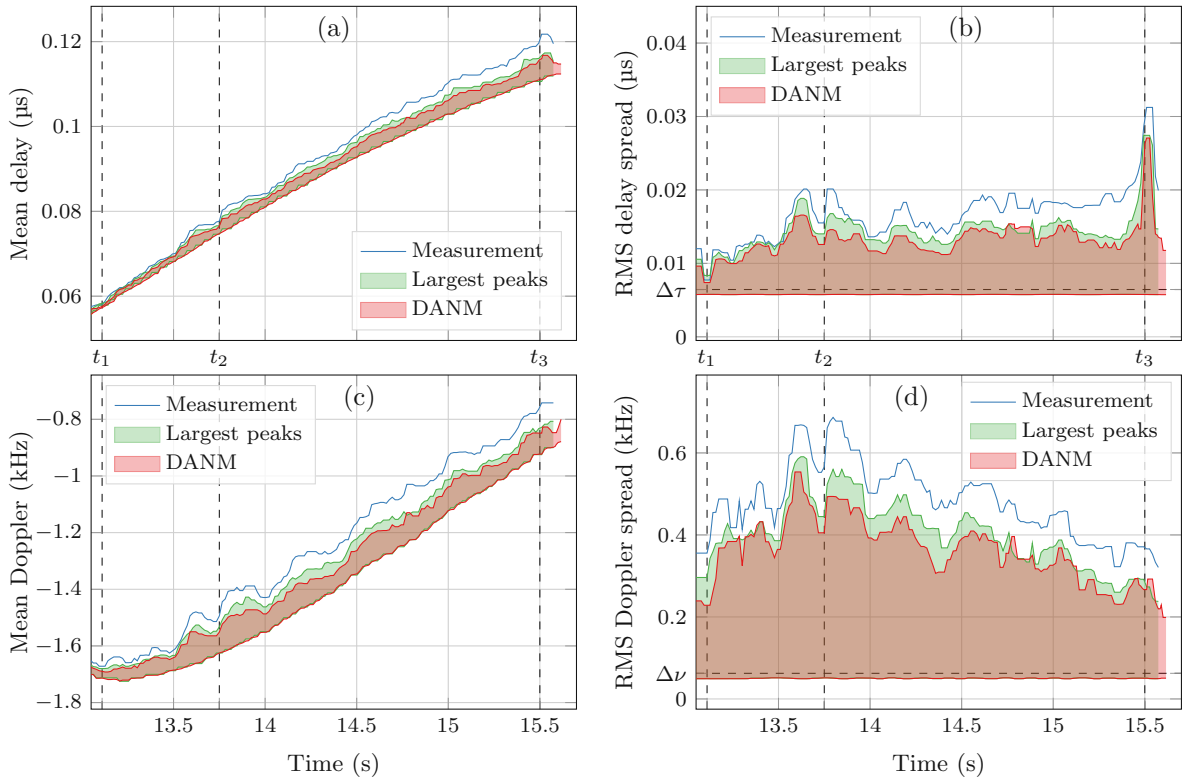

Figure 6.16: First and second central moments vs. time: local scattering function (LSF) estimate eq. (5.1) from measured data at $f_c = 62.35\,\text{GHz}$, LSF of sparse representation $\tilde{\mathbf{H}}_{\text{peaks}}$ by selecting the S largest peaks of the LSF of sample matrix $\mathbf{Y}$, and LSF of $\tilde{\mathbf{H}}_{\text{DANM}}$ based on decoupled ANM (D-ANM) estimates eq. (6.20) with $\mu = \mu_e$. First moments are (a) mean delay and (c) mean Doppler shift. Second central moments are (b) RMS delay spread and (d) RMS Doppler spread. The sparse representations $\tilde{\mathbf{H}}_{\text{peaks}}$ and $\tilde{\mathbf{H}}_{\text{DANM}}$ eq. (6.22) have a varying limit of paths $S = 1, \ldots, 32$, where the actual number for $\tilde{\mathbf{H}}_{\text{peaks}}$ is always S and can be lower for $\tilde{\mathbf{H}}_{\text{DANM}}$. A median filter of 80 ms is applied in time.

depend heavily on the number of paths where for the maximum number of paths, there is only a slight deviation to the LSF of the measurement data. Despite lower spreads in fig. 6.16(b) and fig. 6.16(d) for the D-ANM case compared to the measurement data, their trends follow the measurement data closely and nearly as good as $\tilde{\mathbf{H}}_{\text{peaks}}$. With only a single path for $\tilde{\mathbf{H}}_{\text{DANM}}$ and $\tilde{\mathbf{H}}_{\text{peaks}}$, the spreads reduce to a residual value close to the delay resolution $\Delta\tau$ and Doppler resolution $\Delta\nu$, respectively.

6.5 Discussion

In this chapter, I have showed a method to identify scatterers with atomic norm minimization (ANM) techniques in the delay-Doppler domain for V2I mm-wave communications channels. The ANM framework is an interesting method, which employs semidefinite programming for gridless parameter estimation. However, a rather restrictive minimum separation condition and high computational complexity prevent a wide application of the described method, e.g. on realistic data. In the investigated V2I mm-wave scenario, solving the optimization problem of the vectorized two-dimensional ANM method is only tractable with a sample size, which is insufficient for scatterer identification. Furthermore, effects which are similar to spectral leakage of spectral methods are present for the vectorized two-dimensional ANM. The decoupled ANM provides a reduction in complexity to solve the corresponding optimization problem with larger sample size. The actual scatterers' parameters are recovered from two Toeplitz matrices with a matrix pencil and auto-pairing method to achieve good accuracy.
Both methods employ a regularization parameter for tuning to find a trade-off between sparsity and quality of reconstruction. I treat this regularizer in an extrinsic way and gear its values to empirical results. A more adaptive treatment of the regularizer, e.g. through data cross-validation and iteratively optimization, is out of scope of this thesis.

7 Conclusion and Outlook

I conclude with remarks on channel variability, sparsity in delay-Doppler domain, and scatterer identification with sparse methods.

V2I Channel Variability. The wireless channel fluctuates severely in the presence of multiple dominant specular components, which are not resolvable in delay. Even in the case of aligned beams between TX and RX, the variability of the channel is more severe than in the ideal Rician fading case due to the presence of sidelobes and specular components from the vehicle and ground reflection.
The half power beamwidth of the employed antenna is too wide to significantly attenuate the MPC due to the ground path. Therefore, the ground path interferes with the LOS component if the channel bandwidth of the employed receiver is too low. Variability of the channel is lower for the TX with a 15° uptilt compared to a TX directed horizontally at 0°.

> **The V2I mm-wave channel can fluctuate severely due to interference despite aligned directional antennas and the availability of LOS components. Interfering dominant specular components are caused by too wide beamwidth of the main lobe, unwanted strong sidelobes, or insufficient channel bandwidth limiting frequency diversity.**
>
> **In the presence of dominant specular components, which cause large spatial fading periods, fitting parametric distributions to empirical CDFs from samples across the large spatial fading period results in unacceptable approximations. A simplified three-wave with diffuse power fading model is able to describe the fading within small spatial regions as TWDP fading. The TWDP fading model provides a good fit for the investigated V2I mm-wave channel within small spatial regions.**

Sparsity in delay-Doppler domain. Since I consider the antennas as an integral part of the wireless channel, the limited dynamic range of the employed channel sounder does not severely degrade the measured RMS delay spread and RMS Doppler spread. Therefore, I conclude, the considered V2I mm-wave channel has low RMS spreads based on the measurement.

The 2D multitaper estimator provides an intuitive way of analyzing the MPCs of the wireless channel.

> **The analysis shows that the V2I mm-wave channel is sparse in the delay-Doppler domain. Vehicles with large reflective surfaces are identifiable in the measured V2I mm-wave channels.**

> **The measured wireless channel with the beam directed horizontally contains more MPCs than the beam with a 15° uptilt.**

On the one hand, the variability is higher for 0° leading to worse fading conditions for the wireless system, on the other hand large objects provide additional propagation paths, as seen by highly available paths due to a passenger bus.

> **The high availability of additional paths in the V2I mm-wave scenario increases diversity in the delay-Doppler domain of a wireless system.**

Scatterer Identification with sparse methods. I show an identification method of sparse scatterers with ANM techniques in the delay-Doppler domain for V2I mm-wave communications. The decoupled ANM together with a matrix pencil method allows for estimation with larger sample size, required for the envisioned V2I mm-wave parameters, than ANM for adequately modeling of the sparse channel.
I investigated the error of the approximation of a cluster of point-scatterers model through the sparse model with respect to the cluster spread. I verified through simulation, that small cluster spreads lead to acceptable estimation accuracy for delay and Doppler parameters. The analysis of the V2I mm-wave measurement data shows high agreement between identified scatterers through the decoupled ANM and scatterers from the LSF in terms of approximation quality. Furthermore, the identified scatters accurately model the well-known time-variant channel properties, e.g. mean delay, RMS delay spread, mean Doppler, and RMS Doppler spread.

> **The low approximation error between the measured channels and their sparse representations shows that this is an adequate model for the investigated scenario. Therefore, a hybrid deterministic and random channel model for V2I mm-wave scenarios is more adequate than a purely random channel model.**

Open Questions

Compared to vehicular sub-6 GHz wireless communications, the available delay resolution in the mm-wave bands enables treating selected aspects of the wireless channel as

deterministic. The knowledge of the position of large vehicles and their trajectory may provide channel capacity gains or increase reliability of the wireless system.
Future research on V2I mm-wave wireless channels should take this deterministic part of a hybrid deterministic and random channel into account.
The presented ANM method might be unsuitable for online identification of scatterers with state-of-the-art signal processing hardware. However, identifying scatterers can be of use also in offline situations, e.g. when a map of scatterers needs to be updated, and provide prior knowledge about the deterministic part of a hybrid channel model. The required frequency of updates for positions of static IOs in an urban street environment is currently unknown and open for research.

List of Figures

List of Tables

Bibliography

[1] C. T. et al., „ETSI technology radar“, ETSI, Tech. Rep. 1, Apr. 2021, ETSI White Paper No. 45, ISBN 979-10-92620-39-1.

[2] H. Tataria, M. Shafi, A. F. Molisch, M. Dohler, H. Sjoland, and F. Tufvesson, „6G wireless systems: Vision, requirements, challenges, insights, and opportunities“, *Proceedings of the IEEE*, vol. 109, no. 7, pp. 1166–1199, 2021. DOI: 10.1109/jproc.2021.3061701.

[3] S. Salous, *Radio Propagation Measurement and Channel Modelling*. John Wiley & Sons, Ltd, 2013, ISBN: 9781118502280. DOI: 10.1002/9781118502280.

[4] S. Salous, V. D. Esposti, F. Fuschini, *et al.*, „Millimeter-wave propagation: Characterization and modeling toward fifth-generation systems“, *IEEE Antennas Propag. Mag.*, vol. 58, no. 6, pp. 115–127, 2016. DOI: 10.1109/map.2016.2609815.

[5] R. He, B. Ai, G. Wang, M. Yang, C. Huang, and Z. Zhong, „Wireless channel sparsity: Measurement, analysis, and exploitation in estimation“, *IEEE Wireless Communications*, vol. 28, no. 4, pp. 113–119, 2021. DOI: 10.1109/mwc.001.2000378.

[6] A. F. Molisch, T. Choi, N. Abbasi, F. Rottenberg, and J. Zhang, „Millimeter-wave channels“, in *Wiley 5G Ref*. John Wiley & Sons, Ltd, 2021, pp. 1–46, ISBN: 9781119471509. DOI: https://doi.org/10.1002/9781119471509.w5GRef042.

[7] I. A. Hemadeh, K. Satyanarayana, M. El-Hajjar, and L. Hanzo, „Millimeter-wave communications: Physical channel models, design considerations, antenna constructions, and link-budget“, *IEEE Communications Surveys & Tutorials*, vol. 20, no. 2, pp. 870–913, 2018. DOI: 10.1109/comst.2017.2783541.

[8] H. Groll, E. Zöchmann, S. Pratschner, *et al.*, „Sparsity in the delay-Doppler domain for measured 60 GHz vehicle-to-infrastructure communication channels“, in *2019 IEEE International Conference on Communications Workshops (ICC Workshops)*, May 2019. DOI: 10.1109/iccw.2019.8756930.

[9] M. Hofer, D. Löschenbrand, J. Blumenstein, *et al.*, „Wireless vehicular multiband measurements in centimeterwave and millimeterwave bands“, in *2021 IEEE 32nd Annual International Symposium on Personal, Indoor and Mobile Radio Communications (PIMRC)*, Helsinki, Finland, Sep. 2021. DOI: 10.1109/PIMRC50174.2021.9569547.

[10] R. He, O. Renaudin, V.-M. Kolmonen, *et al.*, „Characterization of quasi-stationarity regions for vehicle-to-vehicle radio channels“, *IEEE Transactions on Antennas and Propagation*, vol. 63, no. 5, pp. 2237–2251, 2015. DOI: 10.1109/TAP.2015.2402291.

[11] L. Bernado, T. Zemen, F. Tufvesson, A. F. Molisch, and C. F. Mecklenbräuker, „Delay and Doppler spreads of nonstationary vehicular channels for safety-relevant scenarios“, *IEEE Transactions on Vehicular Technology*, vol. 63, no. 1, pp. 82–93, 2014. DOI: 10.1109/tvt.2013.2271956.

[12] C. F. Mecklenbräuker, A. F. Molisch, J. Karedal, *et al.*, „Vehicular channel characterization and its implications for wireless system design and performance“, *Proceedings of the IEEE*, vol. 99, no. 7, pp. 1189–1212, 2011. DOI: 10.1109/jproc.2010.2101990.

[13] H. Meinel and A. Plattner, „Millimetre-wave propagation along railway lines“, *IEE Proceedings F (Communications, Radar and Signal Processing)*, vol. 130, no. 7, pp. 688–694, 1983. DOI: 10.1049/ip-f-1.1983.0102.

[14] A. Kato, K. Sato, M. Fujise, and S. Kawakami, „Propagation characteristics of 60-GHz millimeter waves for ITS inter-vehicle communications“, *IEICE Trans. Commun.*, vol. 84, no. 9, pp. 2530–2539, Sep. 2001, ISSN: 09168516.

[15] L. Cheng, B. Henty, D. Stancil, F. Bai, and P. Mudalige, „Mobile vehicle-to-vehicle narrow-band channel measurement and characterization of the 5.9 GHz dedicated short range communication (DSRC) frequency band“, *IEEE Journal on Selected Areas in Communications*, vol. 25, no. 8, pp. 1501–1516, 2007. DOI: 10.1109/jsac.2007.071002.

[16] O. Renaudin, V.-M. Kolmonen, P. Vainikainen, and C. Oestges, „Wideband MIMO car-to-car radio channel measurements at 5.3 GHz“, in *2008 IEEE 68th Vehicular Technology Conference*, Sep. 2008, pp. 1–5. DOI: 10.1109/vetecf.2008.65.

[17] A. Paier, J. Karedal, N. Czink, *et al.*, „Characterization of vehicle-to-vehicle radio channels from measurements at 5.2 GHz“, *Wireless Personal Communications*, vol. 50, no. 1, pp. 19–32, 2008. DOI: 10.1007/s11277-008-9546-6.

[18] L. Bernado, T. Zemen, F. Tufvesson, A. F. Molisch, and C. F. Mecklenbräuker, „The (in-) validity of the WSSUS assumption in vehicular radio channels“, in *2012 IEEE 23rd International Symposium on Personal, Indoor and Mobile Radio Communications - (PIMRC)*, Sep. 2012, pp. 1757–1762. DOI: 10.1109/pimrc.2012.6362634.

[19] M. G. Sánchez, M. P. Táboas, and E. L. Cid, „Millimeter wave radio channel characterization for 5G vehicle-to-vehicle communications“, *Measurement*, vol. 95, pp. 223–229, Jan. 2017. DOI: 10.1016/j.measurement.2016.10.018.

[20] E. Zöchmann, C. Mecklenbräuker, M. Lerch, *et al.*, „Measured delay and Doppler profiles of overtaking vehicles at 60 GHz“, in *12th European Conference on Antennas and Propagation (EuCAP 2018)*, Apr. 2018. DOI: 10.1049/cp.2018.0470.

[21] J. Blumenstein, A. Prokes, J. Vychodil, *et al.*, „Measured high-resolution power-delay profiles of nonstationary vehicular millimeter wave channels“, in *2018 IEEE 29th Annual International Symposium on Personal, Indoor and Mobile Radio Communications (PIMRC)*, Sep. 2018. DOI: 10.1109/pimrc.2018.8580949.

[22] E. Zöchmann, M. Hofer, M. Lerch, *et al.*, „Statistical evaluation of delay and Doppler spread in 60 GHz vehicle-to-vehicle channels during overtaking“, in *2018 IEEE-APS Topical Conference on Antennas and Propagation in Wireless Communications (APWC)*, Sep. 2018. DOI: 10.1109/apwc.2018.8503750.

[23] E. Zöchmann, M. Hofer, M. Lerch, *et al.*, „Position-specific statistics of 60 GHz vehicular channels during overtaking“, *IEEE Access*, vol. 7, pp. 14 216–14 232, 2019. DOI: 10.1109/access.2019.2893136.

[24] A. Prokes, J. Vychodil, T. Mikulasek, *et al.*, „Time-domain broadband 60 GHz channel sounder for vehicle-to-vehicle channel measurement“, in *2018 IEEE Vehicular Networking Conference (VNC)*, Dec. 2018. DOI: 10.1109/vnc.2018.8628344.

[25] A. Prokes, J. Vychodil, M. Pospisil, J. Blumenstein, T. Mikulasek, and A. Chandra, „Time-domain nonstationary intra-car channel measurement in 60 GHz band“, in *Proc. of the International Conference on Advanced Technologies for Communications (ATC)*, 2016.

[26] J. Blumenstein, A. Prokes, J. Vychodil, M. Pospisil, and T. Mikulasek, „Time-varying K factor of the mm-wave vehicular channel: Velocity, vibrations and the road quality influence“, in *2017 IEEE 28th Annual International Symposium on Personal, Indoor, and Mobile Radio Communications (PIMRC)*, Oct. 2017, pp. 1–5. DOI: 10.1109/pimrc.2017.8292755.

[27] A. M. Sayeed and V. Raghavan, „Maximizing MIMO capacity in sparse multipath with reconfigurable antenna arrays“, *IEEE Journal of Selected Topics in Signal Processing*, vol. 1, no. 1, pp. 156–166, 2007. DOI: 10.1109/jstsp.2007.897057.

[28] C. Gustafson, K. Haneda, S. Wyne, and F. Tufvesson, „On mm-wave multipath clustering and channel modeling“, *IEEE Transactions on Antennas and Propagation*, vol. 62, no. 3, pp. 1445–1455, 2014. DOI: 10.1109/tap.2013.2295836.

[29] E. Zöchmann, S. Caban, C. F. Mecklenbräuker, *et al.*, „Better than rician: Modelling millimetre wave channels as two-wave with diffuse power“, *EURASIP Journal on Wireless Communications and Networking*, vol. 2019, 2019, Article number 21, 17 pages. DOI: 10.1186/s13638-018-1336-6.

[30] D. Dupleich, R. Muller, C. Schneider, *et al.*, „Multi-band vehicle to vehicle channel measurements from 6 GHz to 60 GHz at "T" intersection“, in *2019 IEEE 2nd Connected and Automated Vehicles Symposium (CAVS)*, Sep. 2019, pp. 1–5. DOI: 10.1109/cavs.2019.8887794.

[31] A. Loch, A. Asadi, G. H. Sim, J. Widmer, and M. Hollick, „Mm-wave on wheels: Practical 60 GHz vehicular communication without beam training“, in *2017 9th International Conference on Communication Systems and Networks (COMSNETS)*, Jan. 2017, pp. 1–8. DOI: 10.1109/comsnets.2017.7945351.

[32] J.-J. Park, J. Lee, K.-W. Kim, M.-D. Kim, and K. C. Lee, „Multipath propagation characteristics for 5G vehicular communications based on 28 GHz expressway measurements“, in *2019 13th European Conference on Antennas and Propagation (EuCAP)*, 2019, pp. 1–5.

[33] J.-J. Park, J. Lee, K.-W. Kim, M.-D. Kim, H.-K. Kwon, and K. C. Lee, „Wide-sense stationarity of millimeter wave expressway channels based on 28 GHz measurements“, in *2019 IEEE 90th Vehicular Technology Conference (VTC2019-Fall)*, Sep. 2019. DOI: 10.1109/vtcfall.2019.8891220.

[34] H. Wang, X. Yin, X. Cai, H. Wang, Z. Yu, and J. Lee, „Fading characterization of 73 GHz millimeter-wave V2V channel based on real measurements“, in *Communication Technologies for Vehicles*, Springer International Publishing, 2018, pp. 159–168. DOI: 10.1007/978-3-319-90371-2_16.

[35] J.-J. Park, J. Lee, K.-W. Kim, K.-C. Lee, and M.-D. Kim, „Vehicle antenna position dependent path loss for millimeter-wave V2V communication“, in *2018 11th Global Symposium on Millimeter Waves (GSMM)*, May 2018, pp. 1–3. DOI: 10.1109/gsmm.2018.8439480.

[36] C. Ballesteros, L. Montero, G. A. Ramírez, and L. Jofre-Roca, „Multi-antenna 3D pattern design for millimeter-wave vehicular communications“, *Vehicular Communications*, vol. 35, p. 100 473, 2022. DOI: 10.1016/j.vehcom.2022.100473.

[37] G. Ciaramitaro, M. Brambilla, D. Tagliaferri, *et al.*, „On the impact of road roughness and antenna position on vehicular communications“, *IEEE Wireless Communications Letters*, vol. 11, no. 9, pp. 1875–1879, 2022. DOI: 10.1109/lwc.2022.3185054.

[38] A. M. H. Nasr and K. Sarabandi, „A low-cost millimeter-wave 5G V2X multi-beam dual-polarized windshield antenna“, *IEEE Open Journal of Antennas and Propagation*, vol. 3, pp. 1313–1323, 2022. DOI: 10.1109/ojap.2022.3224807.

[39] F. Kaltenberger, T. Zemen, and C. W. Überhuber, „Low-complexity geometry-based MIMO channel simulation“, *EURASIP Journal on Advances in Signal Processing*, 2007, Article ID 95281, 17 pages. DOI: 10.1155/2007/95281.

[40] R. He, C. Schneider, B. Ai, *et al.*, „Propagation channels of 5G millimeter-wave vehicle-to-vehicle communications: Recent advances and future challenges“, *IEEE Vehicular Technology Magazine*, vol. 15, no. 1, pp. 16–26, 2020. DOI: 10.1109/mvt.2019.2928898.

[41] W. Li and J. C. Preisig, „Estimation of rapidly time-varying sparse channels“, *IEEE Journal of Oceanic Engineering*, vol. 32, no. 4, pp. 927–939, 2007. DOI: 10.1109/joe.2007.906409.

[42] K. Venugopal, A. Alkhateeb, N. G. Prelcic, and R. W. Heath, „Channel estimation for hybrid architecture-based wideband millimeter wave systems“, *IEEE Journal on Selected Areas in Communications*, vol. 35, no. 9, pp. 1996–2009, 2017. DOI: 10.1109/jsac.2017.2720856.

[43] B. N. Bhaskar, G. Tang, and B. Recht, „Atomic norm denoising with applications to line spectral estimation“, *IEEE Transactions on Signal Processing*, vol. 61, no. 23, pp. 5987–5999, 2013. DOI: 10.1109/tsp.2013.2273443.

[44] C. F. Mecklenbräuker, P. Gerstoft, and E. Ollila, „DOA M-estimation using sparse Bayesian learning“, in *Proc. IEEE Acoust., Speech and Signal Process. (ICASSP)*, Singapore, May 2022, pp. 4933–4937. DOI: 10.1109/icassp43922.2022.9746740.

[45] K. P. Murphy, *Machine Learning – A Probabilistic Perspective*. Cambridge (USA) and London (UK): MIT Press, 2012, ISBN: 978-0-262-01802-9.

[46] R. Prasad, C. R. Murthy, and B. D. Rao, „Joint approximately sparse channel estimation and data detection in OFDM systems using sparse Bayesian learning“, *IEEE Transactions on Signal Processing*, vol. 62, no. 14, pp. 3591–3603, 2014. DOI: 10.1109/tsp.2014.2329272.

[47] P. Gerstoft, C. F. Mecklenbrauker, A. Xenaki, and S. Nannuru, „Multisnapshot sparse Bayesian learning for DOA“, *IEEE Signal Processing Letters*, vol. 23, no. 10, pp. 1469–1473, 2016. DOI: 10.1109/lsp.2016.2598550.

[48] H. Groll, C. Mecklenbräuker, and P. Gerstoft, „Sparse Bayesian learning for directions of arrival on an FPGA“, in *2018 IEEE Statistical Signal Processing Workshop (SSP)*, Jun. 2018. DOI: 10.1109/ssp.2018.8450684.

[49] G. Tauböck, F. Hlawatsch, D. Eiwen, and H. Rauhut, „Compressive estimation of doubly selective channels in multicarrier systems: Leakage effects and sparsity-enhancing processing“, *IEEE Journal of Selected Topics in Signal Processing*, vol. 4, no. 2, pp. 255–271, 2010. DOI: 10.1109/JSTSP.2010.2042410.

[50] T. Blazek and C. F. Mecklenbräuker, „Sparse time-variant impulse response estimation for vehicular channels using the c-LASSO“, in *2017 IEEE 28th Annual International Symposium on Personal, Indoor, and Mobile Radio Communications (PIMRC)*, Oct. 2017. DOI: 10.1109/pimrc.2017.8292645.

[51] H. Zhang, R. He, B. Ai, S. Cui, and H. Zhang, „Measuring sparsity of wireless channels“, *IEEE Transactions on Cognitive Communications and Networking*, vol. 7, no. 1, pp. 133–144, 2021. DOI: 10.1109/tccn.2020.3013270.

[52] C. R. Berger, B. Demissie, J. Heckenbach, P. Willett, and S. Zhou, „Signal processing for passive radar using OFDM waveforms“, *IEEE Journal of Selected Topics in Signal Processing*, vol. 4, no. 1, pp. 226–238, 2010. DOI: 10.1109/jstsp.2009.2038977.

[53] F. Hlawatsch, *Wireless communications over rapidly time-varying channels*. London: Academic, 2011, ISBN: 9780123744838.

[54] R. Heckel, V. I. Morgenshtern, and M. Soltanolkotabi, „Super-resolution radar“, *Information and Inference*, vol. 5, no. 1, pp. 22–75, 2016. DOI: 10.1093/imaiai/iaw001.

[55] Y. Chi and M. F. D. Costa, „Harnessing sparsity over the continuum: Atomic norm minimization for superresolution“, *IEEE Signal Processing Magazine*, vol. 37, no. 2, pp. 39–57, 2020. DOI: 10.1109/msp.2019.2962209.

[56] R. Alieiev, T. Hehn, A. Kwoczek, and T. Kurner, „Predictive communication and its application to vehicular environments: Doppler-shift compensation“, *IEEE Transactions on Vehicular Technology*, vol. 67, no. 8, pp. 7380–7393, 2018. DOI: 10.1109/tvt.2018.2835662.

[57] G. Battistelli, L. Chisci, C. Fantacci, A. Farina, and A. Graziano, „Networked target tracking with Doppler sensors“, *IEEE Transactions on Aerospace and Electronic Systems*, vol. 51, no. 4, pp. 3294–3306, 2015. DOI: 10.1109/taes.2015.140340.

[58] E. Zöchmann, V. Va, M. Rupp, and R. W. Heath, „Geometric tracking of vehicular mmWave channels to enable machine learning of onboard sensors“, in *2018 IEEE Globecom Workshops (GC Wkshps)*, Dec. 2018. DOI: 10.1109/glocomw.2018.8644440.

[59] M. F. D. Costa and Y. Chi, „On the stable resolution limit of total variation regularization for spike deconvolution“, *IEEE Transactions on Information Theory*, vol. 66, no. 11, pp. 7237–7252, 2020. DOI: 10.1109/tit.2020.2993327.

[60] L. Zheng and X. Wang, „Super-resolution delay-Doppler estimation for OFDM passive radar“, *IEEE Transactions on Signal Processing*, vol. 65, no. 9, pp. 2197–2210, 2017. DOI: 10.1109/tsp.2017.2659650.

[61] H. L. Van Trees, *Optimum Array Processing*. John Wiley & Sons, Ltd, 2002, ISBN: 9780471093909. DOI: 10.1002/0471221104.

[62] A. Xenaki and P. Gerstoft, „Grid-free compressive beamforming“, *The Journal of the Acoustical Society of America*, vol. 137, no. 4, pp. 1923–1935, 2015. DOI: 10.1121/1.4916269.

[63] M. Wagner, Y. Park, and P. Gerstoft, „Gridless DOA estimation and root-MUSIC for non-uniform linear arrays“, *IEEE Transactions on Signal Processing*, vol. 69, pp. 2144–2157, 2021. DOI: 10.1109/tsp.2021.3068353.

[64] M. Wagner, H. Groll, A. Dormiani, V. Sathyanarayanan, C. F. Mecklenbräuker, and P. Gerstoft, „Phase coherent EM array measurements in a refractive environment“, *IEEE Transactions on Antennas and Propagation*, vol. 69, no. 10, pp. 6783–6796, 2021. DOI: 10.1109/tap.2021.3069516.

[65] J. Fuchs, M. Gardill, M. Lubke, A. Dubey, and F. Lurz, „A machine learning perspective on automotive radar direction of arrival estimation“, *IEEE Access*, vol. 10, pp. 6775–6797, 2022. DOI: 10.1109/access.2022.3141587.

[66] Y. Li, X. Wang, and Z. Ding, „Multi-target position and velocity estimation using OFDM communication signals“, *IEEE Transactions on Communications*, vol. 68, no. 2, pp. 1160–1174, 2020. DOI: 10.1109/tcomm.2019.2956928.

[67] H. Groll, E. Zöchmann, P. Gerstoft, and C. F. Mecklenbräuker, „Global robustness characterization of DOA estimators by breakdown detection“, in *2019 IEEE 8th International Workshop on Computational Advances in Multi-Sensor Adaptive Processing (CAMSAP)*, Dec. 2019. DOI: 10.1109/camsap45676.2019.9022468.

[68] P. Gerstoft, H. Groll, and C. F. Mecklenbräuker, „Parametric bootstrapping of array data with a generative adversarial network“, in *2020 IEEE 11th Sensor Array and Multichannel Signal Processing Workshop (SAM)*, Jun. 2020. DOI: 10.1109/sam48682.2020.9104371.

[69] H. Groll, D. Schützenhöfer, S. Pratschner, P. Gerstoft, and C. F. Mecklenbräuker, „Sparse approximation of an outdoor-to-indoor massive MIMO channel measurement“, in *2020 54rd Asilomar Conference on Signals, Systems, and Computers*, Nov. 2020, pp. 88–91. DOI: 10.1109/IEEECONF51394.2020.9443371.

[70] H. Groll, E. Zöchmann, S. Pratschner, *et al.*, „Scanning aperture antennas with spherical shells“, in *2019 International Conference on Electromagnetics in Advanced Applications (ICEAA)*, Sep. 2019. DOI: 10.1109/iceaa.2019.8879413.

[71] H. Groll, E. Zöchmann, M. Hofer, *et al.*, „60 GHz V2I channel variability for different elevation angle switching strategies“, in *2020 14th European Conference on Antennas and Propagation (EuCAP)*, Mar. 2020. DOI: 10.23919/eucap48036.2020.9135524.

[72] H. Groll, P. Gerstoft, M. Hofer, J. Blumenstein, T. Zemen, and C. F. Mecklenbräuker, „Scatterer identification by atomic norm minimization in vehicular mm-wave propagation channels“, *IEEE Access*, vol. 10, pp. 102 334–102 354, 2022. DOI: 10.1109/ACCESS.2022.3205616.

[73] D. Schutzenhofer, S. Pratschner, H. Groll, and M. Rupp, „Channel rank analysis of an outdoor-to-indoor massive MIMO measurement“, in *2020 IEEE 21st International Workshop on Signal Processing Advances in Wireless Communications (SPAWC)*, May 2020. DOI: 10.1109/spawc48557.2020.9154226.

[74] F. Pasic, S. Pratschner, R. Langwieser, *et al.*, „Sub 6 GHz versus mmWave measurements in a controlled high-mobility environment“, in *WSA 2021; 25th International ITG Workshop on Smart Antennas*, 2021, pp. 1–4.

[75] F. Pasic, D. Schutzenhofer, E. Jirousek, *et al.*, „Comparison of sub 6 GHz and mmWave wireless channel measurements at high speeds“, in *2022 16th European Conference on Antennas and Propagation (EuCAP)*, Mar. 2022, pp. 1–5. DOI: 10.23919/eucap53622.2022.9769375.

[76] A. Molisch, *Wireless communications*. Chichester, West Sussex, U.K: Wiley IEEE, 2011, ISBN: 9780470741870.

[77] F. T. Ulaby and D. G. Long, *Microwave radar and radiometric remote sensing*, eng. Ann Arbor, Mich: Univ. of Michigan Press, 2014, ISBN: 0472119354.

[78] G. Durgin, T. Rappaport, and D. de Wolf, „New analytical models and probability density functions for fading in wireless communications“, *IEEE Transactions on Communications*, vol. 50, no. 6, pp. 1005–1015, 2002. DOI: 10.1109/tcomm.2002.1010620.

[79] J. M. Romero-Jerez, F. J. Lopez-Martinez, J. P. Pena-Martin, and A. Abdi, „Stochastic fading channel models with multiple dominant specular components“, *IEEE Transactions on Vehicular Technology*, vol. 71, no. 3, pp. 2229–2239, 2022. DOI: 10.1109/tvt.2022.3141949.

[80] W. Schäfer, „A new deterministic/stochastic approach to model the intervehicle channel at 60 GHz“, in *IEEE 43rd Vehicular Technology Conference*, 1993, pp. 112–115. DOI: 10.1109/vetec.1993.507023.

[81] P. Bello, „Characterization of randomly time-variant linear channels“, *IEEE Transactions on Communications*, vol. 11, no. 4, pp. 360–393, 1963. DOI: 10.1109/tcom.1963.1088793.

[82] D. W. Matolak and Q. Wu, „Channel models for V2V communications: A comparison of different approaches“, in *Proceedings of the 5th European Conference on Antennas and Propagation (EUCAP)*, 2011, pp. 2891–2895.

[83] L. Bernado, T. Zemen, F. Tufvesson, A. F. Molisch, and C. F. Mecklenbrauker, „Time- and frequency-varying K-factor of non-stationary vehicular channels for safety-relevant scenarios“, *IEEE Transactions on Intelligent Transportation Systems*, vol. 16, no. 2, pp. 1007–1017, 2015. DOI: 10.1109/tits.2014.2349364.

[84] M. Yusuf, E. Tanghe, F. Challita, *et al.*, „Experimental characterization of V2I radio channel in a suburban environment“, in *2019 13th European Conference on Antennas and Propagation (EuCAP)*, 2019, pp. 1–5.

[85] D. B. Percival and A. T. Walden, *Spectral Analysis for Univariate Time Series* (Cambridge Series in Statistical and Probabilistic Mathematics). Cambridge University Press, 2020. DOI: 10.1017/9781139235723.

[86] G. Matz and F. Hlawatsch, „Time-frequency transfer function calculus (symbolic calculus) of linear time-varying systems (linear operators) based on a generalized underspread theory“, *Journal of Mathematical Physics*, vol. 39, no. 8, pp. 4041–4070, 1998. DOI: 10.1063/1.532495.

[87] G. Matz, H. Bolcskei, and F. Hlawatsch, „Time-frequency foundations of communications: Concepts and tools“, *IEEE Signal Processing Magazine*, vol. 30, no. 6, pp. 87–96, 2013. DOI: 10.1109/msp.2013.2269702.

[88] M. Niedźwiecki, *Identification of time-varying processes*. Wiley New York, 2000, ISBN: 0-471-98629-1.

[89] W. A. Gardner, A. Napolitano, and L. Paura, „Cyclostationarity: Half a century of research“, *Signal Processing*, vol. 86, no. 4, pp. 639–697, 2006. DOI: 10.1016/j.sigpro.2005.06.016.

[90] A. Maltsev, A. Pudeyev, A. Lomayev, and I. Bolotin, „Channel modeling in the next generation mmWave Wi-Fi: IEEE 802.11ay standard“, in *European Wireless 2016; 22th European Wireless Conference*, 2016, pp. 1–8.

[91] A. Paier, T. Zemen, L. Bernado, *et al.*, „Non-WSSUS vehicular channel characterization in highway and urban scenarios at 5.2 GHz using the local scattering function“, in *2008 International ITG Workshop on Smart Antennas*, Feb. 2008, pp. 9–15. DOI: 10.1109/wsa.2008.4475530.

[92] G. Ghiaasi, M. Ashury, D. Vlastaras, M. Hofer, Z. Xu, and T. Zemen, „Real-time vehicular channel emulator for future conformance tests of wireless its modems“, in *2016 10th European Conference on Antennas and Propagation (EuCAP)*, Apr. 2016. DOI: 10.1109/eucap.2016.7481226.

[93] M. Hofer, Z. Xu, D. Vlastaras, *et al.*, „Real-time geometry-based wireless channel emulation“, *IEEE Transactions on Vehicular Technology*, vol. 68, no. 2, pp. 1631–1645, 2019. DOI: 10.1109/tvt.2018.2888914.

[94] W. U. Bajwa, K. Gedalyahu, and Y. C. Eldar, „Identification of parametric underspread linear systems and super-resolution radar“, *IEEE Transactions on Signal Processing*, vol. 59, no. 6, pp. 2548–2561, 2011. DOI: 10.1109/tsp.2011.2114657.

[95] C. U. Bas, R. Wang, S. Sangodoyin, *et al.*, „Real-time millimeter-wave MIMO channel sounder for dynamic directional measurements“, *IEEE Transactions on Vehicular Technology*, vol. 68, no. 9, pp. 8775–8789, 2019. DOI: 10.1109/tvt.2019.2928341.

[96] M. Li, F. Zhang, Y. Ji, and W. Fan, „Virtual antenna array with directional antennas for millimeter-wave channel characterization“, *IEEE Transactions on Antennas and Propagation*, vol. 70, no. 8, pp. 6992–7003, 2022. DOI: 10.1109/tap.2022.3161334.

[97] A. Chopra, A. Thornburg, O. Kanhere, S. S. Ghassemzadeh, M. Majmundar, and T. S. Rappaport, „A real-time millimeter wave V2V channel sounder“, in *2022 IEEE Wireless Communications and Networking Conference (WCNC)*, Apr. 2022. DOI: 10.1109/wcnc51071.2022.9772001.

[98] *Radio Propagation Measurements and Channel Modeling: Best Practices for Millimeter-Wave and Sub-Terahertz Frequencies*. Cambridge University Press, 2022. DOI: 10.1017/9781009122740.

[99] R. Thomä, D. Hampicke, A. Richter, *et al.*, „Identification of time-variant directional mobile radio channels“, *IEEE Transactions on Instrumentation and Measurement*, vol. 49, no. 2, pp. 357–364, 2000. DOI: 10.1109/19.843078.

[100] S. Salous, S. M. Feeney, X. Raimundo, and A. A. Cheema, „Wideband MIMO channel sounder for radio measurements in the 60 GHz band“, *IEEE Transactions on Wireless Communications*, vol. 15, no. 4, pp. 2825–2832, 2016. DOI: 10.1109/twc.2015.2511006.

[101] Y. Konishi, M. Kim, M. Ghoraishi, J. Takada, S. Suyama, and H. Suzuki, „Channel sounding technique using MIMO software radio architecture“, in *Proceedings of the 5th European Conference on Antennas and Propagation (EUCAP)*, 2011, pp. 2546–2550.

[102] M. Kim, H. K. Pham, Y. Chang, and J.-i. Takada, „Development of low-cost 60-GHz millimeter-wave channel sounding system“, in *Proc. of Global Symposium on Millimeter Wave (GSMM)*, 2013.

[103] M. Lerch, E. Zöchmann, S. Caban, and M. Rupp, „Noise bounds in multicarrier mmWave Doppler measurements“, in *European Wireless 2017; 23th European Wireless Conference*, 2017, pp. 1–6.

[104] D. Chu, „Polyphase codes with good periodic correlation properties (corresp.)“, *IEEE Transactions on Information Theory*, vol. 18, no. 4, pp. 531–532, 1972. DOI: 10.1109/tit.1972.1054840.

[105] K. SAKAGUCHI, J.-i. TAKADA, and K. ARAKI, „A novel architecture for MIMO spatio-temporal channel sounder“, *IEICE Trans. Electron.*, vol. 85, no. 3, pp. 436–441, Mar. 2002, ISSN: 09168524.

[106] G. Matz, A. Molisch, F. Hlawatsch, M. Steinbauer, and I. Gaspard, „On the systematic measurement errors of correlative mobile radio channel sounders“, *IEEE Transactions on Communications*, vol. 50, no. 5, pp. 808–821, 2002. DOI: 10.1109/tcomm.2002.1006562.

[107] A. Freedman and N. Levanon, „Properties of the periodic ambiguity function“, *IEEE Transactions on Aerospace and Electronic Systems*, vol. 30, no. 3, pp. 938–941, 1994. DOI: 10.1109/7.303781.

[108] S. Salous, „Measurement of multipath delay statistics over a 72-to 90-mhz bandwidth at 1.8 GHz in two european cities using a chirp sounder“, *Radio Science*, vol. 34, no. 4, pp. 797–816, 1999. DOI: 10.1029/1999rs900014.

[109] H. L. Van Trees, *Detection, Estimation, and Modulation Theory: Part III. Radar-sonar Signal Processing and Gaussian Signal in Noise*. John Wiley & Sons, Inc., 2001.

[110] R. Bultitude, „Propagation measurement-based wireless channel characterization and modeling“, in *New Directions in Wireless Communications Systems*, CRC Press, 2017, pp. 1–46.

[111] Z. Wang, F. Tigrek, O. Krasnov, F. V. D. Zwan, P. V. Genderen, and A. Yarovoy, „Interleaved OFDM radar signals for simultaneous polarimetric measurements“, *IEEE Transactions on Aerospace and Electronic Systems*, vol. 48, no. 3, pp. 2085–2099, 2012. DOI: 10.1109/taes.2012.6237580.

[112] M. A. Richards, *Fundamentals of radar signal processing*, 2. ed. New York: McGraw-Hill, 2014, ISBN: 0071798323.

[113] S. Schwarz, E. Zöchmann, M. Muller, and K. Guan, „Dependability of directional millimeter wave vehicle-to-infrastructure communications“, *IEEE Access*, vol. 8, pp. 53 162–53 171, 2020. DOI: 10.1109/access.2020.2981166.

[114] M. Rao, F. J. Lopez-Martinez, M.-S. Alouini, and A. Goldsmith, „MGF approach to the analysis of generalized two-ray fading models“, *IEEE Transactions on Wireless Communications*, vol. 14, no. 5, pp. 2548–2561, 2015. DOI: 10.1109/twc.2014.2388213.

[115] S. H. Choi, P. Smith, B. Allen, W. Q. Malik, and M. Shafi, „Severely fading MIMO channels: Models and mutual information“, in *2007 IEEE International Conference on Communications*, Jun. 2007, pp. 4628–4633. DOI: 10.1109/icc.2007.764.

[116] J. Kunisch and J. Pamp, „Wideband car-to-car radio channel measurements and model at 5.9 GHz“, in *2008 IEEE 68th Vehicular Technology Conference*, Sep. 2008, pp. 1–5. DOI: 10.1109/vetecf.2008.64.

[117] M. Peter, W. Keusgen, and R. J. Weiler, „On path loss measurement and modeling for millimeter-wave 5G“, in *Proceedings of the 9th European Conference on Antennas and Propagation (EUCAP)*, 2015, pp. 1–5.

[118] D. W. Matolak, H. Jamal, and R. Sun, „Spatial and frequency correlations in two-ray air-ground simo channels“, in *2017 IEEE International Conference on Communications (ICC)*, May 2017, pp. 1–6. DOI: 10.1109/icc.2017.7996954.

[119] E. Zöchmann, J. Blumenstein, R. Marsalek, M. Rupp, and K. Guan, „Parsimonious channel models for millimeter wave railway communications“, in *2019 IEEE Wireless Communications and Networking Conference (WCNC)*, Apr. 2019, pp. 1–6. DOI: 10.1109/wcnc.2019.8885923.

[120] S. Schwarz and E. Zöchmann, „Robust beam-alignment for TWDP fading millimeter wave channels“, in *2019 IEEE 20th International Workshop on Signal Processing Advances in Wireless Communications (SPAWC)*, Jul. 2019, pp. 1–5. DOI: 10.1109/spawc.2019.8815503.

[121] Y. Chen and N. Beaulieu, „Estimation of Ricean and Nakagami distribution parameters using noisy samples“, in *2004 IEEE International Conference on Communications (ICC)*, 2004, pp. 562–566. DOI: 10.1109/icc.2004.1312552.

[122] A. Papoulis and S. Pillai, *Probability, Random Variables and Stochastic Processes*. McGraw-Hill, 2002, ISBN: 0073660116.

[123] N. Heckert and J. Filliben, „NIST/SEMATECH e-handbook of statistical methods (NIST handbook 151)“, in National Institute of Standards and Technology, 2012, ch. Exploratory Data Analysis. DOI: 10.18434/m32189.

[124] F. J. Massey, „The Kolmogorov-Smirnov test for goodness of fit“, *Journal of the American Statistical Association*, vol. 46, no. 253, pp. 68–78, 1951. DOI: 10.1080/01621459.1951.10500769.

[125] M. T. Ortiz, H. Groll, E. Zöchmann, and C. F. Mecklenbräucker, „Vehicle tracking through vision-millimeter wave Doppler shift fusion“, in *2019 IEEE-APS Topical Conference on Antennas and Propagation in Wireless Communications (APWC)*, Sep. 2019. DOI: 10.1109/apwc.2019.8870369.

[126] R. Bultitude, „Estimating frequency correlation functions from propagation measurements on fading radio channels: A critical review“, *IEEE Journal on Selected Areas in Communications*, vol. 20, no. 6, pp. 1133–1143, 2002. DOI: 10.1109/jsac.2002.801212.

[127] D. W. Matolak and J. Frolik, „Worse-than-Rayleigh fading: Experimental results and theoretical models“, *IEEE Communications Magazine*, vol. 49, no. 4, pp. 140–146, 2011. DOI: 10.1109/mcom.2011.5741158.

[128] D. W. Matolak and R. Sun, „Air-ground channel characterization for unmanned aircraft systems-Part I: Methods, measurements, and models for over-water settings“, *IEEE Transactions on Vehicular Technology*, vol. 66, no. 1, pp. 26–44, 2017. DOI: 10.1109/tvt.2016.2530306.

[129] G. Matz, „On non-WSSUS wireless fading channels“, *IEEE Transactions on Wireless Communications*, vol. 4, no. 5, pp. 2465–2478, 2005. DOI: 10.1109/twc.2005.853905.

[130] G. Matz, „Doubly underspread non-WSSUS channels: Analysis and estimation of channel statistics“, in *Proceedings of the International Workshop on Signal Processing Advances in Wireless Communications (SPAWC)*, Jun. 2003, pp. 190–194. DOI: 10.1109/spawc.2003.1318948.

[131] D. Thomson, „Spectrum estimation and harmonic analysis“, *Proceedings of the IEEE*, vol. 70, no. 9, pp. 1055–1096, 1982. DOI: 10.1109/proc.1982.12433.

[132] M. Pätzold and C. A. Gutierrez, „Modelling of non-WSSUS channels with time-variant Doppler and delay characteristics“, in *2018 IEEE Seventh International Conference on Communications and Electronics (ICCE)*, Jul. 2018, pp. 1–6. DOI: 10.1109/cce.2018.8465761.

[133] H. Krim and M. Viberg, „Two decades of array signal processing research: The parametric approach“, *IEEE Signal Processing Magazine*, vol. 13, no. 4, pp. 67–94, 1996. DOI: 10.1109/79.526899.

[134] R. Schmidt, „Multiple emitter location and signal parameter estimation“, *IEEE Transactions on Antennas and Propagation*, vol. 34, no. 3, pp. 276–280, 1986. DOI: 10.1109/tap.1986.1143830.

[135] M. Amin, A. Belouchrani, and Y. Zhang, „The spatial ambiguity function and its applications“, *IEEE Signal Processing Letters*, vol. 7, no. 6, pp. 138–140, 2000. DOI: 10.1109/97.844632.

[136] A. Barabell, „Improving the resolution performance of eigenstructure-based direction-finding algorithms“, in *ICASSP '83. IEEE International Conference on Acoustics, Speech, and Signal Processing*, vol. 8, 1983, pp. 336–339. DOI: 10.1109/ICASSP.1983.1172124.

[137] A. Paulraj, R. Roy, and T. Kailath, „Estimation of signal parameters via rotational invariance techniques - ESPRIT“, in *Nineteeth Asilomar Conference on Circuits, Systems and Computers, 1985*, Nov. 1985, pp. 83–89. DOI: 10.1109/acssc.1985.671426.

[138] M. Haardt, M. Zoltowski, C. Mathews, and J. Nossek, „2d unitary esprit for efficient 2d parameter estimation“, in *1995 International Conference on Acoustics, Speech, and Signal Processing*, May 1995, pp. 2096–2099. DOI: 10.1109/icassp.1995.478488.

[139] P. Stoica, P. Babu, and J. Li, „New method of sparse parameter estimation in separable models and its use for spectral analysis of irregularly sampled data“, *IEEE Transactions on Signal Processing*, vol. 59, no. 1, pp. 35–47, 2011. DOI: 10.1109/tsp.2010.2086452.

[140] R. Tibshirani, „Regression shrinkage and selection via the lasso“, *Journal of the Royal Statistical Society: Series B (Methodological)*, vol. 58, no. 1, pp. 267–288, 1996. DOI: 10.1111/j.2517-6161.1996.tb02080.x.

[141] E. J. Candès, J. K. Romberg, and T. Tao, „Stable signal recovery from incomplete and inaccurate measurements“, *Communications on Pure and Applied Mathematics*, vol. 59, no. 8, pp. 1207–1223, 2006. DOI: 10.1002/cpa.20124.

[142] E. Candes, J. Romberg, and T. Tao, „Robust uncertainty principles: Exact signal reconstruction from highly incomplete frequency information“, *IEEE Transactions on Information Theory*, vol. 52, no. 2, pp. 489–509, 2006. DOI: 10.1109/tit.2005.862083.

[143] T. Zemen and C. Mecklenbräuker, „Time-variant channel estimation using discrete prolate spheroidal sequences“, *IEEE Transactions on Signal Processing*, vol. 53, no. 9, pp. 3597–3607, 2005. DOI: 10.1109/tsp.2005.853104.

[144] G. Leus, „On the estimation of rapidly time-varying channels“, in *2004 12th European Signal Processing Conference*, IEEE, 2004, pp. 2227–2230.

[145] T. Blazek, H. Groll, S. Pratschner, and E. Zöchmann, „Vehicular channel characterization in orthogonal time-frequency space“, in *2019 IEEE International Conference on Communications Workshops (ICC Workshops)*, May 2019. DOI: 10.1109/iccw.2019.8756717.

[146] V. Chandrasekaran, B. Recht, P. A. Parrilo, and A. S. Willsky, „The convex geometry of linear inverse problems“, *Foundations of Computational Mathematics*, vol. 12, no. 6, pp. 805–849, 2012. DOI: 10.1007/s10208-012-9135-7.

[147] Y. Chi and Y. Chen, „Compressive two-dimensional harmonic retrieval via atomic norm minimization“, *IEEE Transactions on Signal Processing*, vol. 63, no. 4, pp. 1030–1042, 2015. DOI: 10.1109/tsp.2014.2386283.

[148] G. Tang, B. N. Bhaskar, P. Shah, and B. Recht, „Compressed sensing off the grid“, *IEEE Transactions on Information Theory*, vol. 59, no. 11, pp. 7465–7490, 2013. DOI: 10.1109/tit.2013.2277451.

[149] Z. Yang, L. Xie, and P. Stoica, „Vandermonde decomposition of multilevel toeplitz matrices with application to multidimensional super-resolution“, *IEEE Transactions on Information Theory*, vol. 62, no. 6, pp. 3685–3701, 2016. DOI: 10.1109/tit.2016.2553041.

[150] Z. Yang and L. Xie, „Enhancing sparsity and resolution via reweighted atomic norm minimization“, *IEEE Transactions on Signal Processing*, vol. 64, no. 4, pp. 995–1006, 2016. DOI: 10.1109/tsp.2015.2493987.

[151] Y. Wang and Z. Tian, „IVDST: A fast algorithm for atomic norm minimization in line spectral estimation“, *IEEE Signal Processing Letters*, vol. 25, no. 11, pp. 1715–1719, 2018. DOI: 10.1109/lsp.2018.2870539.

[152] Z. Tian, Z. Zhang, and Y. Wang, „Low-complexity optimization for two-dimensional direction-of-arrival estimation via decoupled atomic norm minimization“, in *Proc. 2017 IEEE Int. Conf. on Acoustics, Speech and Signal Processing (ICASSP)*, Mar. 2017, pp. 3071–3075. DOI: 10.1109/icassp.2017.7952721.

[153] M.-M. Liu, C.-X. Dong, Y.-Y. Dong, and G.-Q. Zhao, „Superresolution 2D DOA estimation for a rectangular array via reweighted decoupled atomic norm minimization“, *Mathematical Problems in Engineering*, vol. 2019, pp. 1–13, 2019. DOI: 10.1155/2019/6797168.

[154] Z. Zhang, Y. Wang, and Z. Tian, „Efficient two-dimensional line spectrum estimation based on decoupled atomic norm minimization“, *Signal Processing*, vol. 163, pp. 95–106, 2019. DOI: 10.1016/j.sigpro.2019.04.024.

[155] T. Sarkar and O. Pereira, „Using the matrix pencil method to estimate the parameters of a sum of complex exponentials“, *IEEE Antennas and Propagation Magazine*, vol. 37, no. 1, pp. 48–55, 1995. DOI: 10.1109/74.370583.

[156] F. Ulaby, T. Haddock, and R. Austin, „Fluctuation statistics of millimeter-wave scattering from distributed targets“, *IEEE Transactions on Geoscience and Remote Sensing*, vol. 26, no. 3, pp. 268–281, 1988. DOI: 10.1109/36.3030.

[157] N. Czink, F. Kaltenberger, Y. Zhou, L. Bernado, T. Zemen, and X. Yin, „Low-complexity geometry-based modeling of diffuse scattering“, in *Proceedings of the Fourth European Conference on Antennas and Propagation*, Apr. 2010.

[158] B. O'Donoghue, E. Chu, N. Parikh, and S. Boyd, „Conic optimization via operator splitting and homogeneous self-dual embedding“, *Journal of Optimization Theory and Applications*, vol. 169, no. 3, pp. 1042–1068, 2016. DOI: 10.1007/s10957-016-0892-3.

[159] D. Slepian, „Prolate spheroidal wave functions, fourier analysis, and uncertainty-V: The discrete case“, *Bell System Technical Journal*, vol. 57, no. 5, pp. 1371–1430, 1978. DOI: 10.1002/j.1538-7305.1978.tb02104.x.